Characterisation of the self-assembly and particle formation of major core protein VP7 of AHSV

by

Gayle Victoria Wall

Submitted in partial fulfilment of the requirements for the degree

Magister Scientiae

In the Faculty of Natural & Agricultural Sciences

University of Pretoria

Pretoria

July 2014

i

DECLARATION

I, Gayle Victoria Wall, declare that the dissertation, which I hereby submit for the degree *Magister Scientiae* at the University of Pretoria, is my own work and has not previously been submitted by me for a degree at this or any other tertiary institution.

SIGNATURE:

DATE:

ACKNOWLEDGEMENTS

RESEARCH OUTPUTS

The results of this study have contributed to the following presentations at various national and international scientific meetings:

Poster presentations:

- Wall, G.V., Van Staden, V. and Huismans, H. (2011) Intracellular trafficking and localisation of correctly folded and misfolded AHSV VP7-eGFP fusion proteins. Proceedings of the Microscopy Society of Southern Africa, Volume 41, pg 16.

- Gayle V. Wall, Vida van Staden and Henk Huismans (2012) Investigating the solubility and localisation of African horse sickness virus VP7-eGFP fusion proteins. SAGS 2012, Stellenbosch, South Africa, 10 – 12 September 2012.

- Shani M. Bekker, Gayle V. Wall, Henk Huismans, Vida van Staden and Jacques Theron (2012) Factors that determine AHSV protein VP7 localisation and core assembly. Eleventh International Symposium on Double Stranded RNA viruses, Puerto Rico, 27 November – 1 December 2012.

- Wall G. V., van der Merwe C. F., Hall A. N., Huismans H., van Staden V (2014) Characterising the effect of top domain modifications on the self-assembly and particle formation of major core protein VP7 of African horse sickness virus. 18th International Microscopy Congress, Prague, Czech Republic, 7 – 12 September 2014.

- Gayle V. Wall, Christiaan F. van der Merwe, Alan N. Hall, Henk Huismans, Vida van Staden (2014) An investigation into the effect of various top domain modifications on the self-assembly and particle formation of African horse sickness virus protein VP7. SAGS 2014, Tshwane, South Africa, 23 – 26 September 2014.

Oral presentations:

- Bekker, S.M., Wall, G.V., Van Staden, V. and Huismans, H. (2011) Investigating the factors that affect the transport and intracellular localisation of AHSV structural protein VP7. Virology Africa 2011, Cape Town, South Africa, 29 November - 02 December 2011.

- G.V. Wall, C.F. van der Merwe, A.N. Hall, H. Huismans and V. van Staden (2012) Comparing the ultrastructure of wild-type and mutant AHSV VP7 and VP7-eGFP protein aggregates. Proceedings of the Microscopy Society of Southern Africa, Volume 42, pg 25. (Fiona Graham prize for "First-time-accepted-no-changes" abstract).

- G.V. Wall, C.F. van der Merwe, A.N. Hall, H. Huismans and V. van Staden (2013) Characterisation of the self-assembly and particle formation of major core protein VP7 of AHSV. Proceedings of the Microscopy Society of Southern Africa, Volume 43, pg 14.

SUMMARY

CHARACTERISATION OF THE SELF-ASSEMBLY AND PARTICLE FORMATION OF MAJOR CORE PROTEIN VP7 OF AHSV

by

GAYLE VICTORIA WALL

Supervisor: Dr V. van Staden

Department of Genetics

University of Pretoria

Co-supervisor: Prof H. Huismans

Department of Genetics

University of Pretoria

For the degree *Magister Scientiae*

The highly infectious vector-borne disease African horse sickness (AHS) is caused by African horse sickness virus (AHSV), a non-enveloped dsRNA virus of major economic importance in South Africa. The AHSV virion has a double-layered protein capsid comprised of a diffuse outer layer housing an inner icosahedral core. Viral protein (VP) 7 is the major core particle surface protein and forms trimers that can either be incorporated into the core or can self-assemble into flat hexagonal crystalline-like particles, a characteristic unique to AHSV VP7. Little is known about the self-assembly and particle formation of this highly hydrophobic and insoluble protein, and in particular what drives the stable layering of VP7 into these particles.

In this study, the effect of various minor and major top domain modifications on the self-assembly and particle formation was investigated by comparing the previously constructed AHSV VP7 vector (VP7-144, VP7-177 and VP7-200) and VP7-eGFP fusion proteins (VP7-144-eGFP, VP7-177-eGFP and VP7-200-eGFP), known to differ with regard to solubility and trimerisation, to wild type (WT) AHSV VP7. The dual confocal and transmission electron microscopy approach showed that self-assembly was unaffected by all of the modifications. Particle formation was however affected, as the morphology of the protein structures formed by all six proteins differed from the hexagonal particles formed by WT VP7.

Sucrose gradient sedimentation analysis was used to investigate the kinetics of the VP7-eGFP aggregation observed in previous studies. These results showed that VP7-144-eGFP is an inherently soluble and fluorescing protein, the spontaneous aggregation of which is L-arginine reversible. VP7-200-eGFP, however, is a largely misfolded protein with no evidence of protein aggregation. Immunofluorescence and confocal microscopy was used to investigate the localisation of misfolded, non-fluorescing VP7-eGFP fusion proteins in relation to their correctly folded, fluorescing versions. No such proteins were differentially detected using this approach thereby suggesting that both versions are located in the same area, either due to both versions being transported in a similar manner or due to correctly folded proteins becoming trapped in misfolded protein. Alternatively, the approach itself may be unsuccessful in detecting misfolded VP7-eGFP fusion proteins.

Although the role of AHSV VP7 particles in the replication cycle and disease pathogenesis remains to be investigated, this study provides insights into the self-assembly and particle formation thereof. In particular, it is the top domain in combination with a group of associated factors that strongly influences the stable layering of VP7 to form the characteristic particles.

ABBREVIATIONS

3D	Three dimensional
°C	Degrees Celsius
µl	microliter
µm	micrometer
A/Ala	Alanine
Å	Angstrom
aa	amino acid
AGQ	AHSV Ala-167-Gly-168-Gln-169
AHS	African horse sickness
AHSV	African horse sickness virus
Asp/D	Aspartic acid
ATP	Adenosine triphosphate
Bac	Baculovirus
BHK	Baby hamster kidney
bp	base pair
BTV	Bluetongue virus
Ca^{2+}	Calcium ion
CFP	Cyan fluorescent protein
CFTR	Cystic Fibrosis Transmembrane Conductance Regulator
CLPs	Core-like particles
CPE	Cytopathic effect
Cr	Crystalline-like particle
C. imicola	*Culicoides imicola*
D	Disc-shaped crystal
Da	Dalton
DAPI	4',6-diamidino-2-phenylindole
dH_2O	distilled water
dsRNA	double stranded ribonucleic acid
E	Glutamic acid
E. coli	*Escherichia coli*
EHDV	Epizootic hemorrhagic disease virus
eGFP	enhanced green fluorescent protein
ENSO	El Niňo/Southern Oscillation
ER	Endoplasmic reticulum
ESCRT	Endosomal sorting complex required for trafficking
et al.	*et alia* (and others)

F	Phenylalanine
f	fibrillar structure
FCS	Fluorescence correlation microscopy
FCS	Foetal calf serum
FRET	Fluorescence resonance energy transfer
FS	Freeze substitution
G	Gauge
G/Gly	Glycine
GFPs	Green fluorescent proteins
Gln/Q	Glutamine
HIV	Human immunodeficiency virus
HPF	High pressure freezing
hpi	hours post infection
I	Isoleucine
K	Lysine
kDa	kiloDalton
L	Leucine
M	Marker
M	Molar
ml	millilitre
MOI	Multiplicity of infection
mRNA	messenger RNA
ms	millisecond
MS	Monkey kidney cells
MTOC	Microtubule organising center
MTT	Thiazolyl Blue Tetrazolium Blue
MVBs	Multivesicular bodies
N	Nucleus
nm	nanometer
n.m.	nuclear membrane
NP-40	Nonidet®-P-40
NS	Non-structural
NSP	Non-structural protein
P	Pellet
P	Proline
PBS	Phosphate buffered saline
pfu	plaque forming units
p.m.	plasma membrane

viii

PS1	Presenilin-1
PSB	Protein solvent buffer
R	Arginine
RGD	BTV Arg-168-Gly-169-Asp-170
RNA	Ribonucleic acid
rpm	revolutions per minute
S	Soluble region
S/Ser	Serine
SDS	Sodium dodecyl sulphate
SDS-PAGE	Sodium dodecyl sulphate-polyacrylamide gel electrophoresis
SEM	Scanning electron microscopy
Sf9	*Spodoptera frugiperda* insect cells
SNARE	soluble *N*-ethylmaleimide-sensitive fusion attachment protein receptor
ssRNA	single stranded ribonucleic acid
T/Thr	Threonine
TEM	Transmission electron microscopy
TEMED	N,N,N',N' tetramethylethylene diamine
TGN	*trans*-Golgi network
TGS buffer	Tris-Glycine-SDS buffer
Tsg101	Tumour-susceptibility gene 101 protein
Tub	NS1 tubules
Tyr	Tyrosine
V	Valine
V	AHSV virions
V	Voltage
VIBs	Viral inclusion bodies
VLPs	Virus-like particles
VP	Viral protein
WT	Wild type
w/v	weight per volume
YFP	Yellow fluorescent protein

LIST OF BUFFERS

Blocking buffer	0.1 M Potassium Phosphate buffer
	5% FCS
	0.05% Tween-20
Lysis buffer	0.01 M STE (Tris, EDTA, NaCl)
	0.5% Nonidet®-P-40 (NP-40)
PBS	137 mM NaCl
	2.7 mM KCl
	4.3 mM Na2HPO4.2H2O
	1.4 mM KH_2PO4
	[pH 7.3]
Potassium phosphate buffer (0.1M)	1 M K_2HPo_4
	1 M KH_2PO_4
	[pH 7.2]
PSB (3x)	0.188 mM Tris-HCl
	6% SDS
	30% glycerol
	15% 2-mercaptoethanol
	0.005% bromophenol blue
	[pH 6.8]
TGS	25 mM Tris-HCl
	192 mM glycine
	0.1% SDS
	[pH 8.3]
Towbin's transfer buffer	25 mM Tris
	192 mM Glycine
	20% Methanol
	[pH 8.3]
Wash buffer	0.05% Tween-20 in 1 x PBS

TABLE OF CONTENTS

Chapter 1
Literature Review

1.1 Introduction

African horse sickness virus (AHSV) is the causative agent of African horse sickness (AHS), an economically important viral disease of *Equidae* endemic to many areas of sub-Saharan Africa and possibly even Yemen in the Arabian Peninsula (Mellor and Hamblin 2004). The virus has however extended as far as India, Pakistan, and in recent years, certain parts of Europe. The focus of this study is on AHSV viral protein (VP) 7, the major structural protein of the AHSV core particle. This protein forms trimers that can either be incorporated into the core, or alternatively, can self-assemble into flat, hexagonal crystalline-like particles in the cell, a characteristic unique to AHSV VP7. To date little is known about the self-assembly and particle formation of AHSV VP7. This literature review will give an overview of orbivirus disease and epidemiology followed by a discussion of orbivirus molecular biology and the role of each protein in the replication cycle. The main focus of the review will then be on both AHSV and bluetongue virus (BTV) VP7, and will end with a discussion of protein folding and misfolding and the host cell mechanisms used to deal with such proteins.

1.2 Orbivirus disease and epidemiology

The arbovirus AHSV is a member of the *Orbivirus* genus (family *Reoviridae*) of which the closely related BTV is the prototype species. To date, 9 serotypes of AHSV (Howell 1962) and 24 serotypes of BTV have been identified. Both AHSV and BTV are transmitted by certain species of the *Culicoides* biting midge. The most important species is *C. imicola,* an Afro-Asiatic midge that is the most widespread of the *Culicoides* species, stretching throughout Africa, south-east Asia and certain parts of Europe, including Spain and Portugal (Mellor and Hamblin 2004).

AHSV has a dual life-cycle, infecting and replicating in both insect and mammalian cells. Zebras are considered to be the natural reservoir of the virus, whereas horses are the most susceptible to this virus, exhibiting a mortality rate of as high as 90% (Mellor and Hamblin 2004). Upon infection of the mammalian host, AHSV multiplies in the lymph nodes prior to the dissemination of the virus throughout the body via the circulatory system. This is followed by infection of the target organs and cells (heart, lungs, spleen, lymphoid tissues and certain endothelial cells), in which secondary viraemia occurs (Mellor and Hamblin 2004; Clift and Penrith 2010). There are four forms of the disease AHS, namely horse sickness fever (the mildest form), the mixed form, the cardiac/subacute form and the pulmonary form, each differing in severity with the latter causing the most deaths of infected animals with a mortality rate commonly exceeding 95% (Mellor and Hamblin 2004). As a result of its severity, AHS has joined BTV as an OIE-listed disease (OIE 2011).

The first reference to AHS concerned an epidemic in Yemen in 1327, the virus is however believed to have originated in Africa (Mellor and Hamblin 2004). The first major outbreak of AHS in southern Africa occurred in 1719, killing over 1 700 animals. Since then, there have been a number of outbreaks of the disease, of which the outbreak of 1854-1855 was the most severe, killing some 70 000 horses, which at the time made up about 40% of the entre horse population of the Cape of Good Hope (Coetzer and Guthrie 2004; Mellor and Hamblin 2004). Traditionally AHS was most prevalent in the northern parts of South Africa, with outbreaks between 1955 and 1995 occurring every summer in these areas, but only once every 5 to 10 years in the centre of the country. AHS was rarely found in the Western Cape with only four confirmed outbreaks of AHS occurring between 1950 and 2006 (in 1967, 1990, 1998 and 2004) the latter two of which led to a two-year suspension on the export of horses costing the industry about R50 million (US$ 8.2 million) per annum (Venter *et al.* 2006).

Of the 9 serotypes of AHSV, serotypes 1 through 8 are usually only found within regions of sub-Saharan Africa, whereas type 9 has been responsible for many of the outbreaks outside of the African continent, the exceptions being the Spanish-Portuguese outbreaks of 1987-1990 which were due to AHSV-4, as well as the occurrence of serotype 2 in Ethiopia (2006), Senegal (2007) and Nigeria (2007), serotype 6 in Ethiopia (2003) and serotype 7 in Senegal (2007) (Maclachlan and Guthrie 2010).

The current northward expansion of *C. imicola*, as well as the ability of AHSV to overwinter in southern Spain, Portugal and Morocco, highlights the possibility of outbreaks of AHSV similar to those of BTV in recent years whereby at least eight serotypes of BTV have spread across Europe (Mellor and Hamblin 2004; Gould and Higgs 2009; Maclachlan and Guthrie 2010). Furthermore, the emergence of several new BTV serotypes, as well as a serotype of the related epizootic hemorrhagic disease virus (EHDV) in certain parts of North and South America has led to concerns over future and more extensive outbreaks of BTV in those areas (Gibbs *et al.* 2008; Maclachlan and Guthrie 2010). Novel BTV serotypes have also been found in Israel and Australia, and BTV-8 emerged in Belgium, France, Luxembourg, Germany and the Netherlands (August 2006), and the United Kingdom (September 2007) and could be indicative of a changing epidemiology of the virus (Gibbs *et al.* 2008; Gould and Higgs 2009; Maclachlan and Guthrie 2010). The increased incidence of both BTV and AHSV in recent years may be due, in part, to climate change, and indeed global warming, which is causing ever increasing temperatures that lead to more favourable breeding grounds for arthropods such as the *Culicoides* species which is known to thrive in warmer, wet environments.

Major outbreaks of AHS in South Africa tend to occur every 10-15 years, and may coincide with the warm (El Niňo) phase of the El Niňo/Southern Oscillation (ENSO). The effect of climate change is

2

however, a complicated one, as it will almost certainly continue to cause social and economic changes throughout the world which may in turn affect the transmission of insect-transmitted diseases (Maclachlan 2010).

The control measures targeted at the vector are not sufficient to prevent the disease, and the only vaccines commercially available are live-attenuated vaccines that are not registered in Europe (Mellor and Hamblin 2004). Thus, there is a need for an improved vector control measures, surveillance systems and efficacious, inactivated vaccines, a goal of much research over the past few decades. Recent outbreaks of BTV have indicated that once these viruses reach North Africa they spread readily throughout the Mediterranean basin (Maclachlan and Guthrie 2010).

In order to better understand viral disease, it is important to have some insight into the genome and virion structural organisation.

1.3 Orbivirus genome and virion structural organisation

AHSV and BTV are non-enveloped viruses that have a dsRNA genome composed of 10 segments, housed in a double-layered protein capsid (Els and Verwoerd 1969; Verwoerd 1969; Oellermann 1970; Oellermann *et al.* 1970; Verwoerd *et al.* 1970; Verwoerd *et al.* 1972; Bremer 1976). As listed in Table 1, the 10 segments of the dsRNA genome range from 17 to 150 kDa in size and encode seven structural proteins (VP1-VP7) as well as five non-structural proteins NS1, NS2, NS3, NS3A and the newly discovered NS4 (Belhouchet *et al.* 2011; Ratinier *et al.* 2011). All segments encode one protein, except for segment 9 which encodes both VP6 and NS4 from two out-of-phase overlapping reading frames (Firth 2008; Belhouchet *et al.* 2011), and segment 10 which encodes both NS3 and NS3A from two in-phase overlapping open reading frames (van Staden *et al.* 1991).

In orbiviruses, the dsRNA genome is enclosed in an icosahedral core surrounded by a diffuse outer capsid layer. At the time, the BTV core was the largest molecular structure to be solved at such a high resolution, and revealed the organisation of the VP3 and VP7 layers (Grimes *et al.* 1998). Minor structural proteins VP1, VP4 and VP6 form the enzymatic machinery of the orbivirus core (Fig. 1A) and together with the dsRNA genome are encapsidated by two concentric layers of the major structural proteins VP3 (Fig. 1B) and VP7 (Fig. 1C) to form a viral transcription machine.

In an architecture that seems to be conserved among dsRNA viruses, the VP3 scaffold is composed of a total of 120 VP3 subunits (monomers) arranged in a T=2 icosahedral symmetry (Prasad *et al.* 1992), and can be grouped into two sets of 60 subunits (Grimes *et al.* 1998), namely, sets A (Fig. 1B, red) and B (Fig. 1B, cyan). Pairs of A subunits span the icosahedral two-fold axes, where they are almost in contact with one another. These subunits link adjacent five-fold axes and

3

Table 1 The 10 BTV dsRNA segments, the proteins they encode and their functions.

Segment (size in bp)	Protein(s) encoded (size in kilo Daltons)	Protein function
S1 (3944)	VP1 (150)	RNA dependent RNA polymerase
S2 (2926)	VP2 (111)	Receptor binding and cell entry
S3 (2772)	VP3 (103)	Core structural protein, encloses the viral polymerase complex
S4 (2011)	VP4 (76)	Viral capping enzyme
S5 (1769)	NS1 (64)	Viral protein translation enhancer, forms tubules
S6 (1637)	VP5 (59)	Outer capsid structural protein, membrane permeabilisation protein
S7 (1156)	VP7 (38)	Major core structural protein, receptor binding protein for *Culicoides* cells
S8 (1124)	NS2 (42)	Concentrator of core components, viral inclusion body formation
S9 (1046)	VP6 (36) NS4 (17)	Viral helicase Viral fitness to interferon response
S10 (822)	NS3 (26) NS3A (25)	Adaptor protein facilitating viral egress

Adapted from Patel and Roy (2014).

form a continuous scaffold that determines the eventual size of the subcore. By forming triangular plugs at the icosahedral three-fold axes, the B subunits seal the subcore (cyan, Fig. 1B), resulting in a somewhat fragile VP3 scaffold stabilised by the addition of an adherent lattice of 260 almost identical trimers of VP7 (Grimes *et al.* 1998) arranged on a T=13 icosahedral lattice (Prasad *et al.* 1992) (Fig. 1C). The VP7 outer layer of the core will be discussed in more detail in Section 1.5. The core particle has a diameter of between 690-700 Å (Prasad *et al.* 1992; Grimes *et al.* 1998).
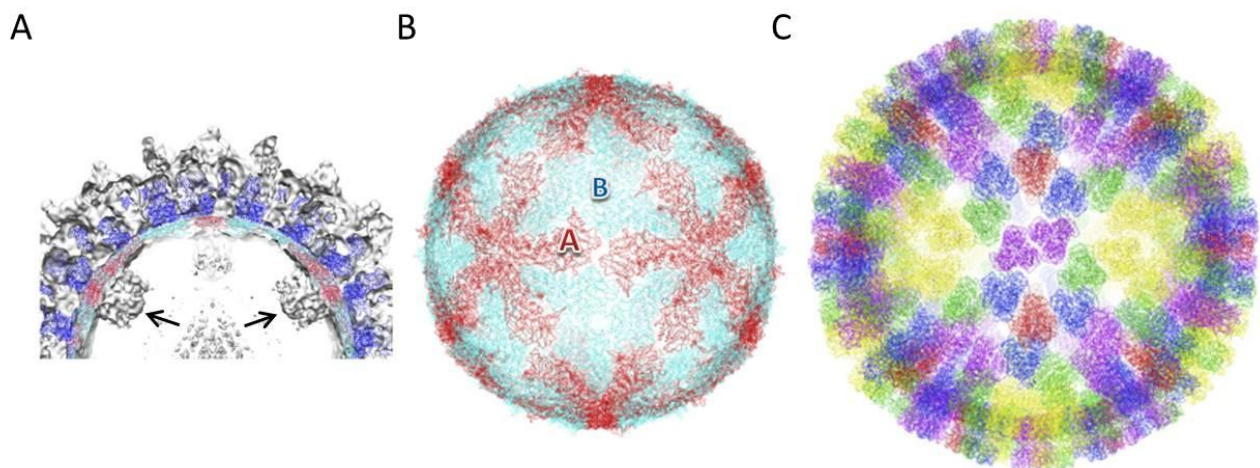
Fig. 1 Homology modelling of AHSV core particle. (A) Slabbed isosurface representation of AHSV-7 tVP2 empty-particle reconstruction. The VP3 scaffold is shown in cyan and red, with VP7 shown in blue. The transcription complex can be seen as protruding lumps of density (arrows in A) protruding inward from the VP3 scaffold. (B) Model of the VP3 subcore composed of 120 molecules of VP3 in a T=2 arrangement. The A subunits (red) span the icosahedral two-fold axis, while the B subunits (cyan) form triangular plugs at the icosahedral five-fold axes. (C) Model of the VP7 outer layer composed of 780 VP7 molecules arranged in a T=13 arrangement. Adapted from (Manole *et al.* 2012).

4

The major structural proteins VP2 and VP5 form the outer capsid which has two distinct motifs present in its organisation, namely globular motifs, representing VP5, interspersed between propeller-shaped triskelion motifs, representing VP2, the outer most viral protein (Hewat *et al.* 1992; Hewat *et al.* 1994; Hassan *et al.* 2001; Nason *et al.* 2004). The BTV VP2 triskelion has a central hub domain from which three tip domains branch, creating three gaps that are filled by the VP5 trimers (Figs. 2B and 2C (Zhang *et al.* 2010)). The hub domain associates with the upper surface of the VP7 trimer, whereas VP5 interacts with the sides of the VP7 trimer (Nason *et al.* 2004). Similar to the fusion proteins of many enveloped viruses the VP5 trimer has a central coiled-coil α-helical bundle (Zhang *et al.* 2010). Furthermore, cryoEM studies have shown that there are 15 amphipathic α-helical regions on the surface of each trimer that may be involved in the penetration of the endosomal membrane and the subsequent release of the core into the cytoplasm. As shown in Figure 2A, the tips of each VP2 propeller bend at a 90˚ angle to the rest of the virus and give the virion its final diameter, with each tip extending outwards from the rest of the particle by approximately 30Å.

The outer capsid proteins VP2 and VP5 tend to form stronger interactions with VP7 than they do with one another, with VP5-VP7 interactions appearing stronger than VP2-VP7 interactions (Nason *et al.* 2004). Thus, VP2 can be removed easily from the virus during uncoating due to its weak interactions with VP5 or alternatively, due to its interactions with the VP7 layer being weaker interactions than those observed for VP5 (Nason *et al.* 2004). This is consistent with previous observations showing that VP2 can be dissociated from the virions without the removal of VP5 (Verwoerd *et al.* 1972; Huismans *et al.* 1987c).
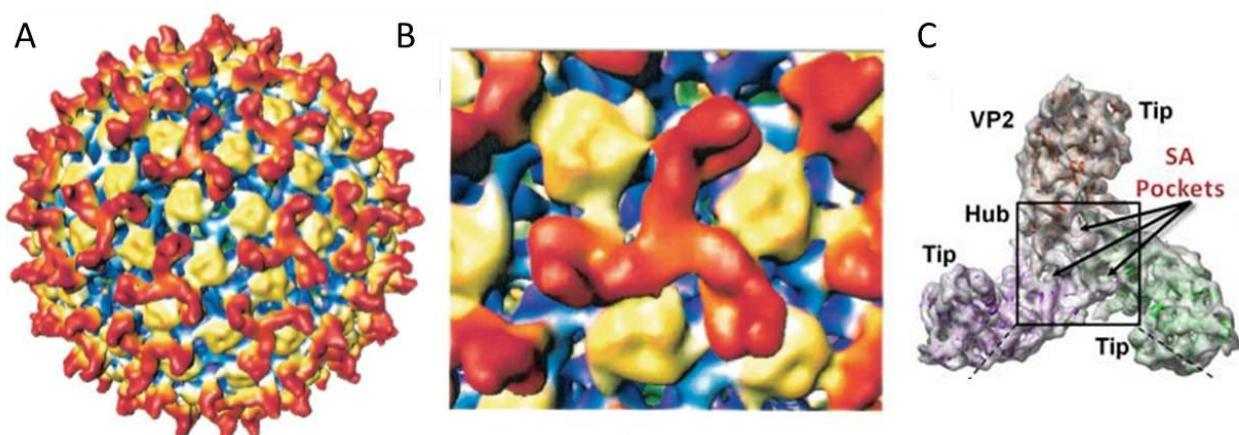
Fig. 2 The BTV virion is shown in (A) with an enlargement thereof shown in (B). The two distinct motifs of the outer layer are clearly visible in (B) with the triskelion propellers (VP2) highlighted in red and the interspersed globular domains (VP5) highlighted in yellow. The underlying VP7 layer is highlighted in blue. (C) Top view of the density map of a VP2 triskelion. The tip domains branch out from a central hub domain (Nason *et al.* 2004; Zhang *et al.* 2010).

Thus, each viral component is important for orbivirus structural organisation with each also having functional significance in the viral replication cycle, knowledge of which is important if one is to understand and study the control of disease.

1.4 Orbivirus replication cycle

This section gives an overview of the orbivirus replication cycle, with special mention being made to BTV as it is the prototype virus of the *Orbivirus* genus (Fig. 3). Any differences in AHSV are highlighted where necessary.

1.4.1   Viral adhesion, entry and uncoating

Virus entry into a host cell requires a number of steps culminating in the release of the viral genome into the cytosol (Forzan *et al.* 2004). This usually takes place by cell attachment followed by the induction of virus uptake by the host cell (Patel and Roy 2014). In general, for animal viruses, this requires the recognition of cellular receptors (which are likely to be glycoproteins) by viral attachment proteins, as well as their association with various coreceptors prior to virus entry (Hassan and Roy 1999).
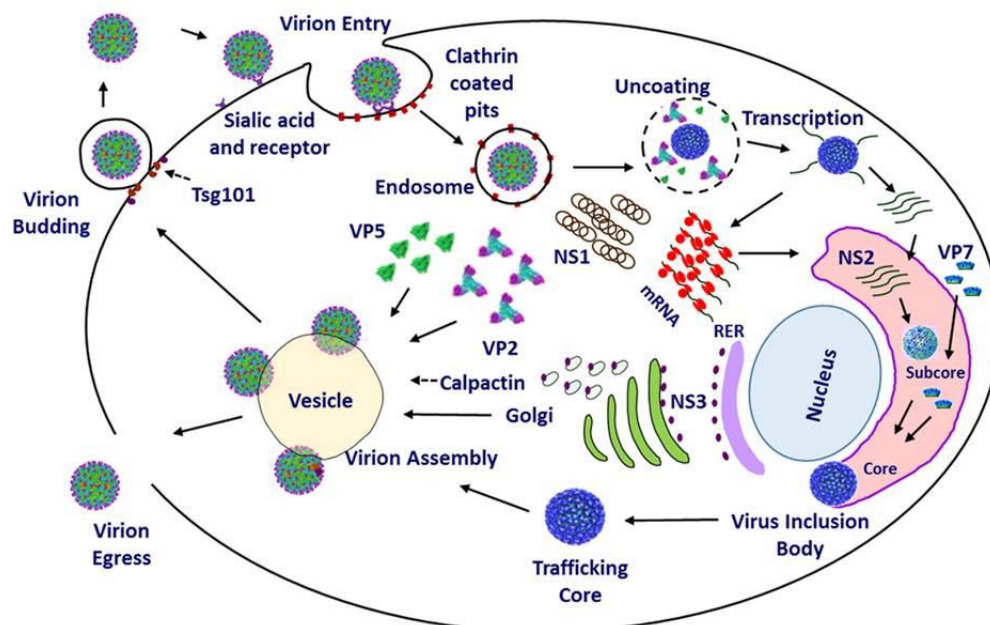
Fig. 3 Diagram representing an overview of the BTV replication cycle. Virus adsorption occurs via VP2 binding to sialic acid and a receptor on the host cell surface. This is followed by entry into the cell via varying mechanisms depending on the virus serotype or cell type in question. The virion is then trafficked to the endosome in which uncoating takes place. The transcriptionally active core is then released into the cytosol where viral transcription and translation take place leading to cellular morphogenesis by the non-structural proteins. NS1 forms tubules and NS2 forms the viral inclusion body (VIB) in which virus assembly takes place, after which VP2 and VP5 are added to form a complete virion. Egress of the mature virion follows via Tsg101 and NS3 mediated budding or via lysis of the host cell membrane (Patel and Roy 2014).

6

The haemagluttinin, VP2, is involved in viral attachment and entry into the cell (Hassan and Roy 1999). This protein appears to have two sites for plasma membrane binding, an inner sialic acid-binding site on the hub domain and an outer site on the tip domains (Zhang *et al.* 2010). The sialic acid interaction is not sufficient for cell entry and instead facilitates infection by stabilising the interaction of projections in the tip domains with a coreceptor on the cell surface (Zhang *et al.* 2010).

Although previously thought to enter the cell via clathrin-dependent endocytosis (Eaton *et al.* 1990; Forzan *et al.* 2007), BTV has recently been shown to also enter the cell via a clathrin-independent mechanism resembling macropinocytosis (Gold *et al.* 2010). The use of these mechanisms may be dependent on the serotype or cell line in question, for example, the study done by Forzan *et al.* (2007) focused on the entry of BTV-10 into Vero and HeLa cells, whereas the study done by Gold *et al.* (2010) focused on BTV-1 entry into BHK cells. In addition to this BTV is infectious in at least three different forms, each of which may use a different mechanism of entry into a cell (Mertens *et al.* 1996; Gold *et al.* 2010). In addition to the importance of endocytosis, entry into an acidic environment is also essential for successful viral infection (Forzan *et al.* 2007; Zhang *et al.* 2010).

Although not infectious in mammalian cells, the core particle is infectious in cells of *Culicoides variipennis* as well as KC cells, a *Culicoides*-derived cell line, thereby suggesting another route of infection with an alternate mechanism of cellular entry into insect cells (Grimes *et al.* 1995). This is important when considering that the virus is a vector-borne disease and needs a way in which to enter the insect cell. It has been suggested that VP7 may also be able to mediate attachment and membrane penetration, perhaps because it is the most exposed of the two core proteins (Mertens *et al.* 1996; Xu *et al.* 1997).

Following the recognition of cellular receptors by VP2 and the subsequent entry into the cell, BTV virions are delivered to endosomes (Forzan *et al.* 2007). Depending on the serotype and cell line, the virions may be delivered to early-endosomes, as in the case of BTV-10 infection (Vero and HeLa cells) or late endosomes/lysosomes, as in the case of BTV-1 infection (BHK cells) (Forzan *et al.* 2007; Gold *et al.* 2010). It is at this point, whilst in the endosome, that an essential step in the replication cycle takes place, namely virus uncoating – the separation of the inner core from the VP2/VP5 outer capsid (Forzan *et al.* 2007). VP2 anchors the virion to the endosomal membrane through receptor binding whilst environmental factors such as acidity and proteolysis modify its structure, perhaps by rearrangement or degradation, revealing VP5 which is otherwise blocked and inhibited by VP2 triskelions (Forzan *et al.* 2004; Forzan *et al.* 2007; Patel and Roy 2014). This allows low pH-dependent conformational changes to VP5 and the subsequent unmasking of two cytotoxic N-terminal amphipathic helices (Hassan *et al.* 2001; Nason *et al.* 2004). Thus, both the conformational changes and the cytotoxicity of VP5 make it possible for the protein to interact with

7

endosomal membranes causing the destabilisation thereof, and resulting in the release of the transcriptionally active core into the cytosol of the host cell (Hassan *et al.* 2001; Forzan *et al.* 2004; Forzan *et al.* 2007).

Once the endosomal membrane has been destabilised, VP5 is retained in the endosome while the transcriptionally active core is released into the cytosol, where it initiates transcription and viral protein synthesis (Huismans *et al.* 1987b; Eaton *et al.* 1990; Forzan *et al.* 2007).

1.4.2   Viral genome transcription, translation and replication

Orbiviruses do not make use of host cell enzymes in viral transcription, rather making use of the enzymatic machinery enclosed in the viral core. Thus viral transcription by VP1, VP4 and VP6 takes place within the core. Another reason for this process taking place in the core is that it may prevent the host cell from eliciting an immune response against the foreign material (Eaton *et al.* 1990; Diprose *et al.* 2002).

VP1 functions as the viral polymerase, VP4 acts in the capping of the viral mRNA and VP6 functions as a helicase (Urakawa *et al.* 1989; Stauber *et al.* 1997; Ramadevi *et al.* 1998). VP6 unwinds dsRNA, after which the negative strand is used as a template for the transcription of positive sense single-stranded mRNA by VP1, which is then capped and methylated by VP4, before extrusion into the cytoplasm. The viral mRNAs can then be translated into the structural and non-structural viral proteins. The interactions between VP1 and VP4 are quite stable and may be necessary for the capping of the mRNA. Recently it has been shown that NS1 may be a positive regulator of this viral protein synthesis (Boyce *et al.* 2012). In addition to this the BTV core binds dsRNA, perhaps in an effort to prevent the dsRNA released from damaged particles from eliciting a host response (Diprose *et al.* 2002).

In addition to its function as a viral polymerase (Urakawa *et al.* 1989), VP1 is also involved in the synthesis of dsRNA genome segments from plus-strand RNA templates by acting as a replicase (Urakawa *et al.* 1989; Boyce *et al.* 2004). Thus in addition to being templates for the translation of viral proteins, the extruded single-stranded mRNA also serves as templates for negative strand synthesis, resulting in progeny dsRNA genome segments, and the subsequent incorporation of the full dsRNA genome into the core of the newly formed virion (Grimes *et al.* 1998).

1.4.3   Viral assembly

Perinuclear viral inclusion bodies (VIBs) are the sites of BTV assembly and subsequent release of newly synthesised BTV particles into the surrounding cytoplasm of the infected cell (Eaton *et al.* 1987; Brookes *et al.* 1993). The non-structural protein NS2, is synthesised in relatively large amounts, phosphorylated, and forms a large component of the VIBs (Huismans *et al.* 1987a). Due

8

to its ability to bind ssRNA, NS2 may be involved in the recruitment of newly transcribed mRNA to VIBs prior to interactions with VP1, VP4 and VP6 within the VIB matrix and subsequent encapsidation by VP3 (Huismans *et al.* 1987a; Roy 2005). Due to its nucleic acid-binding regions, VP6 may also be involved in virus assembly by interacting with the 10 mRNA segments (Stauber *et al.* 1997), thereby assisting in the synthesis of core particles containing the full complement of dsRNA segments.

Virion assembly involves the minor structural proteins VP1, VP4 and VP6, the core proteins VP3 and VP7 (located in the VIB matrix), and the outer capsid proteins VP2 and VP5 (located at the periphery of the VIB) (Roy 2005). It is believed that the assembly of the BTV capsid starts with the assembly of the VP3 decamers followed by the incorporation of VP1 and VP4 which form a flower-shaped structure attached to the underside of the VP3 layer, so that both proteins come into contact with VP3 (Nason *et al.* 2004; Roy 2005). The viral genome then wraps itself around the VP1/VP4 complex, with which VP6 may be associated as the VP3 subcore assembles. VP3 forms a permanent scaffold and in so doing determines the eventual size of the core (Grimes *et al.* 1997). Core assembly is then completed by 260 VP7 trimers associating with the VP3 layer, via hydrophobic residues on the flat underside of the trimers (Grimes *et al.* 1998). Two models for the incorporation of VP7 into the core particle have been suggested. The first suggests that preformed hexamers of VP7 bind around the initial trimer at a single nucleation site. The other suggests that multiple nucleation sites may be present leading to strong interactions between VP7 trimers and the VP3 scaffold. Weaker interactions then fill in the gaps between the two (Limn and Roy 2003).

Once the core has been assembled, the outer capsid proteins VP2 and VP5 attach to the VP7 layer to form an intact virion, after which the virions are no longer transcriptionally active (Roy 2005). The newly formed intact virions are then ready for release from the host cell.

1.4.4   Virus release

BTV virions are assembled at the VIB periphery and are then released into the surrounding cytoplasm after the addition of VP2 (Brookes *et al.* 1993). Alternatively, it has been suggested that VP2, VP5 and NS3/NS3A bind to the negatively charged lipid phosphatidylinositol(4,5) bisphosphate [PI(4,5)P2] present in membrane lipid rafts via SNARE (soluble *N*-ethylmaleimide-sensitive fusion attachment protein receptor) domains to bring the newly assembled cores and outer capsid proteins together to form mature virions in a manner in which particle maturation and egress could be coupled (Bhattacharya and Roy 2008; Patel and Roy 2014). Interestingly, it appears that both VP2 and VP5 need to have been incorporated into the virion before it is able to associate with the cytoskeleton in a stable manner (Eaton *et al.* 1990; Hyatt *et al.* 1993).

Orbiviruses are non-enveloped and lack the glycosylated proteins used by enveloped viruses in viral egress. Thus such viruses have had to adopt other mechanisms of virus exit. BTV release can take place in one of two ways. Firstly, virus particles can bud through the plasma membrane. This non-lytic process occurs mainly early in infection and the viral particles acquire a temporary membrane (Eaton *et al.* 1990; Roy 2001). It appears that this non-lytic budding may be facilitated by NS3/NS3A interacting with Tsg101 (tumour-susceptibility gene 101 protein) a component of the endosomal sorting complex required for trafficking (ESCRT) pathway (Wirblich *et al.* 2006). Alternatively, virus particles can be released from the cell in a lytic manner, through a disrupted plasma membrane (Hyatt *et al.* 1989; Eaton *et al.* 1990). AHSV infected mammalian cells exhibit morphological changes that eventually result in cell death, whereas no observable cytopathic effect (CPE) has been observed in infected insect cells (Martin *et al.* 1998; Wirblich *et al.* 2006). Thus it has been suggested that a non-lytic form of release such as viral budding is more common in infected insect cells, whilst lytic release through a disrupted plasma membrane is more common in mammalian cells.

NS3/NS3A is localised in the plasma membrane, especially at sites of viral egress, as well as in intracellular smooth surface vesicles (Hyatt *et al.* 1991; Stoltz *et al.* 1996). Viruses acquire transient membranes from regions of the plasma membrane that have NS3/NS3A present, thereby suggesting a possible function in release. Furthermore, in a study using recombinant baculoviruses, NS3/NS3A was found to mediate the release of virus-like particles (VLPs) from Sf9 insect cells (Hyatt *et al.* 1993). This study also showed that VLPs interact with the cytoskeleton. The ability of BTV to bind to intermediate filaments through one or both outer capsid protein may facilitate the interaction of viruses with NS3/NS3A localised in smooth membrane vesicles, which can then be transported to the plasma membrane before the release of BTV from the cell (Hyatt *et al.* 1993).

It was previously suggested that NS3/NS3A may take advantage of the host cell's exocytotic pathway to facilitate the non-lytic release of virus particles from insect cells, by forming a complex (at its N-terminal) with cellular protein S100A10/p11, the calpactin light chain of the Annexin II complex involved in exocytosis (Beaton *et al.* 2002). This study also illustrated that NS3/NS3A is able to interact with VP2 at its C-terminal. It has subsequently been shown with the use of a reverse genetics system that NS3, but not NS3A, is required for assembly and virus trafficking in mammalian cells, but both are required in insect cells, thereby indicating a possible explanation for the expression of both proteins in orbiviruses (Celma and Roy 2011). This NS3-S100A10/p11 complex may form part of a larger active but nonlytic, egression process by acting as a bridge between virus particles and the host cell's export machinery (Patel and Roy 2014). Also, AHSV NS3 can act as a viroporin by altering membrane permeability and as such facilitate virus release and total virus yield (Meiring *et al.* 2009).

Together with NS3, NS1 may also play a role in the cytopathic properties of the virus and may be a major determinant of pathogenesis (Owens *et al.* 2004; Meiring *et al.* 2009). BTV, AHSV and EHDV NS1 spontaneously assemble into abundant cytoplasmic tubules that can be observed as early as 2-4 hours post infection (hpi) (Huismans and Els 1979). Thereafter these tubules are associated with virus particles and virus factories later in the infection cycle. Furthermore changing the ratio between NS1 and NS3 could result in a shift in release from lytic to nonlytic budding (Owens *et al.* 2004). The newly discovered BTV protein NS4 was also observed to be associated with the plasma membrane late in infection, and may be involved in virus exit (Belhouchet *et al.* 2011).

A defence mechanism has recently been proposed for the facilitation of non-lytic viral release of AHSV in insect cells (Venter *et al.* 2014). This study showed the presence of viral material, including viral particles, in vesicle-like structures that merged with the plasma membrane to release their contents, and in so doing facilitated non-lytic release in insect cells. By comparing both mammalian and insect cells infected with AHSV, this study also provided evidence that a non-lytic form of release is more common in insect cells, whereas lytic release is more common in mammalian cells.

Major structural protein VP7 is the main focus of this study, and will be discussed in more detail in the section that follows.

1.5 Viral protein 7

This section deals with the structure and properties of BTV VP7, and the unique characteristics of AHSV VP7, followed by a discussion of previously constructed AHSV VP7 mutants and their use as tools for the study of the protein.

1.5.1   BTV VP7

VP7 is a major structural protein and the group specific antigen of BTV (Huismans and Erasmus 1981). Encoded by gene segment 7, BTV VP7 is 349 amino acids (~38.5 kDa) in length (Yu *et al.* 1988). In the absence of other BTV proteins BTV-10 VP7 oligomerises into trimers when expressed in insect cells by means of recombinant baculoviruses (Basak *et al.* 1992). These trimers are composed of three VP7 monomers, each of which is composed of two domains (Fig. 4). The top domain forms the outer layer of the core and consists of amino acids 121-249, folded into a β-sheet. The trimeric top domains of both AHSV and BTV VP7 are structurally very similar to one another and are flanked by bottom domains (amino acids 1-120 and 250-349), composed of α-helices and long extended loops (Basak *et al.* 1996). The bottom domain interacts with the underlying VP3 layer at its base, while its sides interact with flanking VP7 trimers (Grimes *et al.*

11

1995). These two domains orientate themselves in such a way around the three-fold axis that the top domain of one monomer interacts with the bottom domain of another in the trimer.
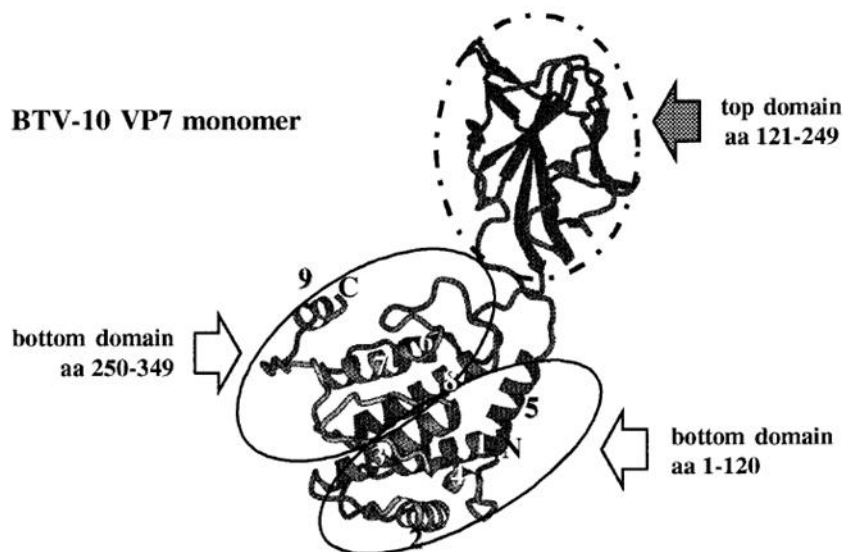

Fig. 4 A schematic of the BTV-10 monomer composed of two domains, namely the top β-sheet domain (aa 121-249) and the larger α-helical bottom domain. The latter is composed of the C-terminal (aa 1-120) and the N-terminal (aa 250-349) and the helices of the bottom domain are labelled 1 through 9 (Monastyrskaya *et al.* 1997).

The bottom domain is composed of 9 helices that are tightly packed in a somewhat complex fashion, with 5 helices located in the N-terminal and the remaining 4 located in the C-terminal region (Fig. 4). A hydrophobic core composed of a 4-helix bundle (helices 1, 3, 7 and 8) is located within the bottom domain of each VP7 monomer (Grimes *et al.* 1995). The base of the VP7 trimer is composed largely of helix 2 in addition to the flexible loops leading to and from this helix. This results in a largely flat surface housing a number of hydrophobic side chains. The residues of the helix 2 are highly conserved among BTV, AHSV and EHDV, thereby indicating their functional significance (Grimes *et al.* 1995; Grimes *et al.* 1997; Limn and Roy 2003).

The connections between the top and bottom domains of both BTV and AHSV VP7 trimers are quite weak (Basak *et al.* 1996), but the interactions between the monomers are extensive, leading to robust trimeric building blocks (Grimes *et al.* 1995). Grimes *et al.* (1995) postulated that the C-terminal residues from 333 onwards play an important role in the interactions between trimers. Of the residues of BTV-10 VP7, these residues are the furthest from the molecular 3-fold axis and form a highly flexible hydrophobic loop and the final α-helix of the molecule. The amino acids P338 and A346 preceding helix 9 of the bottom domain (residues 341-347) are essential for trimer-trimer interactions during core assembly (Limn and Roy 2003). These residues are part of a hydrophobic and flexible loop, and may be able to adopt different conformations to stabilise side-to-side interactions between the different trimers. The α-helical domain curves laterally in order to interact

12

with a neighbouring trimer. Such interactions are what hold together the network of VP7 trimers. Furthermore, the α-helical domains extend inwards to interact with the VP3 layer (Grimes *et al.* 1997).

The VP7 layer of the core is composed of multiple repeats of a group of icosahedrally independent copies of VP7, with each group consisting of 13 icosahedrally independent copies of VP7 (Fig. 5), in the form of five trimers, four of which are located in general positions, whilst the fifth is located with its three-fold axis aligned with the icosahedral three-fold axes, thereby contributing a monomer to each group (Grimes *et al.* 1998). These trimers were first designated as a, b, c, d and e (Prasad *et al.* 1992) and later re-described as P, Q, R, S and T (Grimes *et al.* 1997).

As indicated in Figure 5, the P trimer is located close to the icosahedral fivefold axis, trimer S is adjacent to the icosahedral twofold axis and trimer T is located on the icosahedral threefold axis (Grimes *et al.* 1997). T trimers appear to be the most tightly attached of the trimers and appear to be the first to attach to the VP3 layer. The symmetry of the VP3 and VP7 layers match at this point thus the T trimers are well-placed to act as nucleation points for the binding of VP7 timers to the VP3 subcore (Grimes *et al.* 1998). The P trimer attaches last and is the most distant from the icosahedral three-fold axes, making the least favourable contacts (Grimes *et al.* 1998).
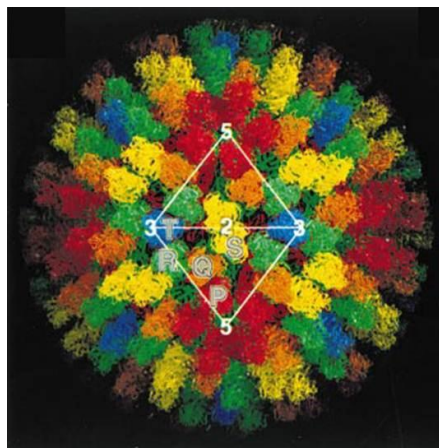

Fig. 5 The architecture of the VP7 layer of the BTV core. The icosahedral asymmetric unit is composed of 13 copies of VP7(T13) arranged as 5 trimers, namely P (red), Q (orange), R (green), S (yellow) and T (blue) (Grimes *et al.* 1998).

1.5.2 AHSV VP7

Also encoded by segment 7, AHSV VP7 is 354 amino acids (~38.1 kDa) in length (Yu *et al.* 1988). The segment 7 nucleotide sequence is highly conserved in the 9 serotypes of AHSV (Bremer *et al.* 1990) and is also closely related to BTV segment 7 (Roy *et al.* 1991). In particular it is the amino-

and carboxyl- terminals that share the highest levels of sequence homology between AHSV-4 VP7 and the BTV-10 VP7, the sequence similarity of which is 44% (Roy *et al.* 1991).

Although both AHSV and BTV VP7 proteins have quite a number of hydrophobic amino acids, including alanine, methionine and proline, AHSV VP7, in contrast to BTV VP7, is highly hydrophobic and insoluble (Roy *et al.* 1991; Basak *et al.* 1996). It is perhaps as a result of this that in addition to being incorporated into AHSV core particles, AHSV VP7 also self-assembles into flat, hexagonal crystalline-like particles in AHSV infected cells or when expressed in insect cells by means of a recombinant baculovirus (Chuma *et al.* 1992; Burroughs *et al.* 1994). This characteristic is unique to AHSV VP7, and no similar crystals ever result from BTV VP7 expression.

These crystalline-like particles were observed in both the cytoplasm (Fig. 6A) and rarely, in the nucleus (Fig. 6B) of AHSV infected monkey kidney (MS) and Vero cells and were first described by Breese in 1969 as "lamellar material" or "intracellular inclusions without internal material" (Breese and Ozawa 1969; Breese *et al.* 1969). Some two decades later Chuma *et al.* (1992) observed recombinant baculovirus expressed disc-shaped VP7 crystals under the light microscope (Fig. 6C) (Chuma *et al.* 1992). These crystals were visible under the TEM (Fig. 6C) and had a maximum diameter of 25 µm and length of 250 µm and typically with between one and three crystals present per cell.

Although Chuma *et al.* (1992) observed what they termed disc-shaped crystals, the authors did not investigate their fine structure. Thus, Burroughs *et al.* (1994) sought to do just that in what was the first study to report the purification and characterisation of such crystals from orbivirus infected cells (Burroughs *et al.* 1994). AHSV-9 VP7 assembled into large, mainly hexagonal crystals (Fig. 6E) in BHK-21 cells (Burroughs *et al.* 1994). Composed solely of AHSV VP7, these large structures had a crystalline appearance when viewed under the light microscope. Electron microscopy showed that the structures had a "highly ordered two-dimensional crystalline lattice (Fig. 6F) consistent with a dimeric or trimeric subunit structure". However, in contrast to what was observed by Chuma *et al.* (1992), the structures described by Burroughs *et al.* (1994) had a maximum diameter of 8 µm.
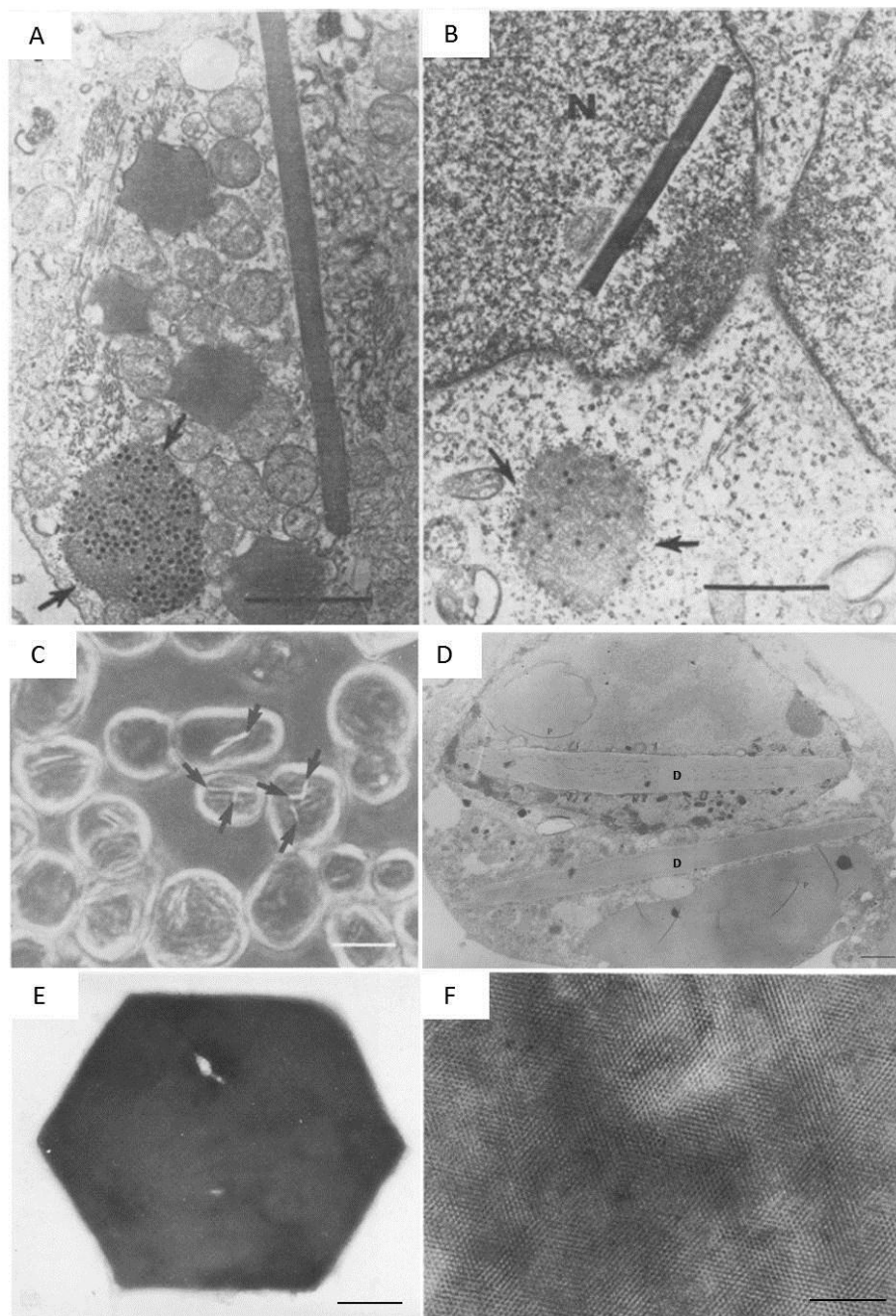
Fig. 6 Electron and light micrographs obtained in the characterisation of AHSV VP7. TEM micrographs of intracyctoplasmic and intranuclear inclusions within AHSV-infected MS cells are shown in (A) and (B) respectively (Breese and Ozawa 1969). The micrographs in (C) and (D) show "disc-shaped crystals" expressed in Sf9 cells by means of a recombinant baculovirus expressing AHSV VP7 (Chuma *et al.* 1992). A purified AHSV VP7 crystalline-like particle is shown in (E), with the surface thereof at a higher magnification shown in (F) (Burroughs *et al.* 1994). N = nucleus. D = disc-shaped crystal. Scale bars represent 1 μm (A, B), 250 μm (C), 1 μm (D), 260 nm (E) and 104 nm (F).

Similar structures to those described by Breese *et al.* (1969) have been observed in AHSV-infected Vero (Fig. 7A and B) and KC cells (Fig. 7C and D) viewed under the TEM (Venter *et al.* 2012; Venter *et al.* 2014). Immunogold labelling using VP7 specific antibodies confirmed that these crystalline-like particles represented the hexagonal crystalline-like AHSV VP7 particles purified by

15

Burroughs *et al.* (1994) (Fig. 7C) and TEM micrographs taken at high magnification showed that the particles have a sheet-like appearance (Fig. 7D) similar to the "highly ordered two-dimensional crystalline lattice" of purified VP7 crystals.
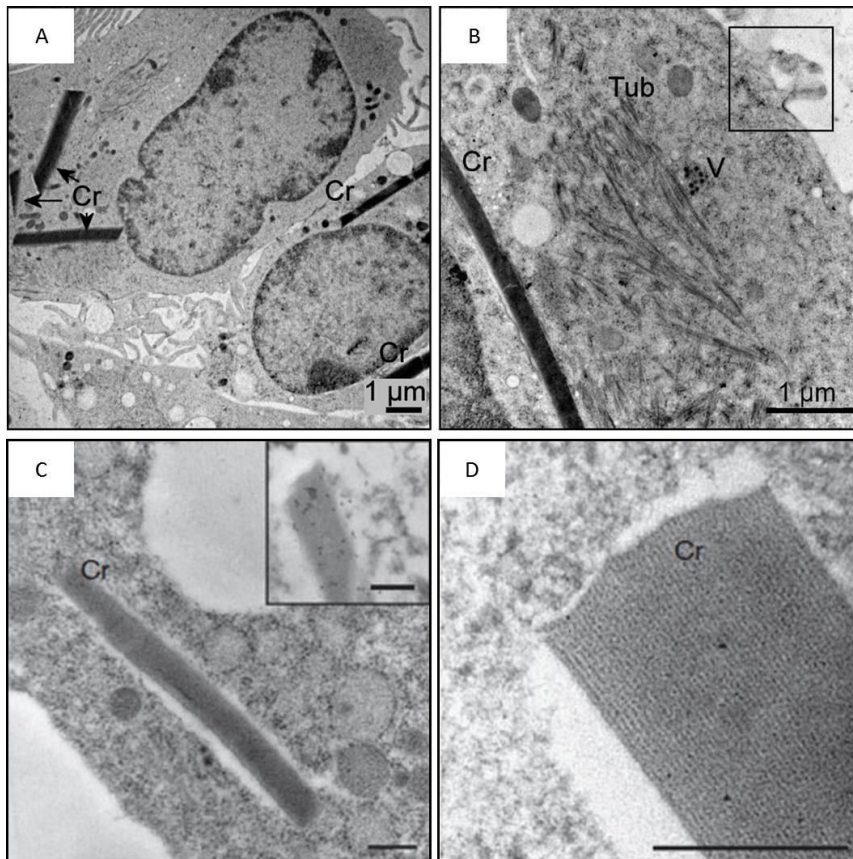

Fig. 7 TEM micrographs of AHSV-infected Vero (A, B) and KC (C, D) cells. AHSV VP7 crystalline-like particles are indicated by Cr. The insert in C shows positive immunogold labelling of the particles with anti-VP7. Tub = NS1 tubules and V = AHSV virions. Scale bars represent 1 µm (A, B), 2 µm (C) and 500 nm (D and insert) (Venter *et al.* 2012; Venter *et al.* 2014).

At times, mature virions or NS1 tubules were observed in close proximity to the AHSV VP7 crystalline-like particles (Breese *et al.* 1969; Venter *et al.* 2014), the significance of which has yet to be established. Furthermore, the importance of these unique crystals is unknown. Thus, these studies have highlighted the need to elucidate the nature of the interactions that control the self-assembly of the VP7 protein into either crystals or alternatively their incorporation into AHSV core particles.

The crystal structure of the top domain of AHSV has been particularly useful in studies of BTV and AHSV VP7 solubility (Basak *et al.* 1996). In particular it was shown that AHSV VP7 residues Ala-167 and Phe-209 increase the hydrophobicity of the protein, and were suggested as candidates for mutations aimed at increasing the solubility of AHSV VP7, specifically an Ala-167-Arg change (Basak *et al.* 1996). The equivalent residues in BTV are Arg-168 and Thr-209 respectively, with

16

Arg-168 located in a hydrophilic region running along the edge of BTV VP7. These observations led to the hypothesis that the distribution of amino acid residues in the top domain of AHSV VP7 may be responsible for the overall insolubility of the protein (Basak *et al.* 1996). To determine whether or not this is indeed the case, chimeric VP7 proteins were constructed whereby the top domain of BTV-10 (B) was substituted with the structurally similar AHSV-4 VP7 top domain (A) and vice versa, resulting in the chimeras BAB VP7 and ABA VP7 (Basak *et al.* 1996; Monastyrskaya *et al.* 1997). These chimeras were able to form trimers, but both did not form core-like particles (CLPs) when co-expressed with BTV VP3 thereby suggesting that VP7 trimerisation is not enough for CLP formation. The chimera ABA VP7, containing the BTV-10 top domain, was more soluble than BAB VP7, containing the AHSV-4 top domain, confirming that the top domain contributes to the insolubility of AHSV VP7 (Basak *et al.* 1996; Monastyrskaya *et al.* 1997).

The BTV Arg-168-Gly-169-Asp-170 (RGD) motif is involved in the attachment of BTV VP7 to a cell surface receptor, most likely an integrin, and at the very least is part of the receptor binding sequence of BTV cores (Tan *et al.* 2001). Located in a loop of the BTV VP7 top domain, this domain is accessible on the surface of the VP7 molecule and as such has no effect on the interactions between VP3 and VP7. Despite its exposed position on the core, the RGD motif is conserved in almost all known orbivirus VP7s (Grimes *et al.* 1995). In AHSV, Ala-167-Gly-168-Gln-169 (AGQ) is found at the equivalent position of the BTV RGD motif and is thought unlikely to play the same role as the BTV RGD motif (Basak *et al.* 1996). A RGD motif has however been found in AHSV VP7, but it is located elsewhere at residues 178-180 of the highly flexible loop encompassing residues 175-180. This flexible loop is located at the lower part of the top domain and appears to be less accessible to integrins than the AGQ segment of AHSV. Tan *et al.* (2001) mutated the BTV RGD motif to AGQ and this mutant was still able to form trimers. Furthermore, it was found that alterations to the RGD motif do not affect the antigenic and biochemical properties of VP7.

Interestingly, the Ala-167 residue suggested for mutation by Basak *et al.* (1996) is found in the AGQ motif of AHSV VP7. By making single amino acid substitutions at positions 167 and 209 of the BAB VP7 chimeric protein Monastyrskaya *et al.* (1997) investigated the possible role of Ala-167 and Thr-209 in solubility. Alanine (A) at position 167 was replaced by arginine (R) as that is the equivalent BTV residue at position 168 of BTV-10 and phenylalanine (F) at position 209 was replaced by threonine (T). Furthermore, BTV Arg-168 forms part of the RGD motif, which is located in an area associated with the C-terminal helix 9 of an adjoining VP7 monomer (Basak *et al.* 1996). Both substitutions increased the solubility of the BAB chimeric protein but not the wild type (WT) AHSV-4 VP7 protein. It was suggested that the lower solubility of AHSV mutant A167R may indicate the importance of the C-terminal helix 9. This is so as the C-terminal of AHSV VP7 is more hydrophobic than that of BTV VP7, with L346 replacing R345 of BTV VP7.

Monastyrskaya *et al.* (1997) also created chimeras that could be used to study the interactions between helices in the bottom domain. One such chimera was BBA VP7, composed of the chimera ABA VP7 which was altered to contain the N-terminal α-helices 1 to 5 of BTV-10 instead of AHSV-4. Unlike the chimera ABA VP7, BBA VP7 was shown to aggregate and lost its conformational epitopes, thereby indicating that the protein was not correctly folded, perhaps due to an arginine replacing an isoleucine residue (I251) at the junction site disrupting the protein structure. Similarly, the chimera ABB VP7 was constructed by replacing the 4 C-terminal helices of chimera ABA VP7 with those of BTV-10 VP7. This alteration also led to incorrect protein folding, no trimer formation and protein aggregation. Thus the differences between the N- and C-terminals of BTV-10 and AHSV-4 VP7, although minor, are significant enough to abolish trimer formation.

Recent modifications to AHSV VP7 have enabled investigations into its potential use as an antigenic delivery and display system.

1.5.3   Minor AHSV VP7 modifications

The use of AHSV VP7 as an antigen delivery and display system has recently been investigated by Rutkowska *et al.* (2011). An important factor in the development of such a system was the solubility of AHSV VP7, which normally is highly hydrophobic and insoluble (Basak *et al.* 1996). Three distinct hydrophilic, surface exposed β-loops at amino acids 144-145, 175-180 and 200-201 (Fig. 8A) were identified by crystallographic studies of the AHSV VP7 top domain and targeted for the insertion of foreign peptides (Rutkowska *et al.* 2011). Amino acids 175-180 form a flexible loop containing an RGD motif (Basak *et al.* 1996).

To this end, 18 nucleotide DNA fragments were inserted downstream of the codons encoding amino acids 144, 177 and 200 respectively. This generated multiple cloning sites in the VP7 top domain and specified the restriction enzyme sites *Hind*III, *Xba*I and *Sal*I and encoded the amino acids KLRSVD. These modified genes were used to express the VP7 vector proteins VP7-177 and VP7-200 (Fig. 5B) via recombinant baculoviruses. In addition to this an 18 nucleotide fragment specifying the restriction enzyme sites *Sma*I, *Eco*RI and *Xho*I*,* and encoding the amino acids PGEFLE, was inserted downstream of amino acid 144, leading to the expression of the vector protein VP7-144 (Fig. 5B).
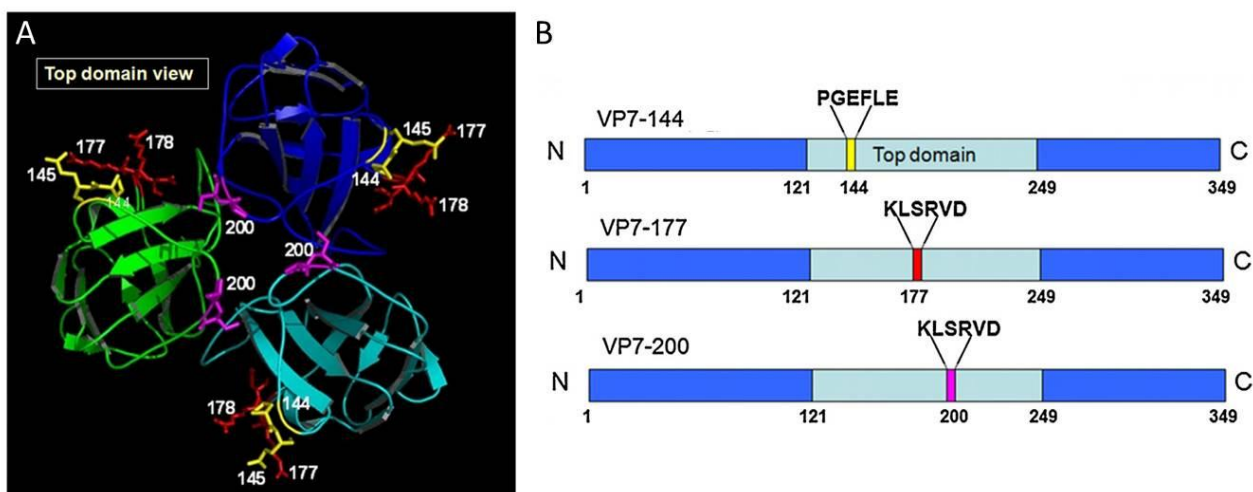
Fig. 5 A representation of the crystallographic structure AHSV VP7 top domain is shown in (A) (looking vertically into the top of the VP7 trimer). The three VP7 monomers are indicated in green, blue and cyan. The hydrophilic sites targeted for mutation are indicated in yellow at position 144-145, red at position 177-178 and in magenta at position 200-201. The three vector proteins are shown in (B), with the amino acid inserts indicated above each protein at the insertion site (Rutkowska *et al.* 2011).

The effect of these insertions on solubility and particle formation was investigated and showed that the insertion downstream of amino acid 144 led to a largely soluble protein, with about 60% of the expressed protein in the soluble fraction. The insertion downstream of amino acid 177 increased the solubility to about 30%, while the insertion downstream of amino acid 200 had no effect on solubility. Thus the effect of these insertions was both insert and site specific.

AHSV VP7 trimers can be distinguished from the monomer, provided that the sample is not heated before electrophoresis (Monastyrskaya *et al.* 1997). By incubating samples at room temperature rather than at 95˚C before electrophoresis, Rutkowska *et al.* (2011) showed that the soluble fractions of all three vector proteins electrophoresed to the position expected of an AHSV VP7 trimer. This was confirmed by sedimentation analyses similar to those performed by Limn *et al.* (2000) whereby samples were compared to various size markers. Thus all three proteins could form trimers, their stability however was affected by the insertions. Monomers were also detected in all cases. The majority of expressed VP7-144 protein was trimeric. VP7-177 was found to be trimeric but to a lesser extent than both VP7-144 vector proteins. In the case of VP7-200 some trimers were observed, but the protein was found to be largely monomeric in nature.

The particulate fractions of the vector proteins VP7-144, VP7-177 and VP7-200 were analysed via SEM and compared to WT VP7 (Kretzmann 2006; Rutkowska *et al.* 2011; Rutkowska 2012). Figure 9 shows the layered, flat hexagonal, crystalline-like particles characteristic of WT VP7 (Fig. 9A). The insertion of PGEFLE downstream of amino acid 144, disrupted the self-assembly of the protein to such an extent that no particles were assembled (Fig. 9B). VP7-177 and VP7-200, on

19

the other hand, still formed somewhat hexagonal particles (Figs. 9C and D). These particles were however not as rigid as that of WT VP7.
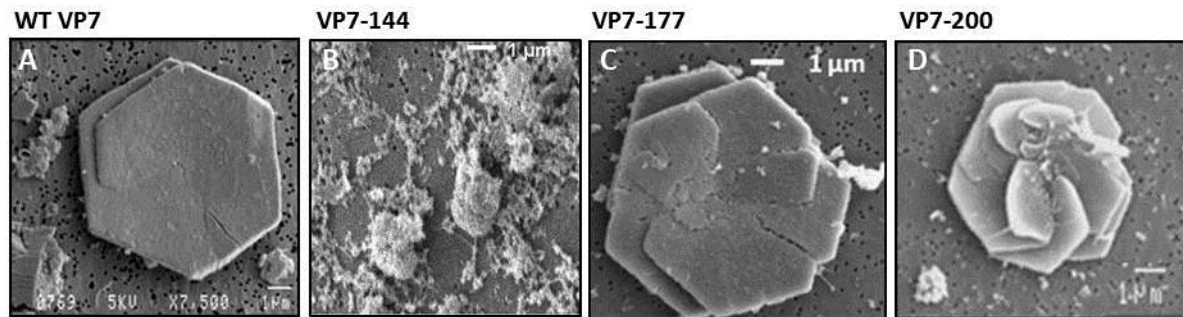

Fig. 9 SEM micrographs of the particles or protein aggregates formed by WT VP7 (A), VP7-144 (B) or VP7-177 (C), VP7-200 (D) when expressed in Sf9 insect cells by means of recombinant baculoviruses (Kretzmann 2006; Rutkowska *et al.* 2011; Rutkowska 2012). Scale bars represent 1 μm.

A few VP7 fusion proteins were constructed using these vector proteins, analysis of which showed that solubility is the most important determinant of a good insert specific immune response, thereby highlighting the need to increase the soluble fraction of VP7 fusion proteins. To this end, several fusion proteins were treated with non-ionic detergents such as TritonX 100 or Nonidet[®]P-40 (NP-40) to determine whether or not the solubility of the fusion proteins could be improved by chemical treatment (Rutkowska *et al.* 2011). In addition to this, the particulate fractions were treated with 1 M L-arginine, a mild, non-denaturing solubilisation agent (Golovanov *et al.* 2004; Ishibashi *et al.* 2005; Tsumoto *et al.* 2005), previously shown to extract correctly folded proteins from insoluble aggregates at higher concentrations (0.5 – 2 M) (Tsumoto *et al.* 2004). These reagents prevented or reversed aggregation and highlighted the advantage of presenting soluble antigens to the immune system in conjunction with such reagents (Rutkowska *et al.* 2011).

As an alternative method of increasing the solubility of AHSV VP7, the charge of the protein was altered by making a single amino acid substitution at sites 345 of WT VP7 and VP7-177 respectively (Rutkowska *et al.* 2011). This substitution involved changing the uncharged leucine to a positively charged arginine (VP7 L345R). This substitution increased the solubility of VP7 from less than 10% to 48%, and confirmed the prediction by Monastyrskaya *et al.* (1997) that the leucine-345 in the ninth C-terminal helix of the AHSV VP7 bottom domain contributes to the insolubility of the protein.

Although constructed in the hopes of developing AHSV VP7 as a vaccine display system, the three vectors can also be used as tools for, amongst others, the study of protein transport and self-assembly.

1.5.4 Major AHSV VP7 modifications

In addition to the minor modifications described above, large proteins have also been inserted into sites 144, 177 and 200 of the AHSV VP7 top domain, one protein of which was enhanced green fluorescent protein.

1.5.4.1 Enhanced green fluorescent protein

Bioluminescence is the process whereby light is emitted in an organism due to a chemical reaction involving the enzymatic oxidation of a substrate, by an enzyme (Zimmer 2002). Common bioluminescent organisms include marine animals and insects, and the light emitted by these organisms usually has one of three functions: defence, offence or communication. Of interest here are the green fluorescent proteins (GFPs) used by many organisms as energy-transfer acceptors in bioluminescence (Prasher *et al.* 1992; Prasher 1995).

Although GFPs are found in a number of organisms, the GFP isolated from *Aequorea victoria*, a jellyfish found in the Pacific Northwest, is the GFP that is commonly used as a biological marker (Prasher 1995; Zimmer 2002). In addition to this, this was the first GFP for which the gene was cloned (Prasher *et al.* 1992) and subsequently expressed and sequenced. The bioluminescence of *Aequorea* involves the protein aequorin (the luciferase) which contains coelenterazine (the luciferin). Upon binding three Ca^{2+} ions, and in the presence of oxygen, the luciferase oxidises the luciferin, producing a complex emitting blue light *in vivo*. This complex then undergoes radiationless energy transfer to GFP which emits green fluorescence. Alternatively Ca^{2+}-activated proteins can be used instead of the luciferase to activate GFP, as such proteins also produce energy during the oxidation of coelenterazine (Prasher *et al.* 1992).

The fluorescent chromophore of GFP appears to be formed by the cyclisation of residues 65-67 (Ser-Tyr-Gly). GFP has a unique 11 β-sheet barrel-like structure (Fig. 10), through which an α-helix runs diagonally to the barrel. The GFP chromophore is located in the centre of the 11 β-sheets and is linked by the α-helical stretch running through the centre of the barrel (Fig. 10). The chromophore is well protected from quenching by oxygen and attack by hydronium ions and is surrounded by a hydrogen-bonding network. Nearly the entire structure of GFP is required for chromophore formation and fluorescence. In particular, the folding of GFP into the β-barrel is thought to be crucial to the formation of the chromophore and the bioluminescence of GFP.

Fig. 10 The green fluorescent protein (GFP) monomer. The chromophore is located at the centre of the β-barrel (Nienhaus and Wiedenmann 2009).

Many variants of GFP have been constructed, examples of which include cyan fluorescent protein (CFP) and yellow fluorescent protein (YFP), in order to enhance brightness and improve pH resistance and have similar applications to GFP (Zhang *et al.* 2002). One such variant of GFP is enhanced green fluorescent protein (eGFP, 239aa), the structure of which has only recently been resolved and the role of Glu222 in the stabilisation of the chromophore cavity of eGFP highlighted (Cormack *et al.* 1996; Zhang *et al.* 1996; Royant and Noirclerc-Savoye 2011). EGFP has single amino acid substitutions at positions 64 (F64L) and 65 (S65T), both of which contribute to the enhanced fluorescent properties of the protein as amino acid 65 forms part of the chromophore whilst amino acid 64 is located proximally to the chromophore. These substitutions lead to better folding of the protein as well as to a protein that fluoresces about 35-fold more intensely in *E. coli* than the WT when excited at 488 nm (37°C). In addition to this, these mutations also led to a more soluble version of GFP. When constructing eGFP, several codons were replaced with those that are highly expressed in human proteins in order to improve the expression of eGFP in mammalian cells, thereby increasing the sensitivity of the protein (Zhang *et al.* 1996). EGFP is ideal for quantitative studies of intra- and intercellular protein dynamics using fluorescence microscopy (Cinelli *et al.* 2000). The fluorescence spectrum of this protein is not affected to any large extent by the environment and additional molecules or those molecules fused to eGFP.

There are many applications for GFP, such as its use in studying protein trafficking and mobility in live cells, examples of which are fluorescence correlation microscopy (FCS) and fluorescence resonance energy transfer (FRET) (Zhang *et al.* 2002; Zimmer 2002). Both GFP and eGFP have been used extensively in the study of viral protein transport and localisation, as such helping to elucidate the role of such proteins in the replication cycle. Although a DNA virus, papillomavirus is

22

also a non-enveloped virus with icosahedral symmetry and makes use of a similar entry mechanism to BTV and AHSV. Papillomaviruses have been difficult to study as they could not be propagated *in vitro.* The ability to generate *in vitro* infectious papillomavirus capsids has assisted in the study of this virus and GFP fusion proteins have also been especially useful. In a 2006 study, authors used L2-GFP mutants to determine the role of minor protein L2 in the egress of viral genomes from endosomes (Kamper *et al.* 2006). Using GFP tagged proteins studies on human immunodeficiency virus (HIV) type 1 have shown the role of Tsg101 in Gag trafficking and release (Goff *et al.* 2003). This protein is also implicated in the release of BTV and AHSV, and appears to be important in the sorting of cargo in the endosomal trafficking pathway.

Closer to the focus of this study, much work using eGFP tagged proteins has been done on rotavirus. Like BTV and AHSV, rotavirus is a member of the *Reoviridae* family and as such is a dsRNA virus. Examples of the use of eGFP in the study of this virus include the identification of amino acid residues essential for the interaction of VP1 with non-structural protein (NSP) 5, using eGFP tagged VP1 mutants (Arnoldi *et al.* 2007). A great deal of research has centred on rotavirus NSP4, the viral enterotoxin. Studies in recent years have utilised eGFP to study NSP4 and its role in Ca^{2+} homeostasis (Berkova *et al.* 2003; Berkova *et al.* 2006; Diaz *et al.* 2008), as well as its role in the organisation of the actin network (Berkova *et al.* 2007) to name but a few.

Thus, among its many functions, eGFP is a useful tool for the study of protein transport and localisation and also for the elucidation of the role of the viral proteins in the replication cycle.

1.5.4.2 AHSV VP7-eGFP fusion proteins

Due to the advantages discussed in the previous section, VP7-eGFP fusion proteins were previously constructed by members of this research group as tools for the study of AHSV VP7 trimerisation, solubility and transport (Mr T Seameco and Dr QC Meyer, personal information, (Mizrachi 2008)).

In order to construct these proteins, the sequence encoding eGFP (239 aa) was amplified using primers flanked with the necessary restriction enzyme sites. In the case of VP7-144-eGFP the primers were flanked with *Eco*RI (forward) and *Xho*I (reverse), and in the cases of VP7-177-eGFP and VP7-200-eGFP the primers were flanked with *Hind*III (forward) and *Sal*I (reverse). The VP7 vectors described by Rutkowska *et al.* (2011) (Section 1.5.3) were digested by the corresponding restriction enzymes and the eGFP amplicon inserted by directional cloning. This yielded constructs encoding the VP7-eGFP fusion proteins VP7-144-eGFP, VP7-177-eGFP and VP7-200-eGFP (Fig. 11) which were subsequently used to generate recombinant baculoviruses expressing these proteins.
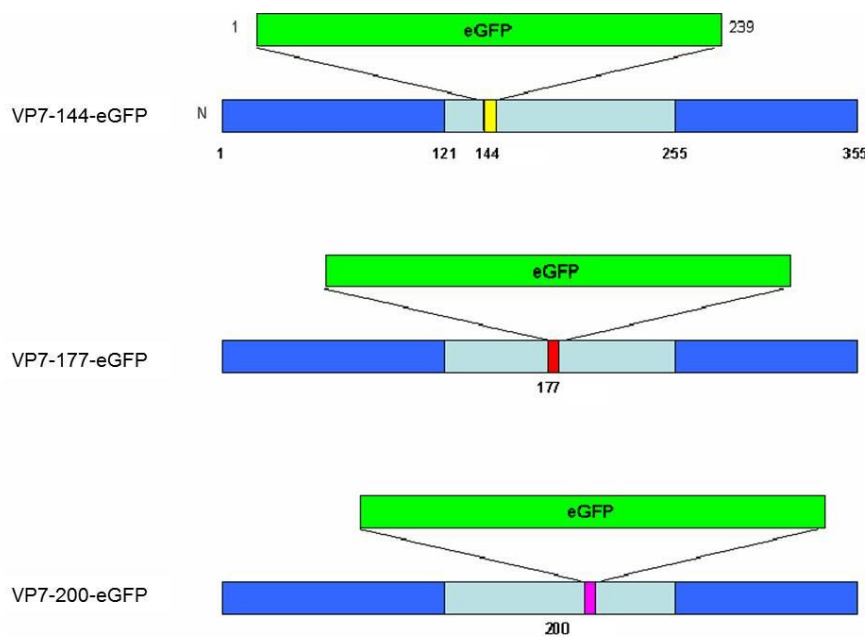
23

Fig. 11 Schematic representation of the VP7-eGFP fusion proteins whereby eGFP was inserted into sites 144, 177 or 200 of the AHSV VP7 top domain.

The fusion of eGFP to these proteins allows for their easy visualisation via a range of techniques. Thus these VP7-eGFP proteins serve as tools for the study of, amongst others, the transport and localisation of AHSV VP7.

1.6 Protein targeting/sorting in eukaryotic cells

A mammalian cell can contain up to 10, 000 different proteins, some of which remain localised in the cytosol but the majority are transported elsewhere in the cell, either to the surface for secretion or to other organelles or aqueous compartments (Lodish 2004). The transport of proteins to various locations within the cell is termed protein sorting or protein targeting, and needs to be quite specific in order for the cell to function correctly.

The non-secretory pathway involves protein targeting and translocation across the membranes of organelles (Lodish 2004). The specificity of protein targeting is controlled by signal sequences or uptake-targeting sequences within the N-terminal of the protein. The synthesis of secretory proteins begins on free cytosolic ribosomes after which a 16-30 amino acid endoplasmic reticulum (ER) signal sequence in the N-terminal of the nascent protein directs the ribosome to the rough ER membrane in a process known as cotranslational translocation (Lodish 2004). These signal sequences contain 6-12 hydrophobic amino acids (the core) adjacent to one or more positively charged amino acids. This hydrophobic core is essential to the functioning of the signal sequence and mutations to it can be detrimental to eventual location and function of the protein. Once at the ER, the growing polypeptide is translocated across the ER membrane into the ER lumen, after which the signal sequence is cleaved by signal peptidase and degraded (Lodish 2004). Secretory

24

proteins move through the translocation channel and cross the ER membrane completely whilst the hydrophilic regions of membrane proteins either cross the membrane or remain in the cytosol (Rapoport 2007). An energetically favourable process is usually coupled to the translocation event to ensure a unidirectional transfer of the protein into an organelle. Proteins lacking the ER signal sequence are synthesised on cytoplasmic ribosomes in the non-secretory pathway. The proteins that do not have targeting sequences are released from the ribosomes into the cytosol where they remain, whereas those proteins with organelle-specific targeting sequences are released into the cytosol before being transported to their target organelle, be it the mitochondrion, chloroplast, peroxisome or nucleus (Lodish 2004).

Largely dependent on transport vesicles, the secretory pathway on the other hand deals with the targeting of soluble and membrane proteins synthesised on the rough-ER to their final destinations. After the ER, proteins are transported to the Golgi apparatus where they undergo further processing as they are transported through the Golgi's discrete compartments. These compartments ensure that sorting and processing events occur in an organised and sequential manner through the Golgi apparatus (Cooper and Hausman 2007). Proteins are sorted for delivery to their final destinations upon arrival at the *trans*-Golgi network (TGN), the last compartment of the Golgi apparatus (Traub and Kornfeld 1997). Together, the ER and the Golgi apparatus sort and transport proteins destined for secretion, transportation to the plasma membrane and incorporation into lysosomes or endosomes. After transport to the TGN, modified proteins are transported to their final destinations through one of three branches of the secretory pathway, namely the constitutive secretory pathway, the regulated secretion pathway or via the third pathway involving transport of lysosome-destined membrane and soluble proteins to the lysosome (Traub and Kornfeld 1997; Lodish 2004).

In recent years, tunnelling nanotubes similar to the transport tubules found in plant cells have been described in animal tissue culture. Nanotubes from adjacent cells appear to coalesce when they meet, forming a cytoplasmic bridge between cells providing another avenue for protein transport in animal cells (Gallagher and Benfey 2005).

Other mechanisms in the cell complement this protein targeting and serve as further levels of organisation in the cell. One such level of organisation in the cell is the cytoskeleton, a network of protein filaments found throughout the cytoplasm of eukaryotic cells. The cytoskeleton provides the cell with a scaffold that provides a structural framework for determining cell shape, organelle positioning and the general organisation of the cytoplasm (Cooper and Hausman 2007). The cytoskeleton consists of three major protein filaments: actin filaments, intermediate filaments and microtubules (Cooper and Hausman 2007).

25

As reviewed by Ward (2011) intermediate filaments have no known motors utilising them for transport. In contrast to this, microtubules and actin have motor proteins that travel along them based on the utilisation of the energy released by the hydrolysis of adenosine triphosphate (ATP) (Ward 2011). The motor proteins use this energy to produce movement that can transport intracellular molecules such as proteins to different locations within the cell (Cooper and Hausman 2007). Myosin is the motor protein that moves along actin filaments. There are two classes of myosin, conventional and unconventional myosins, the latter of which have been observed to function in intracellular trafficking (Ward 2011). Microtubules are polar structures, with the minus end located at the microtubule organising center (MTOC) and the plus end located at the cell periphery (Ward 2011). The two motor proteins (kinesin and dynein) move in an antiparallel manner along microtubules with the kinesins moving toward the plus end and the dyneins moving toward the minus end (Smith and Enquist 2002; Cooper and Hausman 2007). This allows for cargo to be transported in opposite directions within the cytoplasm, either toward the cell periphery or toward the nucleus (Smith and Enquist 2002; Cooper and Hausman 2007).

In addition to transporting membrane vesicles in the secretory and endocytic pathways, one of the major roles of microtubules is to transport macromolecules and organelles through the cytoplasm (Cooper and Hausman 2007). By transporting membrane-enclosed organelles such as the ER, Golgi apparatus, lysosomes and mitochondria within the cell, microtubules are also responsible for their eventual location within the cell.

Although the cell has developed sophisticated protein targeting pathways there are also instances in which the protein never reaches its target site, perhaps due to protein misfolding and aggregation and the subsequent exhaustion of the mechanisms in place to deal with such proteins.

1.7 Protein misfolding and aggregation

In order for a protein to be fully functional it needs to be correctly folded into its distinct 3-dimensional structure or native fold (Tyedmers *et al.* 2010). This is so as only correctly folded proteins are stable in the cellular environment and are able to interact with their target molecules (Dobson 2003). In addition to this, there are many cellular processes, such as trafficking and secretion that are dependent on correct protein folding.

It is the kinetic competition between folding and aggregation that determines whether or not a protein will be correctly folded (Garcia-Mata *et al.* 2002). In many cases protein misfolding occurs due to mutations, as well as due to errors during protein synthesis, either at a translational level or during the assembly of protein complexes. Furthermore, environmental stresses such as temperature, pH, ionic strength and redox environment amplify protein misfolding (Garcia-Mata *et al.* 2002). By exposing hydrophobic domains that are hidden in their native state, misfolded

26

proteins expose themselves to unproductive associations and aggregation (Wetzel 1994). Such misfolding and aggregation is problematic in the cell as it leads to a "crowding effect" in the cytosol, in which large organelles as well as other macromolecules are already present. This so-called "crowding effect" is especially evident in cases where large amounts of heterologous proteins are synthesised thereby exposing similar aggregation-prone domains, increasing the chance of protein aggregation (Garcia-Mata *et al.* 2002).

A wide range of molecular chaperones and folding catalysts are present in the cell and in normal circumstances are efficient in controlling protein folding (Dobson 2003; Cooper and Hausman 2007). Proteins that fail the cell's strict quality control tests initiate an unfolded protein response whereby proteins can be refolded by molecular chaperones and if this chaperone-mediated refolding is unsuccessful misfolded proteins are exposed to the cell's degradative pathways, of which there are two in eukaryotic cells, the ubiquitin-proteasome pathway and the lysosomal pathway (Dobson 2003).

Soluble proteins are targeted to the ubiquitin-proteasome pathway by polyubiquitination, in combination with Hsp70 chaperones, where they are degraded by the 26S proteasome, a multisubunit complex found in the cytosol and nucleus (Dobson 2003; Hurley and Emr 2006). On the other hand, monoubiquitinated transmembrane proteins are transported to the lysosome in one of two ways, either via the autophagic pathway or via the multivesicular pathway (Babst 2005; Hurley and Emr 2006). In the autophagic pathway, autophagosomes (cytoplasmic vesicles containing intracellular components for lysosomal degradation) fuse with lysosomes. Degradation then takes place within the resulting phagolysosomes (Hurley and Emr 2006; Tyedmers *et al.* 2010). Alternatively, multivesicular bodies (MVBs) fuse with lysosomes, releasing their contents into the lysosome for degradation.

There comes a point where the quality control mechanisms of the cell can no longer deal with misfolded proteins, perhaps due to overexpression of the protein or by a decrease in proteasome activity in the case of the ubiquitin-proteasome pathway (Johnston *et al.* 1998). Thereafter, the remaining misfolded and aggregated protein is sequestered to a site that differs per organism, cellular compartment and protein in question, with environmental stress also playing a substantial role (Tyedmers *et al.* 2010).

It has been shown that misfolded proteins not degraded by the degradative pathways of eukaryotic cells accumulate in structures termed aggresomes, first described by Johnston *et al.* (1998) in their investigation of integral membrane protein-1 (PS1) and cystic fibrosis transmembrane conductance regulator (CFTR). These authors suggested that retrograde transport (in a minus-end direction) on microtubules is a cellular mechanism for clearing the cytoplasm of potentially toxic aggregates of

27

misfolded protein (Johnston *et al.* 1998). Furthermore, it was suggested that aggresome formation is a general response to misfolded proteins and that it is not limited to CFTR and PS1. A subsequent study supported this hypothesis but showed that ubiquitination is not a prerequisite of aggresome formation and that it can involve cytosolic, non-ubiquitinated proteins as well as ubiquitinated transmembrane proteins (Garcia-Mata *et al.* 1999). A later study however, showed that aggresomes do not represent a general response to misfolded proteins in mammalian cells indicating that the formation of protein aggregates may be more complex than once believed (Beaudoin *et al.* 2008).

The cell has systems for sorting correctly folded proteins and for handling abnormal or excess proteins, all of which can be exploited by viruses to ensure adequate infections of host cells.

1.8 Aims of this study

As a broader aim, we are interested in the processes underlying the intracellular trafficking of VP7, and its assembly into either cores or crystals. The main aim of this study was to investigate how VP7 self-assembly and particle formation is influenced by top domain modifications. In order to address these events, the objectives were to:

1. Investigate the effects of minor, and major (insertion of eGFP), top domain modifications on the self-assembly and particle formation of AHSV VP7 by using a dual confocal scanning laser and transmission electron microscopy approach.
2. Investigate factors influencing VP7-eGFP aggregation by using sucrose gradient sedimentation analysis.
3. Investigate the fate of misfolded VP7-eGFP fusion proteins by comparing the localisation of fluorescing and non-fluorescing versions of each VP7-eGFP fusion protein under the confocal scanning laser microscope.

28

Chapter 2

2.1 Introduction

In addition to being incorporated into the core, AHSV VP7 trimers have also been shown to self-assemble into distinct hexagonally shaped particles in AHSV-infected cells or when expressed in baculovirus infected cells (Chuma *et al.* 1992; Burroughs *et al.* 1994). This is a characteristic unique to AHSV VP7, which, in contrast to the cognate BTV VP7, is highly hydrophobic and insoluble (Roy *et al.* 1991; Basak *et al.* 1996). Little is known about what determines the self-assembly and particle formation of AHSV VP7. Thus, as a broader research aim we are interested in the processes underlying the assembly of AHSV VP7 into either crystalline-like particles or viral cores. This study however is focussed more specifically on the formation of these characteristic particles, and the effect of various top domain modifications on the assembly thereof.

The AHSV VP7 vector proteins, mutants VP7-144, VP7-177 and VP7-200, containing minor top domain modifications were available for use at the beginning of this study, as were the AHSV VP7-eGFP fusion proteins VP7-144-eGFP, VP7-177-eGFP and VP7-200-eGFP. The latter were representative of AHSV VP7 mutants containing major top domain modifications. As previously detailed, eGFP is particularly useful as the fluorescence thereof is indicative of the correct folding of the protein to which it is fused (Waldo *et al.* 1999). Thus, GFP can be used as a visible marker, thereby providing insights into the function and regulation of the protein to which it is fused (Prasher 1995; Cormack 1998; Zhang *et al.* 2002; Zimmer 2002). Furthermore, primary antibodies directed against GFP can be used to detect proteins to which GFP is fused, even in the absence of fluorescence, thereby allowing different methods of protein detection for such proteins.

The AHSV VP7 vector proteins have previously been characterised with regard to solubility and trimerisation, and have been compared to WT AHSV VP7 under the SEM (Kretzmann 2006; Rutkowska *et al.* 2011; Rutkowska 2012). Data showed that the insertions at sites 144 and 177 increased the solubility of VP7, whereas the insertion at site 200 had little to no effect on solubility. Furthermore, although trimers were formed by all three proteins, VP7-200 was found to be largely monomeric. Studies under the SEM showed that VP7-177 and VP7-200 formed particles that largely resembled those of WT AHSV VP7. However, especially in the case of VP7-200 the particle layering seemed to be affected by the insertion as evidenced by a large incidence of rosette-like particles. In the case of VP7-144 no stable uniform particles were observed at all. Even though particles were not formed, the localisation of VP7-144 to a specific site(s) in the cell was not affected, and in that regard, was shown to behave very much like WT VP7 (Bekker *et al.* 2014). This implies that if transport is unaffected by the top domain modification it is important to study the events taking place at the site of self-assembly.

The VP7-eGFP fusion proteins have not been characterised in as much detail as the vector proteins, but preliminary studies have shown that the insertion of eGFP into the 144, 177 and 200 sites of the AHSV VP7 top domain affects solubility as well as the ability of the protein to form trimers, and the stability thereof (Rutkowska 2012). Like VP7-144, VP7-144-eGFP has recently been shown to localise to a distinct location in the cell but nothing is known about particle formation (Bekker *et al.* 2014). In addition to this data, some fluorescing protein has been found to co-sediment with the particulated or aggregated fraction of all three VP7-eGFP fusion proteins (Mizrachi 2008; Rutkowska 2012). Preliminary data and the subsequent treatment with L-arginine, suggested that in the case of VP7-144-eGFP this represented correctly folded, fluorescing VP7-eGFP trimers that were either loosely aggregated or trapped in the excess of misfolded, non-fluorescing VP7-eGFP protein (Rutkowska 2012). Such loosely reversible aggregated VP7-eGFP fusions were not observed in the case of VP7-177-eGFP and VP7-200-eGFP (Mizrachi 2008; Rutkowska 2012). It is unknown whether or not the tendency of correctly folded, fluorescing VP7-144-eGFP trimers to aggregate is due to the site of the insertion, or whether it could be due to over-expression of the protein later in the infection cycle. Although VP7-177-eGFP has been studied to some extent (Mizrachi 2008), the factors that affect the aggregation of the VP7-eGFP fusion proteins and the kinetics of the process are still unknown.

The aim of this study was to investigate the formation of AHSV VP7 particles and the effect of various top domain modifications thereon. In order to do this the morphology of each of the vector and VP7-eGFP proteins (containing minor and major top domain modifications) was compared to wild type AHSV VP7 using a dual confocal scanning laser and transmission electron microscopic approach. Both forms of microscopy were used here as although confocal microscopy allows three-dimensional reconstructions to be rendered immunofluorescence techniques are limited in that what is observed is directly related to the fluorescent signal(s) of interest (Schnell *et al.* 2012). In contrast, transmission electron microscopy makes it possible to view the ultrastructure of the cell at high resolution (Giepmans *et al.* 2006; Giepmans 2008). In addition to this, the kinetics of VP7-eGFP aggregation was investigated using sucrose gradient sedimentation analyses both with and without the treatment of L-arginine. Lastly, immunofluorescence and confocal microscopy were used to investigate whether or not the localisation of misfolded VP7-eGFP fusion proteins can be detected in relation to correctly folded, fluorescing proteins.

2.2 Materials and Methods

2.2.1 Viruses and cells

Spodoptera frugiperda (Sf9) cells were cultured and maintained in suspension cultures at 27˚C in TC-100 medium (Lonza) supplemented with 10% (v/v) foetal calf serum (FCS, Biochrom), 1% pluronic (Sigma Aldrich) and the appropriate antibiotics (penicillin (100 000 U/l), streptomycin (100 mg/l) and fungizone (50 mg/l), Highveld Biological (Pty) Ltd and Sigma Aldrich). Table 2 lists the recombinant baculoviruses that were available for use in this study. Fresh viral stocks of these baculoviruses were amplified by infecting Sf9 cells (1×10^7 cells) with each baculovirus at a multiplicity of infection (MOI) of 0.1 plaque forming units/ml (pfu/ml) and harvesting the supernatant when total CPE was seen. The baculovirus stocks were then filter sterilised and stored at 4°C.

Table 2 Recombinant baculoviruses used in this study, the proteins they express and the modifications of each

Wild type and Recombinant baculovirus	Expresses	Modification	Reference and/or accredited to
Wild type (WT) Baculovirus	WT Bac specific proteins	-	
Bac-VP7	WT AHSV-9 VP7	-	(Maree *et al.* 1998)
Bac-VP7-144	Vector protein VP7-144	Amino acids PGEFLE inserted downstream of amino acid 144 of AHSV-9 VP7	(Riley 2003)
Bac-VP7-177	Vector protein VP7-177	Amino acids KLSRVD inserted downstream of amino acid 177 of AHSV-9 VP7	(Maree 2000)
Bac-VP7-200	Vector protein VP7-200	Amino acids KLSRVD inserted downstream of amino acid 200 of AHSV-9 VP7	(Maree 2000)
Bac-VP7-144-eGFP	VP7-144-eGFP	eGFP (239aa) inserted into vector VP7-144	Mr T. Seameco
Bac-VP7-177-eGFP	VP7-177-eGFP	eGFP (239aa) inserted into vector VP7-177	(Mizrachi 2008)
Bac-VP7-200-eGFP	VP7-200-eGFP	eGFP (239aa) inserted into vector VP7-200	Dr QC Meyer

2.2.2 Titration of baculovirus stocks

Serial dilutions of each of the baculovirus stocks listed in Table 2 were made in TC-100 medium (Lonza) supplemented with 10% FCS (Biochrom). After the removal of growth medium, 500 µl of each dilution was added in duplicate to separate wells of 6-well plates seeded with Sf9 cells (8.5×10^5 cells/well). Plates were incubated at room temperature (with gentle agitation) for 1 hour after which the all media was removed from each well. Cells were then overlaid with 1.05% low gelling agarose (Agarose, Type VII, Sigma Aldrich) and the plates incubated at 28˚C for 8 days. Cells were then stained with 500 µl/well of 0.1% Thiazolyl Blue Tetrazolium Blue (MTT, Sigma

31

Aldrich) and incubated at 28°C for a further 24 hours, followed by titre determination by counting the visible plaques in each well.

2.2.3 Expression analysis of baculovirus infected Sf9 cells

Sf9 cells (1×10^6 cells/well) were infected with each of the above recombinant baculoviruses at an MOI of 5 before incubation at 27°C for 48 hours. Cells were then harvested via centrifugation at 1500 rpm for 20 mins at 4°C. The cell pellets were rinsed in 1 x phosphate buffered saline (PBS; 137 mM NaCl, 2.7 mM KCl, 4.3 mM $Na_2HPO4.2H_2O$, 1.4 mM KH_2PO_4, pH 7.3) before being resuspended in 1 x PBS and stored at -20°C for analysis by Western blot analysis.

2.2.4 Pre-absorption of primary antibodies

Two of the available primary antibodies were pre-absorbed prior to use in this study (Table 3), with one 75cm^2 flask used per antibody. Flasks were seeded with 1×10^7 Sf9 cells and infected with WT baculovirus at an MOI of 5. The flasks were incubated at 27°C for 48 hours after which cells were collected by centrifugation (3 000 rpm for 5 mins) and resuspended in 0.5-1 ml 1% blocking solution (1% milk powder in 1 x PBS). Cells were lysed by passage through a 22G needle before antibodies (diluted 1:100) were added to the cell lysate. This solution was incubated at room temperature (with gentle agitation) for 3 hours followed by centrifugation at 4 000 rpm for 10 mins. The supernatant was stored at -20°C.

2.2.5 Sucrose density sedimentation of soluble and particulate VP7-eGFP protein

Sf9 cells (1×10^7 cells per 75cm^2 flask) were infected with recombinant baculoviruses, expressing either VP7-144-eGFP or VP7-200-eGFP, at an MOI of 5 and harvested at 24, 30, 38 or 48 hpi. Protein harvesting was done by pelleting the cells at 2 000 rpm for 5 mins. The pellet was resuspended in 1 ml Lysis buffer (0.01 M STE (Tris, EDTA, NaCl), 0.5% Nonidet$^®$-P-40 (NP-40, Boehringer Mannheim)) followed by a 30 min incubation period on ice. The resuspended sample was then homogenised using a 1 ml dounce homogeniser (Wheaton) to obtain a cell lysate containing the protein of interest. At this point the cell lysates were split in two, resulting in two 500 µl samples. One 500 µl sample was left untreated, whilst the other was treated with L-arginine to a final concentration of 1 M L-arginine. Both untreated, and L-arginine treated cell lysates were loaded onto 30-80% (w/v) discontinuous sucrose density gradients and centrifuged in a Beckman Coulter Optima^{TM} L-80 Ultracentifuge (SW55Ti rotor) at 30 000 rpm for 21 hours at 4°C. After removal from the ultracentrifuge, fractions of 500 µl each were collected from the bottom of each tube using a 2112 Redirac fraction collector (LKB Bromma), The pellet was resuspended in 500 µl 1 x PBS. The sucrose gradient fractions and resuspended pellets were stored at -20°C until further use.

32

Table 3 Antibodies used in this study

Antibody	Details
anti-VP7*	Bled from guinea pigs injected with VP7-177-FM Epi, targets VP7 • Used at a dilution of 1/100
anti-VP7-eGFP*	Bled from guinea pigs injected with VP7-177-eGFP, polyclonal targeting VP7 and eGFP • Used at a dilution of 1/100
anti-GFP	Affinity isolated Anti-GFP N-terminal antisera targeting amino acids 3-17 of GFP (Sigma Aldrich). Bled from a rabbit • Used at a dilution of 1/4 000 for Western blot analysis, 1/1 000 for immunofluorescence and 1/500 for immunogold labelling
anti-guinea pig-TRITC	Anti-Guinea Pig IgG (whole molecule) TRITC conjugate, affinity isolated, rabbit, guinea pig IgG (Sigma Aldrich) • Used at a dilution of 1/250 for immunofluorescence
AlexaFluor 633	AlexaFluor 633 goat anti—rabbit IgG, affinity isolated (Invitrogen) • Used at a dilution of 1/250 for immunofluorescence
Anti-Guinea Pig 10 nm Colloidal Gold	Goat anti-Guinea Pig IgG (SPI Supplies) • Used at a dilution of 1/30 for immunogold labelling
Anti-Rabbit 10 nm Colloidal Gold	Goat anti-Rabbit IgG (SPI Supplies) • Used at a dilution of 1/30 for immunogold labelling

*Antibodies that were preabsorbed

2.2.6 VP7 protein analysis via sodium dodecyl sulphate-polyacrylamide gel electrophoresis (SDS-PAGE)

Protein electrophoresis was performed under denaturing conditions with proteins separating based on size differences. The PageRuler (Fermentas) was used as a size marker in all cases. For all experiments 12% separating (0.375 M Tris-HCl pH 8.8, 0.1% SDS) and 5% stacking (5% polyacrylamide, 0.125 M Tris-HCl, pH 6.8, 0.1% SDS,) gels were used, with both being prepared from a 30% acrylamide, 0.8% bisacrylamide stock solution. Polymerisation of each gel was induced chemically by the addition of 0.008% (v/v) N,N,N',N' tetramethylethylene diamine (TEMED) and 0.08% (m/v) ammonium persulphate. Protein samples were resuspended in 2/3 volume 3 x protein solvent buffer (PSB, 0.188 mM Tris-HCl pH=6.8; 6% SDS; 30% glycerol; 15% 2-mercaptoethanol; 0.005% bromophenol blue). Further denaturation of each sample was done by heating to 95°C for 3 mins prior to electrophoresis. The samples were loaded onto a polyacrylamide gel submerged in 1 x Tris-Glycine-SDS (TGS, 25 mM Tris-HCl pH 8.3, 192 mM glycine, 0.1% SDS) buffer and subjected to electrophoresis at 130V for 2.5-3 hours. After electrophoresis the gel was stained with Coomassie Brilliant Blue staining solution (0.125% Coomassie blue, 50% methanol, 10% acetic acid) and destained using 5% ethanol, 5% acetic acid

33

at room temperature overnight. Alternatively, the gel was used for Western blot analysis after the completion of electrophoresis.

2.2.7 Western blot analysis of VP7 protein

After separation via SDS-PAGE, proteins were transferred to a Hybond™ C extra nitrocellulose membrane (Amersham Biosciences) via electroblotting (100V for 1 hour) in the presence of Towbin's transfer buffer (25 mM Tris, 192 mM Glycine, 20% Methanol pH 8.3). After transfer, non-specific binding sites on the membrane were blocked using 1% blocking solution (1% (m/v) milk power in 1 x PBS) for 30 mins-1 hour. The membrane was then incubated overnight at room temperature (with gentle agitation) in the primary antibody (Table 3) diluted appropriately in 1% blocking solution. The membrane was then washed three times in succession with wash buffer (0.05% Tween-20 in 1 x PBS, 5 mins) and incubated for 1 hour with Protein A peroxidase (Calbiochem, diluted 1:10 000). The blots were once again washed three times (5 mins each) with wash buffer followed by rinsing in 1 x PBS (5 mins). In order to detect the bound primary antibody the membrane was transferred to an enzyme-substrate solution consisting of 60 mg 4-chloro-1-napthol in 20 ml ice-cold methanol, mixed with 60 µl hydrogen peroxide in 100 ml 1 x PBS directly before use. The blots were incubated at room temperature until bands became visible, followed by rinsing with dH$_2$O to stop the detection reaction.

2.2.8 Quantification of relative amount of VP7-eGFP protein

The relative amount of VP7-eGFP fusion protein was calculated from immunoblots by scanning the VP7 bands in each pellet and gradient fraction using the EZQuant software package (EZQuant Ltd.).

2.2.9 Fluorescence profiles of soluble and particulate VP7-eGFP protein

The fluorescence (wavelength of 480 nm) emitted each sucrose gradient fraction and pellet was measured by means of a Fluoroskan Ascent FL Fluorometer (Thermo Labsytems), using excitation and emission filters of 485 and 538 nm respectively.

2.2.10 Immunofluorescence and confocal microscopy

Sf9 cells seeded onto sterile coverslips housed in 6- or 24-well plates (1.3×10^6 or 1.9×10^5 cells per well respectively) were infected with recombinant baculoviruses (Table 2) at an MOI of 5 pfu/ml and at 48 hpi were prepared for either direct or indirect immunofluorescence. For direct immunofluorescence cells were rinsed once with 1 x PBS (5 mins), followed by 50% methanol/50% acetone fixation for 2-3 mins. After fixation cells were rinsed with 1 x PBS (5 mins) prior to nuclear staining with 4',6-diamidino-2-phenylindole (DAPI, Roche Applied Science). DAPI (10 µg/µl) was added to each coverslip and incubated at room temperature for 10 mins. Thereafter, cells were rinsed with 1 x PBS before coverslips were mounted onto glass slides using VECTASHIELD

34

Mounting Medium (Vector Laboratories). Cells were infected in the same manner for indirect immunofluorescence and after 48 hours the cells were washed twice with 1 x PBS (5 mins) followed by 50% methanol/50% acetone fixation for 2-3 mins. Thereafter, cells were rinsed in 1 x PBS (5 mins) and blocked using 5% blocking solution (5% milk powder in 1 x PBS) for 30-60 mins. Primary antibody labelling was done overnight at 4°C, after which cells were washed three times (5 mins each) using wash buffer (0.05% Tween-20 in 1xPBS). Secondary labelling using the appropriate antibody (Table 2) was done for 1 hour (at room temperature), after which cells were washed twice with wash buffer (5 mins each) and rinsed twice with 1 x PBS (5 mins each) before nuclear staining with DAPI was performed as above. A last rinse step (1 x PBS for 5 mins) was done before the coverslips were mounted onto glass slides using the same mounting medium as above. All slides were viewed using a Zeiss, LSM 510 Meta confocal microscope. The laser detecting green fluorescence was set at a wavelength of 488 nm, the laser detecting red fluorescence was set at a wavelength of 543 nm (for anti-guinea pig-TRITC) or 633 nm (for AlexaFluor 633) and the laser detecting blue (nuclear staining) was set at a wavelength of 405 nm. Plan-Neofluar 40X/1.3 Oil DIC or 100X/1.3 Oil l objective lenses were used.

2.2.11 Colocalisation analysis

Colocalisation analysis was done using Image J software (Version 1.43m, http://rsb.info.nih.gov/ij). Immunofluorescence images taken using the Zeiss, LSM 510 Meta confocal microscope were analysed as LSM files and as a first step were split into the different channels (red, green and blue). Images representing the blue channel were discarded as they were unnecessary for the colocalisation analyses. The Manders' coefficient was then obtained for the colocalisation of green auto-fluorescence and red primary antibody signal.

2.2.11 High-Pressure Freezing and Freeze Substitution

High-pressure freezing (HPF) was done on Sf9 cells (3.3×10^6 cells per $25 cm^2$ flask) infected with recombinant baculoviruses at an MOI of 5 pfu/ml. After 48 hpi cells were gently dislodged from the flask by scraping. A cell pellet was then obtained by low speed centrifugation at 1 000 rpm for 5 mins. A 0.5 µl sample of the cell pellet was transferred onto a dry Leica membrane specimen carrier coated with L-α-Phosphatidylcholine (10 mg/ml, Sigma Aldrich). Membrane carriers were then placed into a Leica EMPACT2 HPF machine and frozen to -196°C following pressurisation to 2 000 bar within 10 milliseconds (ms) (Studer *et al.* 2001). Following HPF, freeze substitution (FS) was done in a Leica AFS2 FS machine in the presence of a FS mixture of ethanol containing 1% distilled water. During the FS process the temperature was increased from -90°C to 0°C over a period of 72 hours. Thereafter, membrane carriers were removed from the FS machine and washed with 100% ethanol. The cell samples were then transferred from the membrane carriers to Eppendorf tubes (Eppendorf AG) and submerged in 100% ethanol prior to resin embedding.

2.2.12 Resin embedding and transmission electron microscopy

In preparation for immunogold labelling and TEM, resin embedding was done using LR White (SPI Supplies). Half the volume of 100% ethanol present after HPF-FS was removed and replaced with clean LR White resin. This resulted in a 1:1 ratio of 100% ethanol: LR White resin. Before incubation at room temperature for 1 hour, the Eppendorf tube was inverted several times until a homogenous solution was obtained. After 1 hour the entire solution of 100% ethanol and LR White resin was replaced with clean LR White resin and incubated at room temperature for 4 hours to allow further penetration of the resin into the cell sample. Polymerisation of the cell sample in the LR White resin was done at 65°C for 48 hours, after which ultrathin (100 nm) sectioning through the polymerised sample was then done using a Reichert Jung Ultracut E microtome and a diamond knife (DiATOME, US). Staining was done using 1% uranyl acetate for 10 mins and Reynold's lead citrate for 3 mins (Reynolds 1963), followed by visualisation on a JEOL JEM-2100F field emission transmission electron microscope (TEM).

2.2.13 Immunogold labelling for TEM

Immunogold labelling was done using 0.1 M potassium phosphate buffer (1 M K_2HPo_4, 1 M KH_2PO_4, pH 7.2) instead of PBS to minimise the presence of salt crystals. All reagents were sonicated for 30 mins and centrifuged at 10 000 rpm for 2 mins prior to the start of the procedure and were sonicated further for 5 mins and the centrifuged at 10 000 rpm for 2 mins directly before use. Blocking of non-specific binding sites was done for 1.5-2 hours using blocking buffer composed of 0.1 M potassium phosphate buffer, 5 % FCS, 0.05 % Tween-20. Primary antibody labelling was then done for 1.5-2 hours with each antibody diluted appropriately in blocking buffer (Table 3). Grids were washed twice with blocking buffer (2 mins each) and thereafter were rinsed twice with potassium phosphate buffer (2 mins each). Secondary antibody labelling (Table 3) was done for 1 hour followed by another wash and rinse step. Once dry, grids were stored for future TEM viewing.

36

2.3 Results

The aim of this study was to investigate how AHSV VP7 self-assembly and particle formation is influenced by top domain modifications. This was divided into two main components forming the two major headings of this section. The first component dealt with the effect of minor top domain modifications on the self-assembly and particle formation of AHSV VP7 (2.3.2). The second was concerned with investigating the effect of a large insertion in the top domain on the self-assembly and particle formation of AHSV VP7 (2.3.3). Before we addressed these components we first determined whether or not the available baculovirus stocks were expressing the proteins necessary for this study and, in addition to this, we established controls for both confocal and transmission electron microscopy.

2.3.1   Verification of baculovirus stock expression and establishment of immunofluorescence and TEM controls

In order to confirm baculovirus stock expression of WT AHSV VP7, the vector proteins VP7-144, VP7-177 and VP7-200, as well as the VP7-eGFP fusion proteins VP7-144-eGFP, VP7-177-eGFP and VP7-200-eGFP, Western blot analyses were performed on protein samples harvested from recombinant baculovirus infected Sf9 cells.

Following Western blot analysis using a VP7-specific primary antibody, a VP7 specific protein band of approximately 38 kDa was visible in lanes 2-5 of the immunoblot (Fig. 12A). This was the expected size of the WT and vector proteins, and was absent in lanes 6 and 7, thereby confirming baculovirus expression of WT VP7 and the VP7 vector proteins. The immunoblot in Figure 12B showed a protein band of approximately 63 kDa in lanes 2-4 following detection with the anti-GFP primary antibody. This was the expected size of the VP7-eGFP proteins and was absent in lanes 5 and 6 of the immunoblots, thereby confirming baculovirus expression of the VP7-eGFP proteins.

Once recombinant baculovirus expression of the necessary proteins had been confirmed, it was necessary to establish controls needed for this study.

37
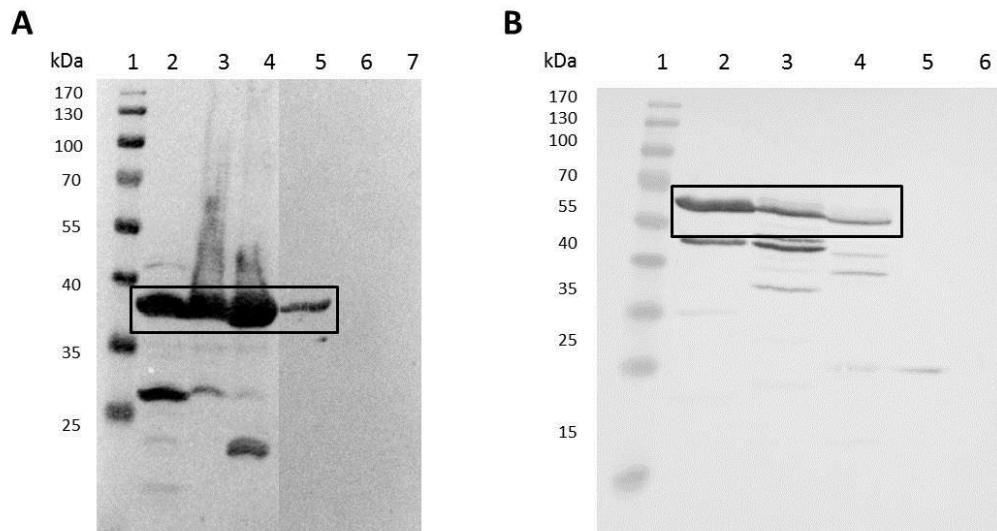
Fig. 12 Western blot analysis of baculovirus expressed VP7 proteins. For A and B: PageRuler (Fermentas) (Lane 1). Sf9 cells were infected with recombinant baculoviruses expressing VP7-144 (2), VP7-177 (3) or VP7-200 (4) or WT VP7 (5). A WT Bac control and a mock infected sample are seen in lanes 6 and 7 respectively. The boxes indicate WT VP7 and the VP7-144, VP7-177 and VP7-200 vector proteins (~38 kDa). For B: Sf9 cells were infected with recombinant baculoviruses expressing VP7-144-eGFP (2), VP7-177-eGFP (3) or VP7-200-eGFP (4). A WT Bac control and a mock infected sample are seen in lanes 5 and 6 respectively. The boxes indicate the VP7-144-eGFP, VP7-177-eGFP and VP7-200-eGFP VP7-eGFP fusion proteins.

It was important to note what structures in the cell were baculovirus specific so that structures related to VP7 expression could be easily identified. In order to investigate this, Sf9 cells were infected with WT Bac and viewed under the TEM (Fig. 13). These round cells have large nuclei, surrounded by a relatively small area of cytoplasm (A). The tubular structures seen in the nucleus of the Sf9 cell in Figure 13B are baculovirus specific structures and baculoviruses themselves are shown in Figures 13C and 13D. In Figure 13E, the baculovirus protein, p10, is shown in association with a fibrillar structure (Lee *et al.* 1996).
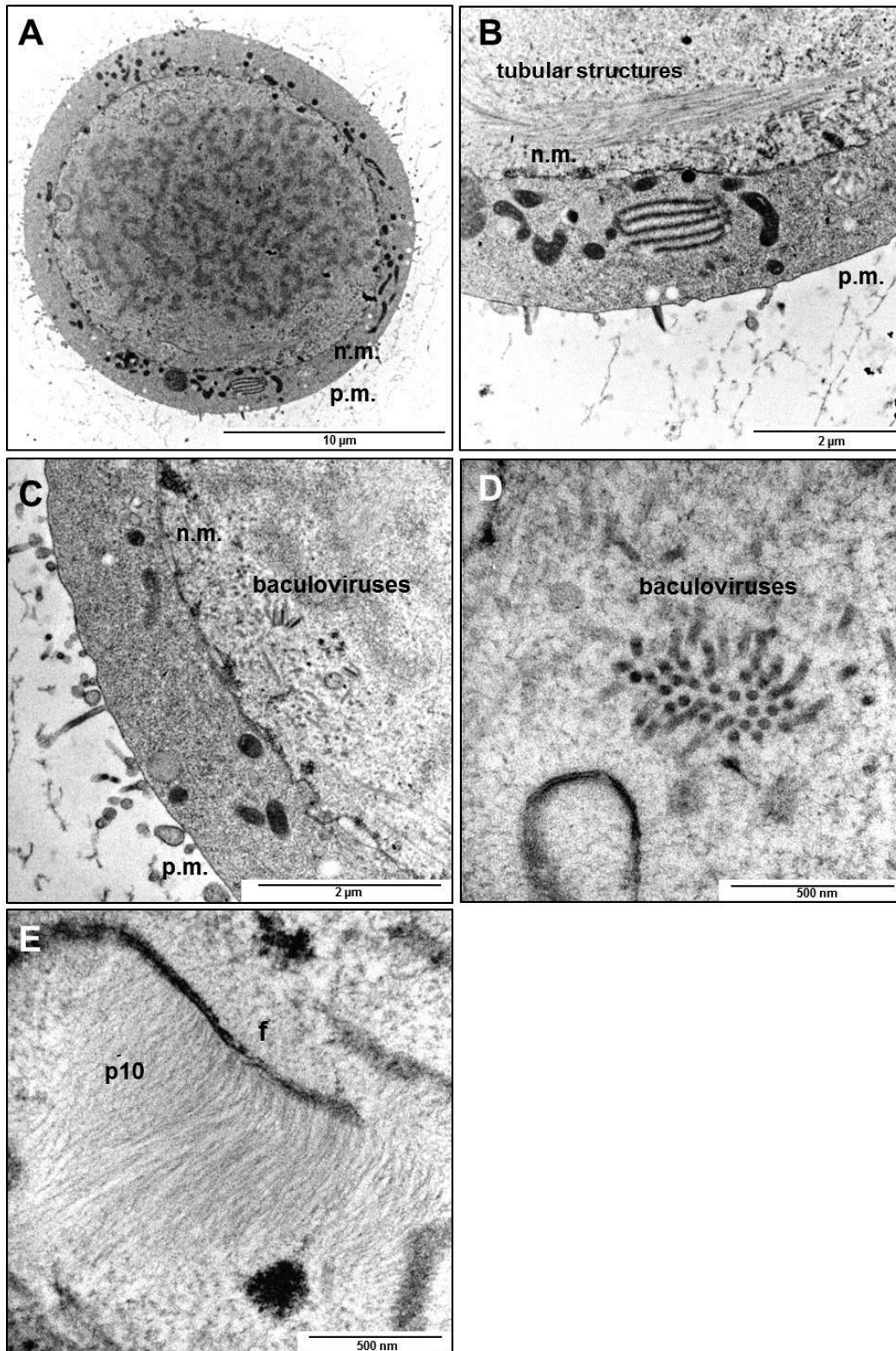
Fig. 13 TEM micrographs of Sf9 insect cells infected with WT Bac (48 hpi). B and C are enlargements of region of the cell in A. Baculovirus specific tubular structures are shown in B. Baculoviruses are seen shown in C and D. E shows p10 associating with a fibrillar structure. n.m. = nuclear membrane. p.m. = plasma membrane. f = fibrillar structure. Scale bars represent 10 µm (A), 2 µm (B, C), 500 nm (D, E).

To establish the extent of background labelling of cellular or baculovirus proteins by the available primary antibodies (Table 3, Materials and Methods), mock infected and WT Bac infected cells

39

were labelled with each primary antibody and tested for either confocal or TEM imaging, or both. Little to no background was observed in mock infected Sf9 cells when immunolabelling and confocal microscopy were performed with preabsorbed anti-VP7 primary and TRITC-conjugated secondary antibodies (Figs. 14A and B). This was similar for mock infected Sf9 cells immunogold labelled with anti-VP7 primary and gold-conjugated secondary antibodies, where the presence of 10 nm gold particles indicated positive labelling (Figs. 14C and D). The level of background seen in the WT Bac infected cells varied from experiment to experiment but fell between the range seen in Figure 14, with most cells showing the background level observed in Figure 14E. Anything resembling the background seen in Figure 14F was regarded as background baculovirus labelling. Quite a high level of background labelling was observed in immunogold labelled WT-Bac infected Sf9 cells (Fig. 14G and H), with most of this labelling located at the sites of baculovirus production (Fig. 14G and H) with much less general cytoplasmic labelling. The background immunogold labelling illustrated here was not a problem in other experiments, as the labelling of VP7 was seen to be very specific in cells expressing WT VP7 or the mutant VP7 proteins.

Little to no background was seen in mock infected Sf9 cells when immunolabelling and confocal microscopy were performed with anti-VP7-eGFP and anti-GFP antibodies (Fig. 14I-L). Quite some background was observed in WT Bac infected cells when immunolabelled with anti-VP7-eGFP (Fig. 14K) and little to no background was observed in WT Bac infected cells immunolabelled with anti-GFP (Fig. 14L).

After confirming protein expression and establishing the necessary controls, we were able to progress to Section 2.3.2 of this study.
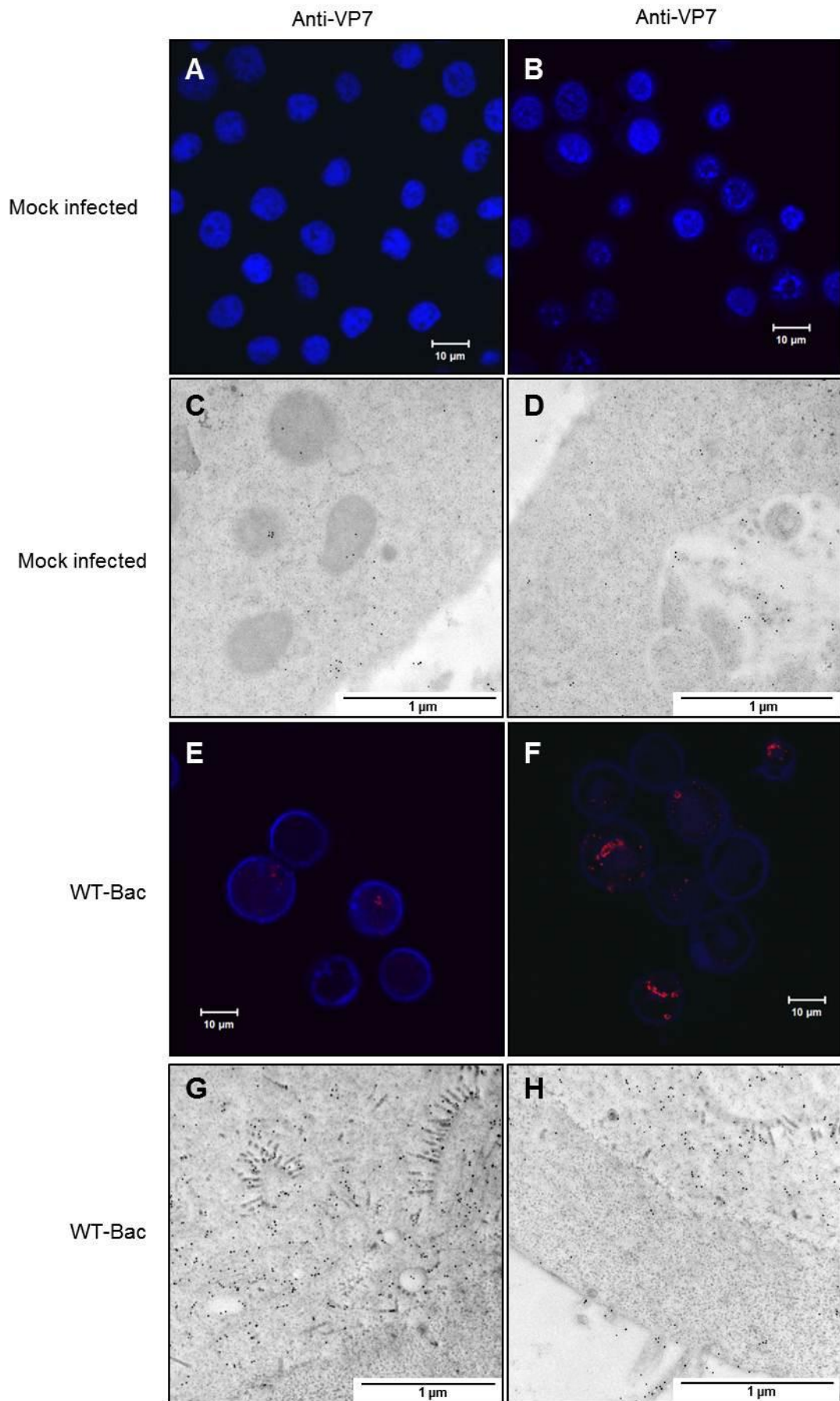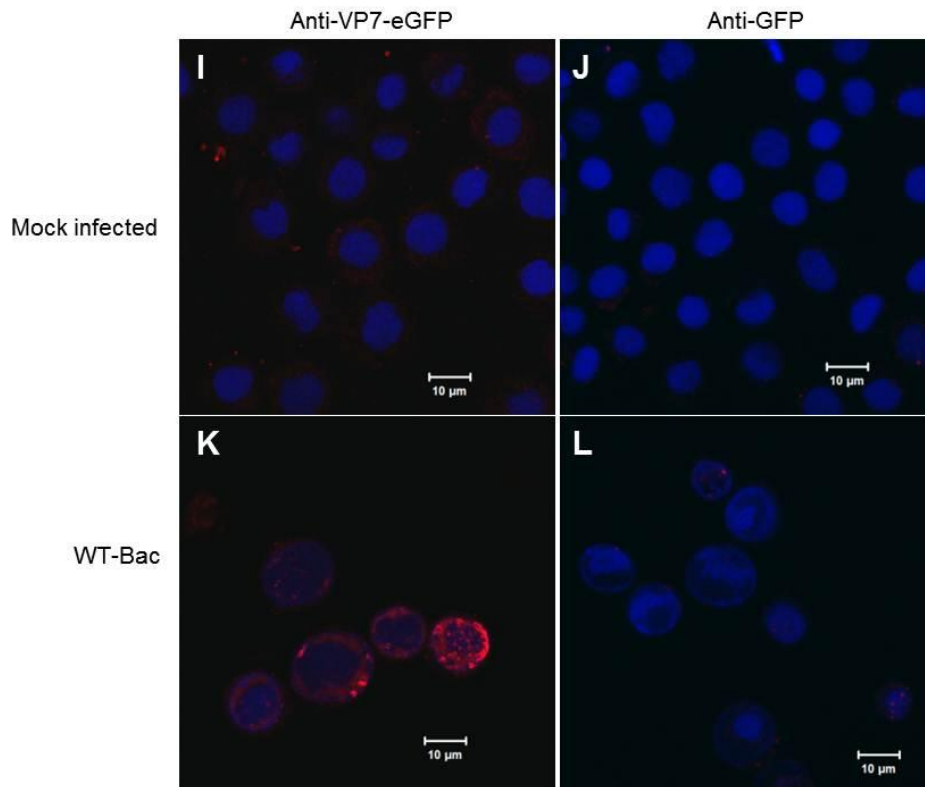
Anti-VP7   Anti-VP7

Fig. 14 Immunofluorescence and TEM micrographs of mock infected and WT Bac infected Sf9 insect cells at 48 hpi. For immunofluorescence, labelling was done with preabsorbed anti-VP7 (A, B, E, F), anti-VP7-eGFP (I, K) primary and TRITC-conjugated secondary (red) antibodies. Immunolabelling was done with anti-GFP primary and AlexaFluor secondary antibodies in J and L. For immunofluorescence, nuclear staining was done with DAPI (blue). For TEM, labelling was done with anti-VP7 primary and gold-conjugated secondary antibodies (C, D, G, H). Scale bars represent 10 µm for immunofluorescence and 1 µm for TEM micrographs.

2.3.2 Effect of minor top domain modifications on AHSV VP7 self-assembly and particle formation

In order to investigate the effect of minor top domain modifications on the self-assembly and particle formation of AHSV VP7 a dual microscopic approach of applying confocal microscopy in conjunction with TEM was used. Sf9 cells were infected with recombinant baculoviruses expressing WT VP7 or various top domain modified VP7 proteins, namely the vector proteins VP7-144, VP7-177 and VP7-200. At 48 hpi, Sf9 cell samples were prepared for immunofluorescence, or preserved by high pressure freezing and freeze-substitution (HFP-FS) for TEM. Anti-VP7 was used for both immunofluorescence and immunogold labelling, with TRITC- or gold-conjugated secondary antibodies respectively. Uninfected (mock infected) Sf9 cells as well as WT-Bac infected Sf9 cells were included as negative controls for each experiment that was performed.

WT VP7

This study was started with an investigation into WT AHSV VP7 as little is known about the self-assembly process of this protein. Also, to determine what effect, if any, the modifications to the top

42

domain had on AHSV VP7 self-assembly and particle formation it was necessary to compare the vector proteins to WT AHSV VP7.

Immunofluorescence and confocal microscopy of WT VP7 showed one or more crystalline-like particle in the cell (Fig. 15). Localised mainly in the cytoplasm, but also occasionally in the nucleus, these particles were observed as flat, rod-like (Fig. 15B), or hexagonal (Fig. 15C) structures. Labelling was observed on the outer edge of the rods, whereas hexagonal particles were observed as solid structures (Fig. 15).
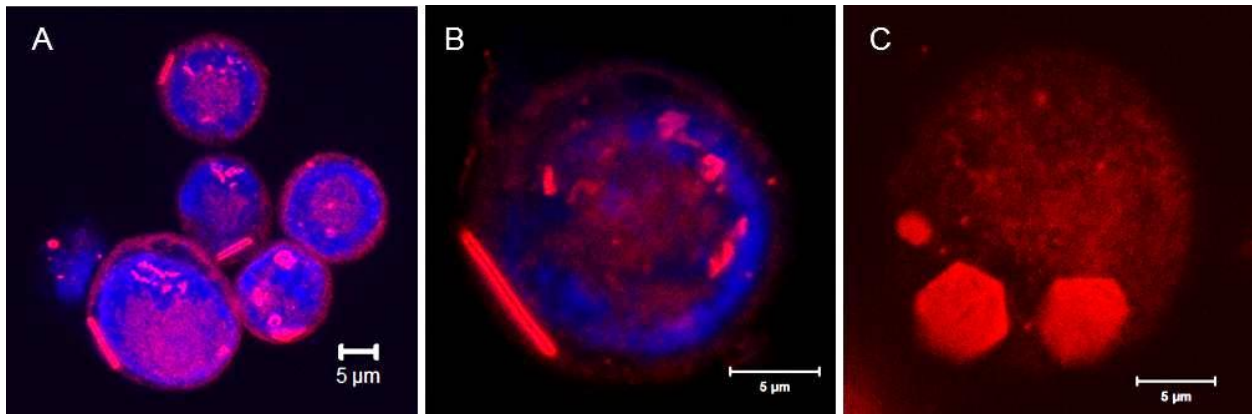
Fig. 15 Immunofluorescence images of Sf9 cells infected with Bac-VP7 at 48 hpi. A larger field of cells is seen in A. Wild-type VP7 is visualised as rod-like (B) or hexagonal (C) crystalline-like particles depending on the focal plane and orientation of the cell. Immunolabelling was done with anti-VP7 (primary antibody) and anti-guinea pig-TRITC (red secondary antibody). Nuclear staining was done with DAPI (blue). Scale bars represent 5 μm.

To further investigate the self-assembly and particle formation of AHSV VP7, Z-stack analysis was used. This technology is one of the advantages of confocal microscopy, and results in three-dimensional (3D) representations of an entire cell. Using the field of cells in Figure 16A as an example, Z-stack analysis is performed by manually defining the upper and lower margins of the field and instructing the microscope to take images at defined intervals through the field, between the two margins. An image gallery of the resulting images is then compiled (Fig. 16B) and these images are stacked by the software to render a 3D reconstruction.

Once the 3D reconstruction has been rendered, one is able to take snapshots as it is rotated around a specified axis. Here, snapshots were taken as the 3D reconstruction rotated around the Y-axis (Fig. 17). Using the VP7 particle in cell 3 as an example, WT VP7 particles can be viewed as rod-like or hexagonal crystalline-like particles depending on the focal plane and orientation of the cell. In Panel 1 this particle was viewed as a rod, however, as the reconstruction was rotated around the Y-axis in a clockwise manner the rod looked more and more hexagonal in shape, until a true hexagonal particle was viewed at a 90˚ angle to the original rod (Panel 5, Fig. 17). The particle

43

appeared rod-like once again after another 90° rotation around the Y-axis (Panel 9, Fig. 17). Furthermore, this 3D reconstruction indicated that AHSV VP7 self-assembled to multiple sites in the cell even though a single plane through a field (such as that in Fig. 16A) suggested that only one particle was present per cell. Often, as many as three self-assembly sites were observed in a single cell (Cell 1, Panels 6-8, Fig. 17).
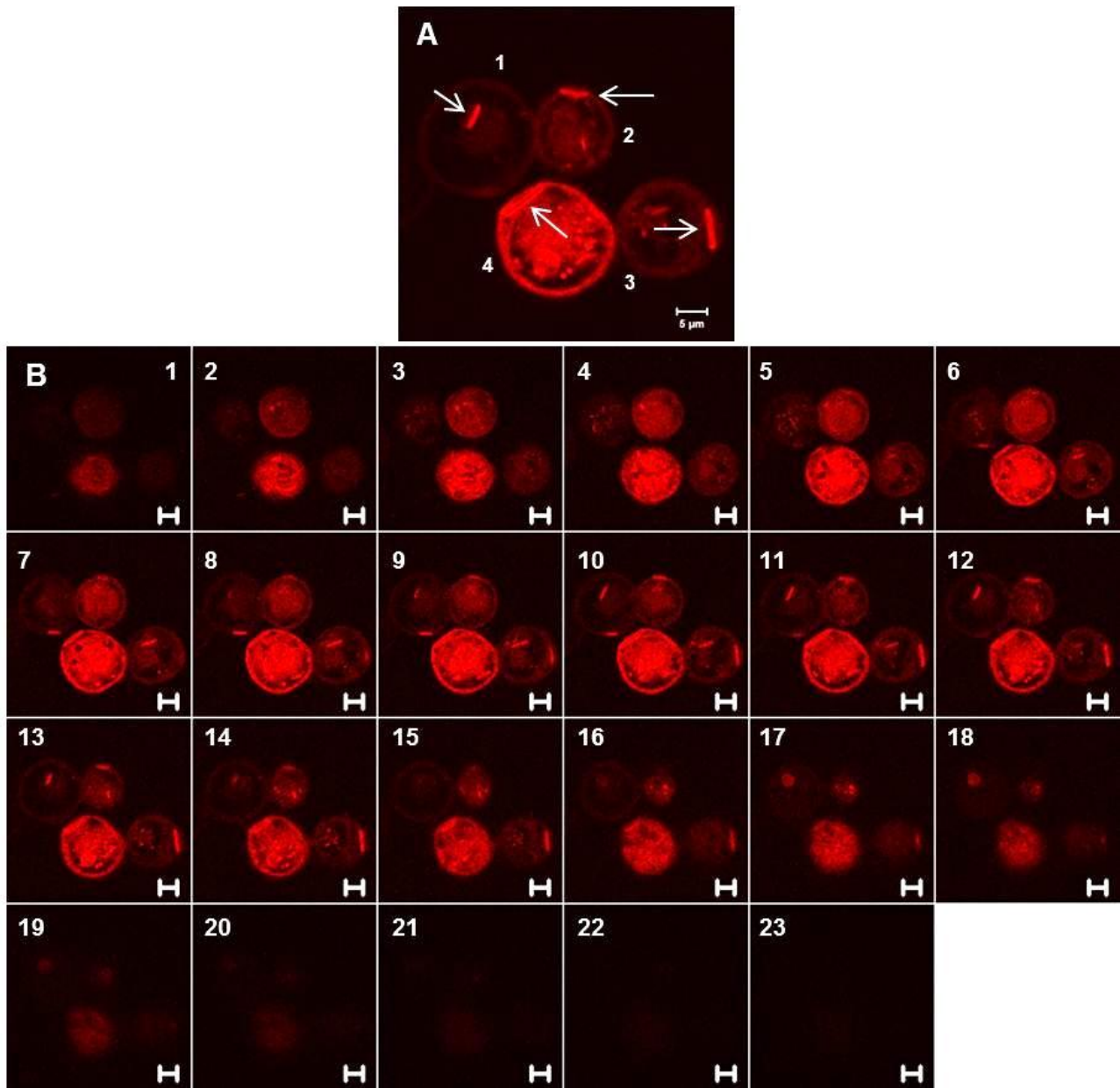
Fig. 16 Z-stack analysis of a field of Sf9 cells infected with Bac-VP7 (48 hpi, A). Arrows indicate rod-like AHSV VP7 particles. Immunolabelling was done with anti-VP7 (primary antibody) and anti-guinea pig-TRITC (red secondary antibody). Cells are labelled 1 through 4. The Z-stack gallery of 23 images taken at 0.8 μm intervals through the field is shown in B. Scale bars represent 5 μm.

44
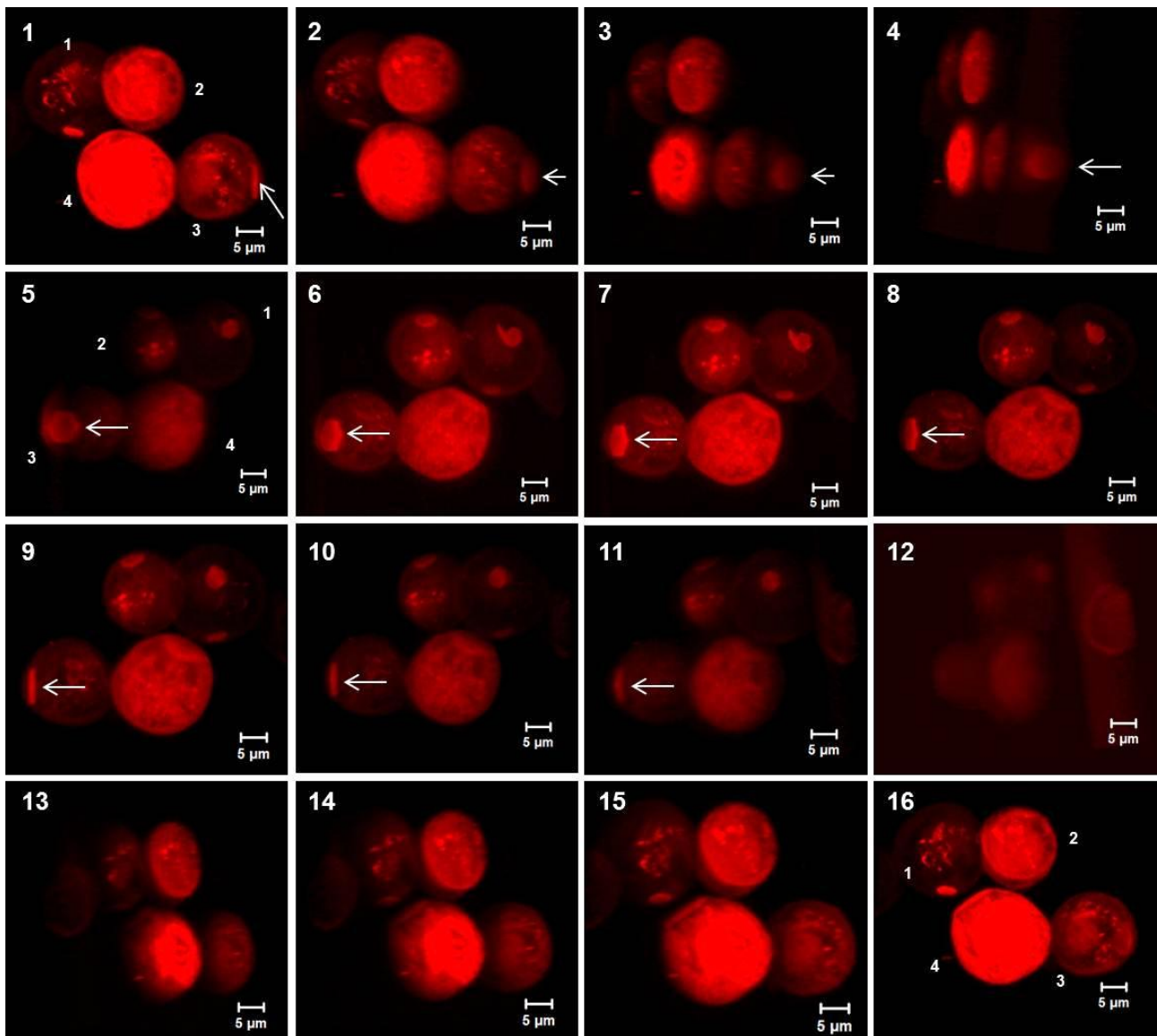
Fig. 17 Snapshots of a three-dimensional reconstruction of the Bac-VP7 infected Sf9 cells (48 hpi) in Figure 7. The reconstruction was rotated around the Y-axis in a clockwise manner, with 90° rotation observed in Panel 5, 180° in Panel 9, 270° between Panels 12 and 13, and 360° in Panel 16. Cells are labelled 1 through 4. The particle in cell 3 appeared rod-like at 0° (Panel 1) and appeared more hexagonal in nature as the reconstruction was rotated around the Y-axis (Panels 1-8). When viewed at 180°, the particle was once again viewed as a rod (Panel 9). Cell 1 illustrated that there are often multiple VP7 self-assembly sites per cell. Scale bars represent 5 μm.

In order to investigate the structures formed by WT VP7 on an ultrastructural level, Bac-VP7 infected cells were cryofixed and embedded prior to ultrathin sectioning and visualisation by TEM. Rod-like crystalline-like particles were observed in the cell and were found to be located mainly in the cytoplasm (Fig. 18). No hexagonal crystals were observed under the TEM, which is not surprising as TEM is done on sections through a cell.

In order to confirm that these rigid structures were indeed WT VP7, immunogold labelling using anti-VP7 primary and gold-conjugated secondary antibodies was performed. Very specific positive

45

labelling, as indicated by the presence of 10 nm gold particles, was observed (Fig. 19), thereby confirming that the rod-like particles were indeed WT VP7.
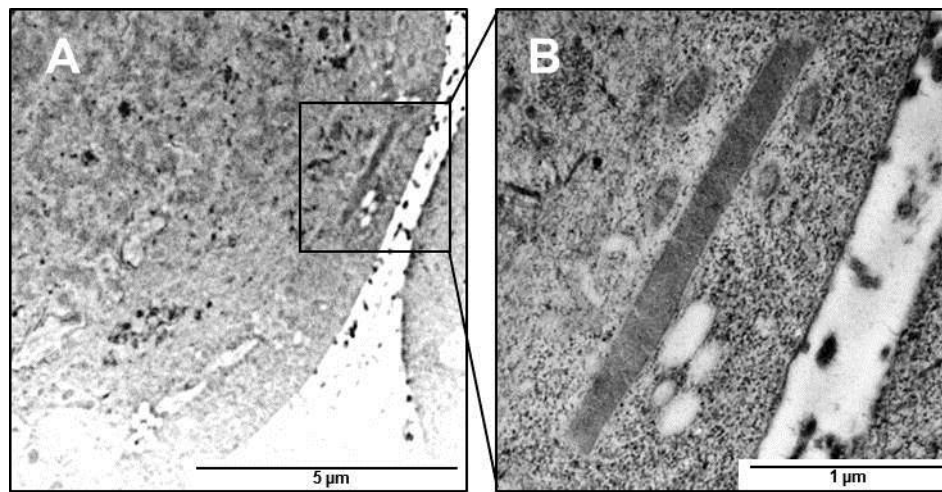
Fig. 18 TEM micrographs of Bac-VP7 infected Sf9 cells (48 hpi). A - VP7 crystalline-like particle is indicated in the cytoplasm of the cell, with an enlargement of the field shown in B. Scale bars represent 5 µm (A) and 1 µm (B).
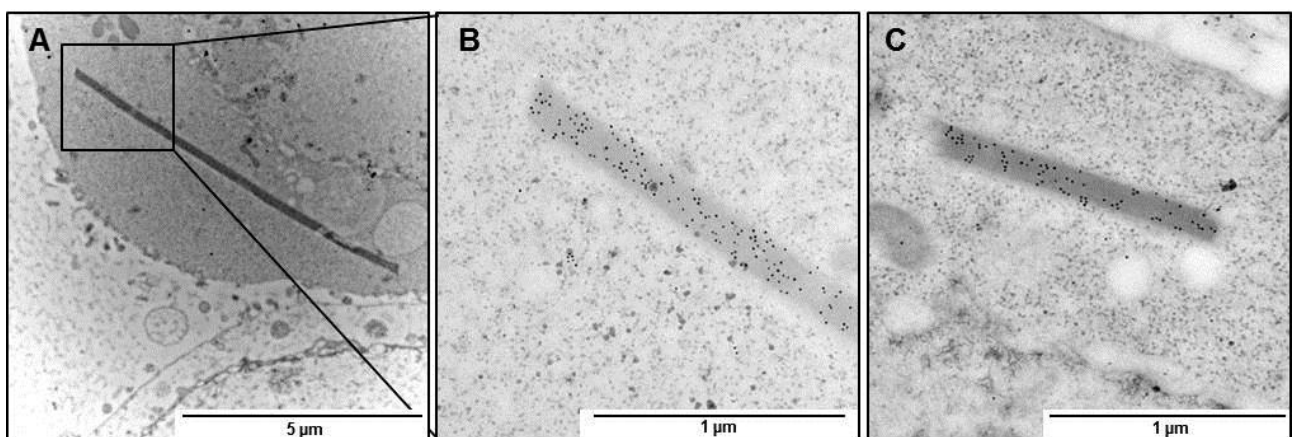
Fig. 19   TEM micrographs of WT VP7 in Sf9 cells immunogold labelled with anti-VP7 primary and gold-conjugated secondary antibodies, with B an enlargement of the field in A. In all cases, WT VP7 is visualised as rod-like crystalline-like particles. Scale bars represent 5 µm (A) and 1 µm (B, C).

The above data for WT AHSV VP7 was then compared to the vector proteins containing minor top domain modifications.

VP7-144

Like WT VP7, VP7-144 (amino acids PGEFLE inserted downstream of amino acid 144 of AHSV-9 VP7, Riley, 2003) assembled to one, or multiple site(s) in the cell (Fig. 20). However, this protein did not form the well-defined particles characteristic of WT VP7. Instead, long and tapered structures, hereafter referred to as spindle-like structures, were observed, and associated to form

46

larger spindle aggregates (Fig. 20A, B). These larger spindle aggregates appearing somewhat star-shaped (Fig. 20B), with anti-VP7 labelling having occurred on the outer edge of the spindle-like structures, leading to the halo-like effect observed in Figure 20.

Z-stack analysis showed that the star-shaped aggregates were formed by spindle-like structures layering one on top of the other (Fig. 21). Panels 2-17 of Figure 21 illustrate the gradual layering of VP7-144 spindles from the bottom (Panel 17) to the top of the aggregate (Panel 2), eventually resulting in the structure observed in Figure 21A. A 3D reconstruction of this cell was made (not shown) and the rotation thereof around the Y-axis showed that the star-shaped aggregate was visible at 0˚ and then again at 180˚, from the opposite side of the cell, thereby indicating that this was a large structure occupying a significant portion of the cell.
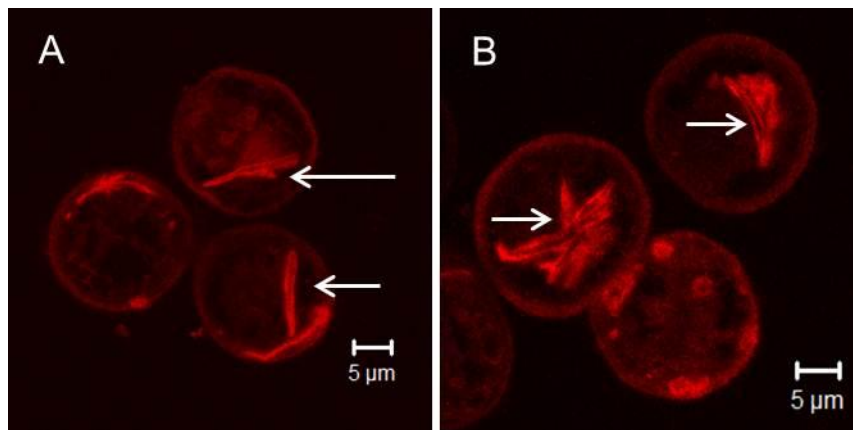
Fig. 20 Immunofluorescence images of Sf9 cells infected with Bac-VP7-144 at 48 hpi. VP7-144 self-assembles into spindle-like structures (A) that associate to form the larger star-like structures in B. Immunolabelling was done with anti-VP7 (primary antibody) and anti-guinea pig-TRITC (red secondary antibody). Scale bars represent 5 µm.

47
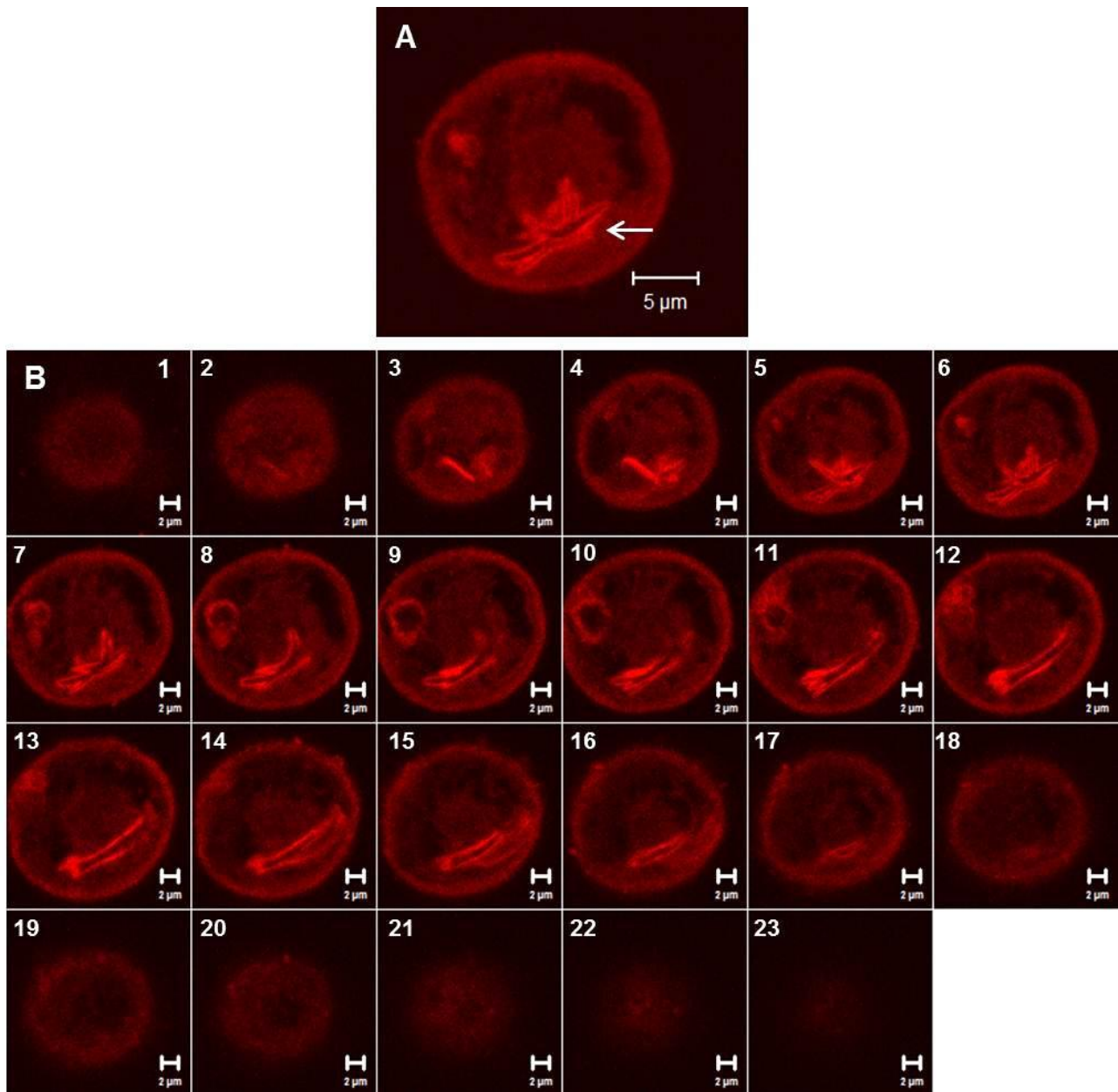
Fig. 21 Z-stack analysis of a Sf9 cell infected with Bac-VP7-144 (48 hpi). The cell of interest is shown in A. The Z-stack gallery of 24 images taken at 1 µm intervals through the cell is shown in B. VP7-144 spindles layer one on top of the other to form the larger spindle aggregate shown in A. Immunolabelling was done with anti-VP7 (primary antibody) and anti-guinea pig-TRITC (red secondary antibody). Scale bars represent 5 µm (A) and 2 µm (B).

The spindle-like structures observed under the confocal microscope were visualised as long, fibrous structures under the TEM (Fig. 22A, B). In addition to these structures, small, loosely associated structures were also observed in infected cells (Fig. 22C), with both often being observed in the same cell (Fig. 22D). The presence of both structures in a specific cell led to the postulation that the smaller loosely associated structures were cross sections through spindle aggregates.

48

Enlargements of both structures showed that these structures lacked the rigidity of the WT particles and tapered in at either end (Fig. 22F, G). The structure in Figure 20I further illustrates that although the smaller structures associated with one another, they did not form larger rigid structures with well-defined shapes.
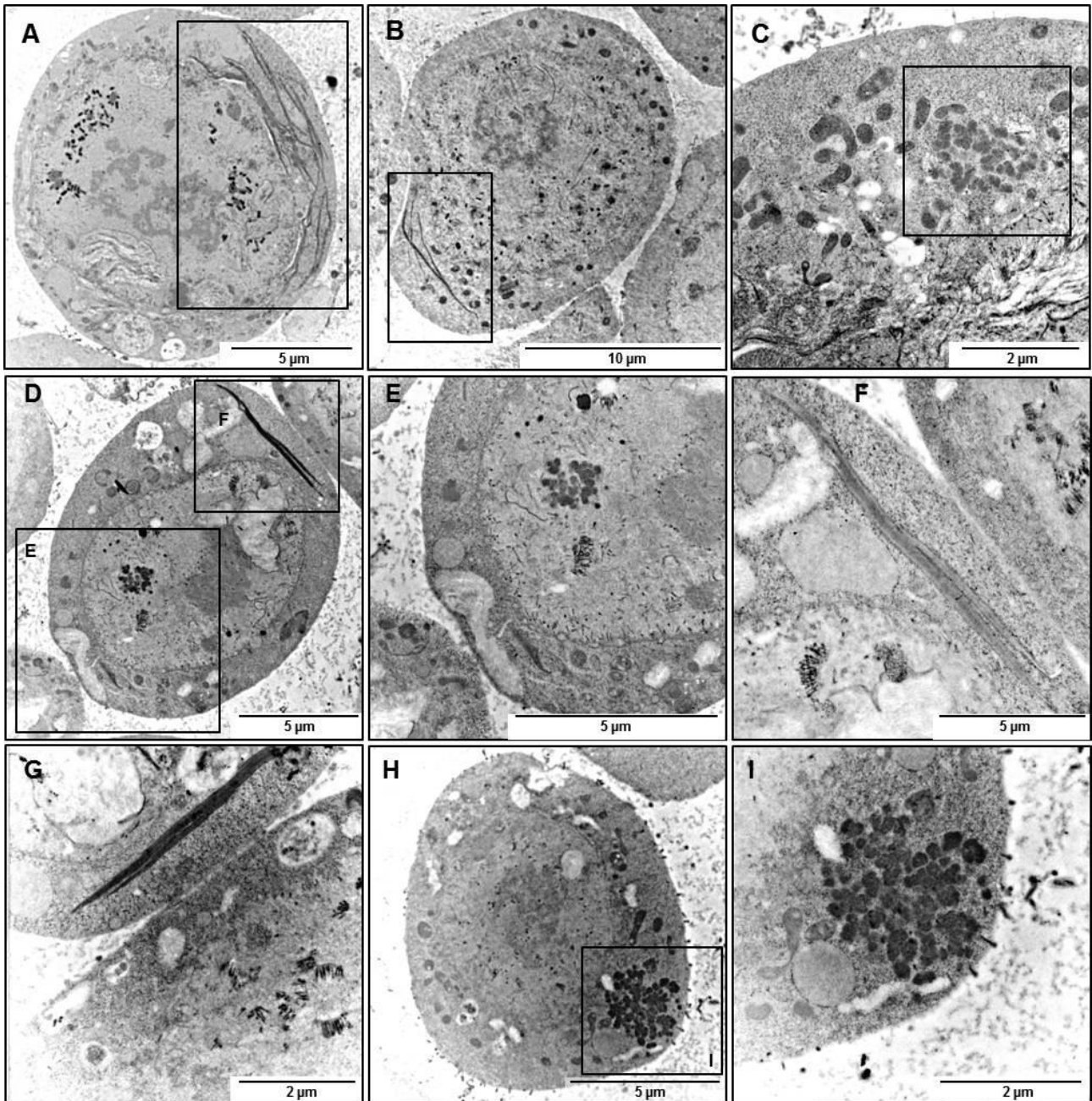
Fig. 22 TEM micrographs of Bac-VP7-144 infected Sf9 cells (48 hpi). A, B – cytoplasmic spindle-like structures were visualised in multiple cells, as were foci-like structures composed of small, loosely associated protein aggregates (C). Both structures were often observed in the same cell (D), with enlargements shown in E and F. Enlargements showed that the spindle-like structures tapered in at both ends (F, G). Foci-like structures always appeared to be composed of loosely associated protein aggregates indicating that these structures were most likely cross sections through the spindle-like structures (H, I). Scale bars represent 5 µm (A, D-F), 10 µm (B) and 2 µm (C, G, I).

49

In order to confirm whether or not the observed structures were VP7 specific proteins, immunogold labelling with anti-VP7 primary and gold-conjugated secondary antibodies was performed. Very specific labelling was obtained thereby confirming that both structures were indeed VP7 related (Fig. 23).
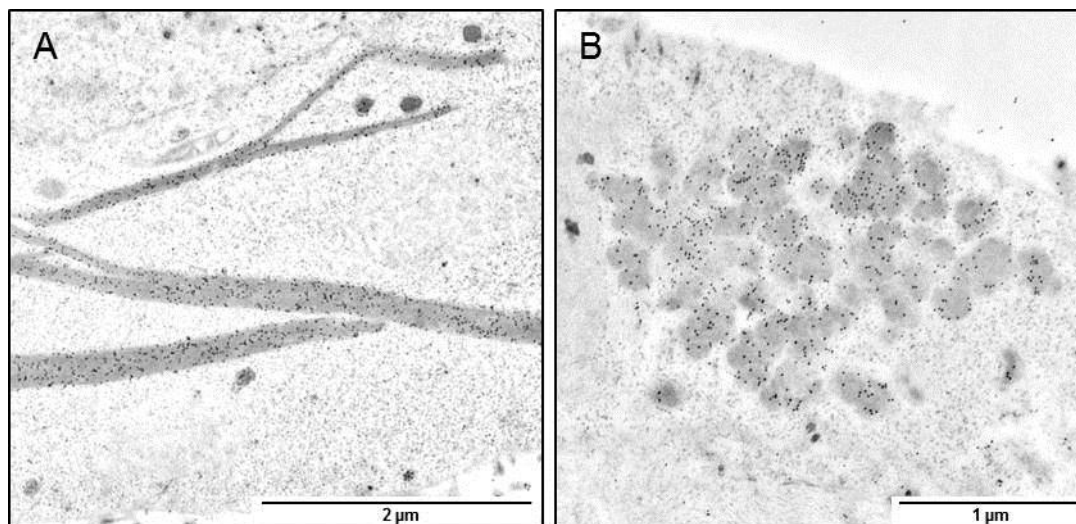
Fig. 23 TEM micrographs of VP7-144 immunogold labelled with anti-VP7 primary and gold-conjugated secondary antibodies. Spindle-like structures are shown in A and a cross section through a spindle aggregate is shown in B. Scale bars represent 2 μm (A) and 1 μm (B).

Next, we investigated VP7-177, the vector protein with intermediate solubility.

VP7-177

The next vector protein to be investigated was VP7-177 which was modified by the insertion of the amino acids KLSRVD downstream of amino acid 177 of AHSV-9 VP7 (Maree, 2000). The structures formed by VP7-177 appeared rosette-like under the confocal microscope (Fig. 24) and were similar in shape to the spindle aggregates formed by VP7-144 (Fig. 20). As with VP7-144, these rosette-like structures appeared to be composed of VP7 sheets that layered on top of one another to form a larger structure. These structures appeared somewhat hollow, with antibody labelling having occurred around the edges of each sheet leading to a halo-like effect (Fig. 24).

The layering of VP7-177 is illustrated by the subset of images in Figure 25. A few VP7-177 particles were present in Panel 7 (Fig. 25B), however, more particles were observed at this site with gradual progression through the cell. This pattern continued throughout, from one end of the rosette to the other, showing a larger structure composed of smaller VP7-177 sheets layered one on top of the other.
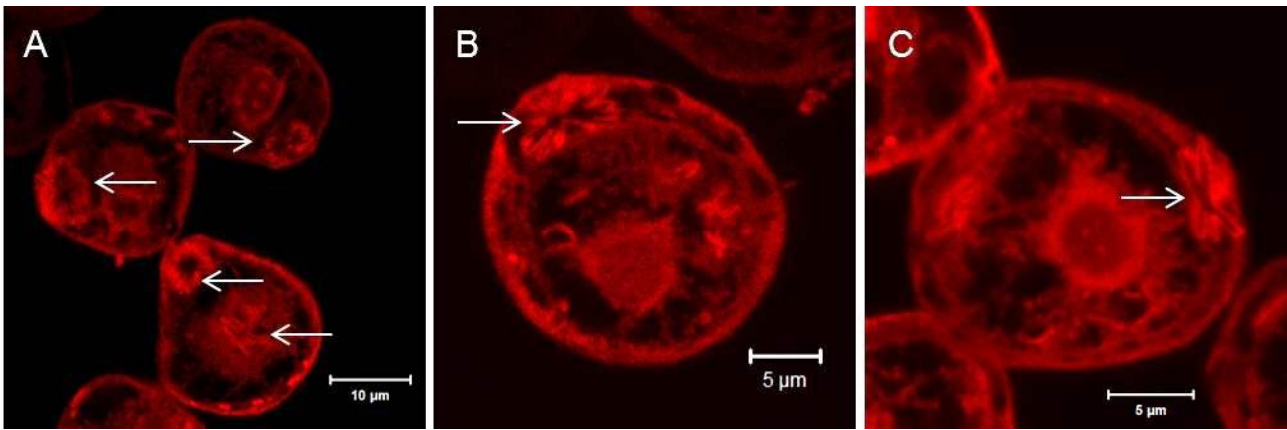
Fig. 24 Immunofluorescence images of Sf9 cells infected with Bac-VP7-177 at 48 hpi. VP7-177 forms rosette-like structures, located mainly in the cytoplasm, as indicated by arrows in A-C. Immunolabelling was done using anti-VP7 (primary antibody) and anti-guinea pig-TRITC (red secondary antibody). Scale bars represent 10 μm (A) and 5 μm (B, C),

TEM showed that on an ultrastructural level VP7-177 assembled into rigid particles resembling those of WT VP7, however, the stable layering of the VP7 sheets was affected, leading to the formation of rosette-like structures (Fig. 26A-D). At times, single rods of varying length were also observed in the cell (Fig. 26E, F). Very specific positive immunogold labelling using anti-VP7 primary and gold-conjugated secondary antibodies for these structures confirmed that they were indeed VP7-177 (Fig. 26B, D, F).

51
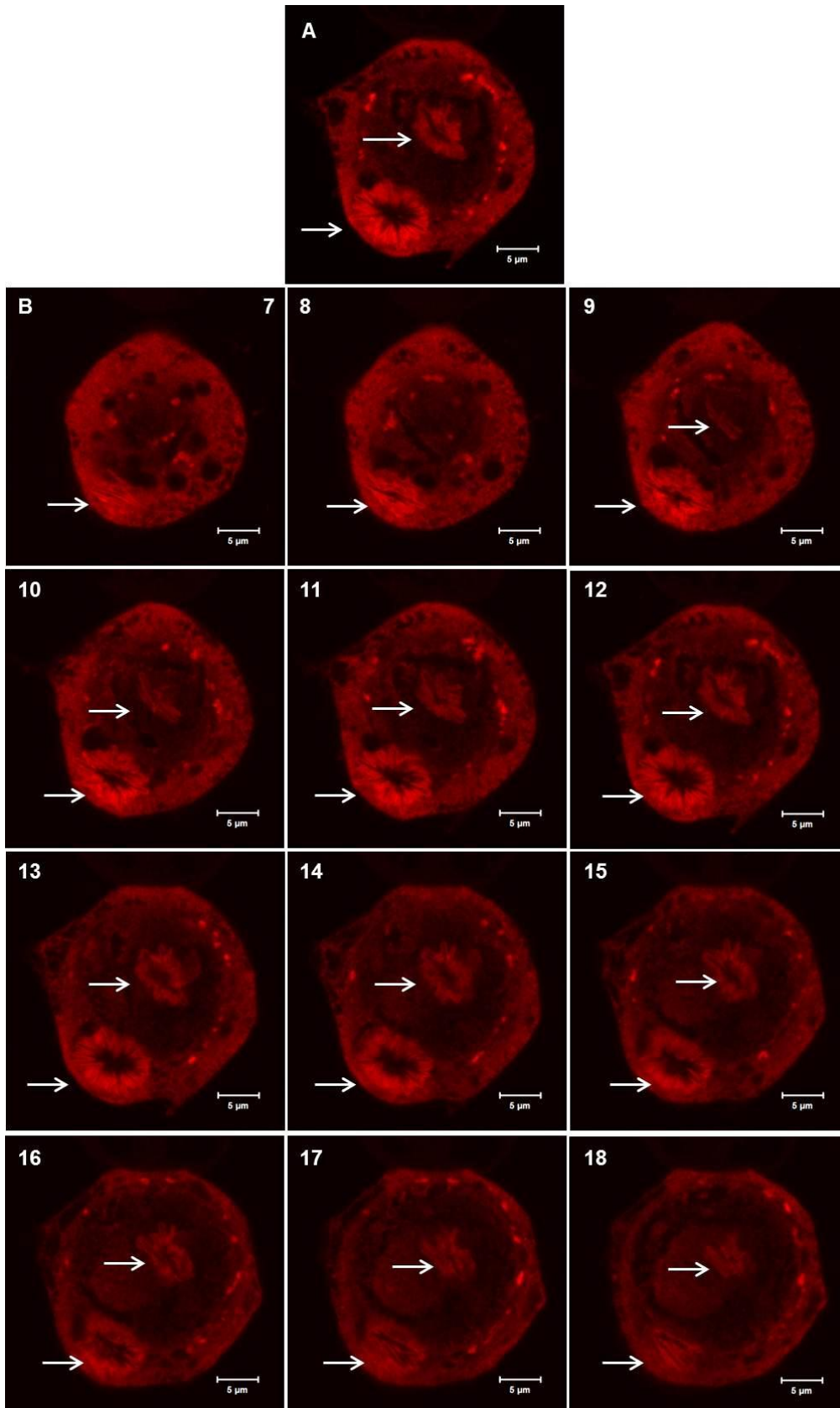
Fig. 25 Z-stack analysis of a Bac-VP7-177 infected Sf9 cell (48 hpi). The cell of interest is shown in A. A subset of the Z-stack gallery of images taken at 0.75 µm intervals through the cell is shown in panels 7-18 (B). Immunolabelling was done with anti-VP7 (primary antibody) and anti-guinea pig-TRITC (red secondary antibody). Scale bars represent 5 µm.
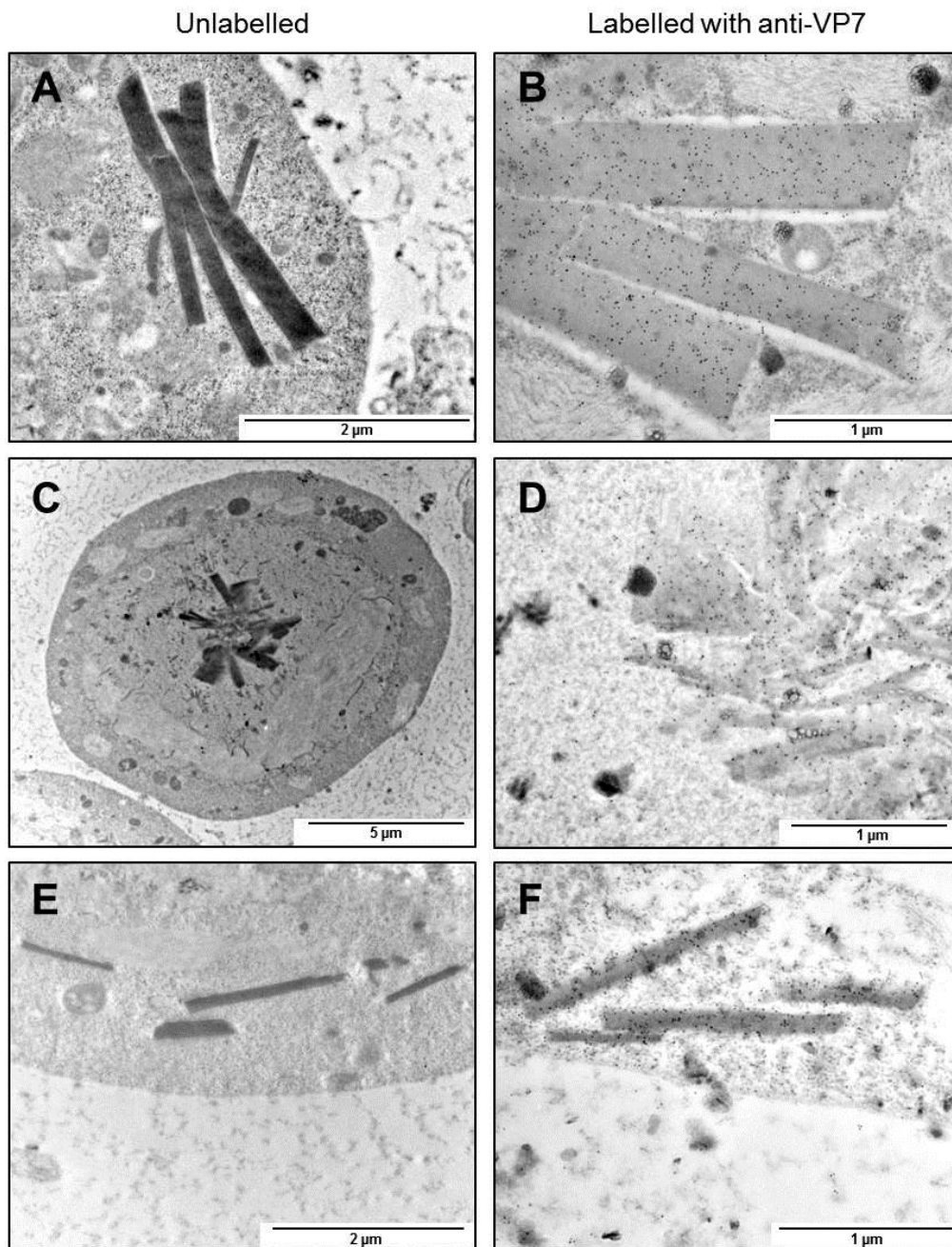
Fig. 26 TEM micrographs of unlabelled VP7-177 (left) or anti-VP7 labelled (right) VP7-177. Rosette-like structures are seen in A-D. At times however, single rods were observed (E and F). Immunogold labelling was done with anti-VP7 primary and gold-conjugated secondary antibodies. Scale bars represent 2 µm (A, E), 1 µm (B, D, F) and 2 µm (E).

After investigating both VP7-144 and VP7-177 we were able to progress to an investigation of VP7-200, the least soluble of the vector proteins.

VP7-200

The last of the vector proteins was VP7-200, the least soluble of the three vector proteins, and thus the most like WT VP7 in that regard. This protein was modified by inserting the amino acids KLSRVD downstream of amino acid 200 of AHSV-9 VP7. Immunofluorescence and confocal

53

microscopy showed that VP7-200 formed individual particles that associated to form larger rosette-like structures (Fig. 27). As with VP7-144 and VP7-177, labelling with anti-VP7 occurred on the outer edge of the individual particles, leading to a halo-like effect.

Multiple Z-stack analyses indicated that the rosette-like structures may have been somewhat hexagonal in nature when viewed from above (Fig. 28). Three dimensional reconstructions such as that seen in Figure 29 confirmed that this was indeed the case and also showed that some structures were more rigid than others. Furthermore, all structures appeared relatively flat in nature even though they did not form the rigid particles formed by WT VP7.

TEM showed larger VP7-200 rosette-like structures located mainly in the cytoplasm (Fig. 30). Individual VP7-200 particles appeared to be thinner than those of both WT VP7 and VP7-177 (Fig. 28), and appeared more rigid than the spindle-like structures formed by VP7-144 (Figs. 22 and 23). Immunogold labelling with anti-VP7 and gold-conjugated secondary antibodies confirmed that these structures were indeed VP7-200 (Fig. 31B, D, F).
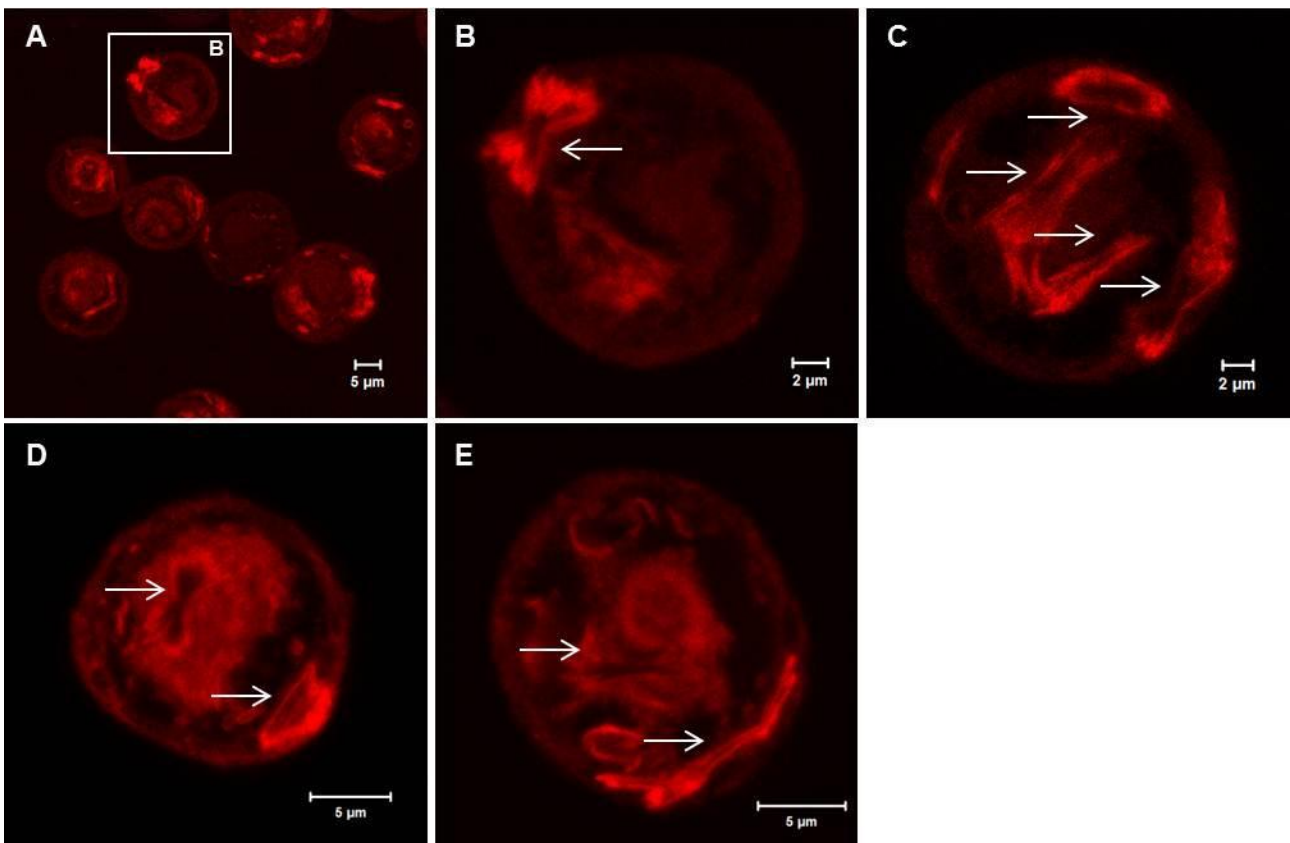
Fig. 27 Immunofluorescence images of Sf9 cells infected with Bac-VP7-200 (48 hpi). An enlargement of the cell in A shows that VP7-200 forms rosette-like structures (B). Such structures were observed in many cells and usually occurred in multiples (B-E). Immunolabelling was done using anti-VP7 (primary antibody) and anti-guinea pig-TRITC (red secondary antibody). Scale bars represent 5 µm (A, D, E) and 2 µm (B, C).

54
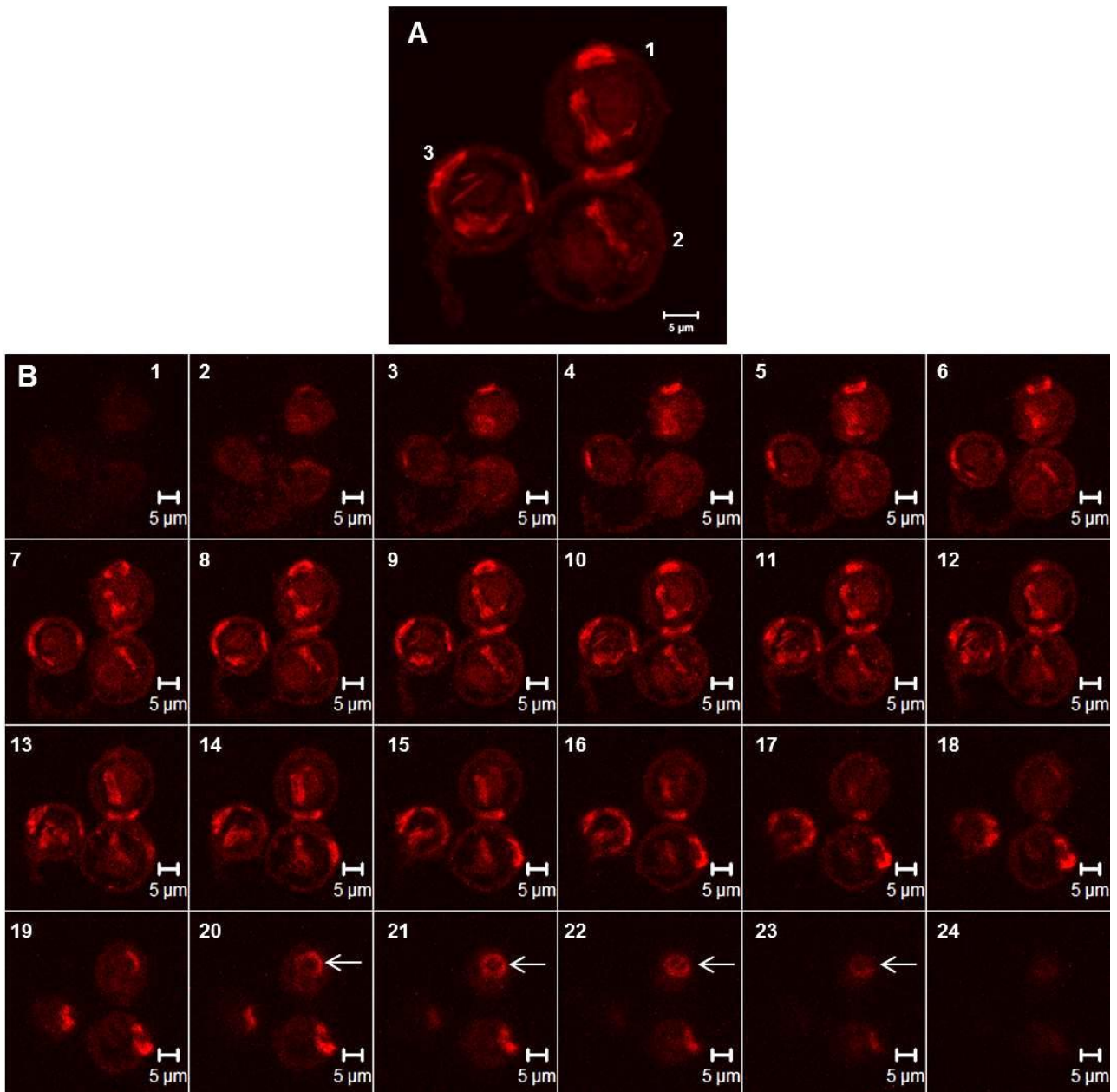
Fig. 28 Z-stack analysis of a field of Sf9 cells infected with Bac-VP7-200 (48 hpi, A). The Z-stack gallery of images taken at 0.8 μm intervals through the field is shown in B. Arrows in Panels 20-23 indicate that rosette-like structures may appear somewhat hexagonal from above. Immunolabelling was done with anti-VP7 (primary antibody) and anti-guinea pig-TRITC (red secondary antibody). Cells are labelled 1 through 3. Scale bars represent 5 μm.
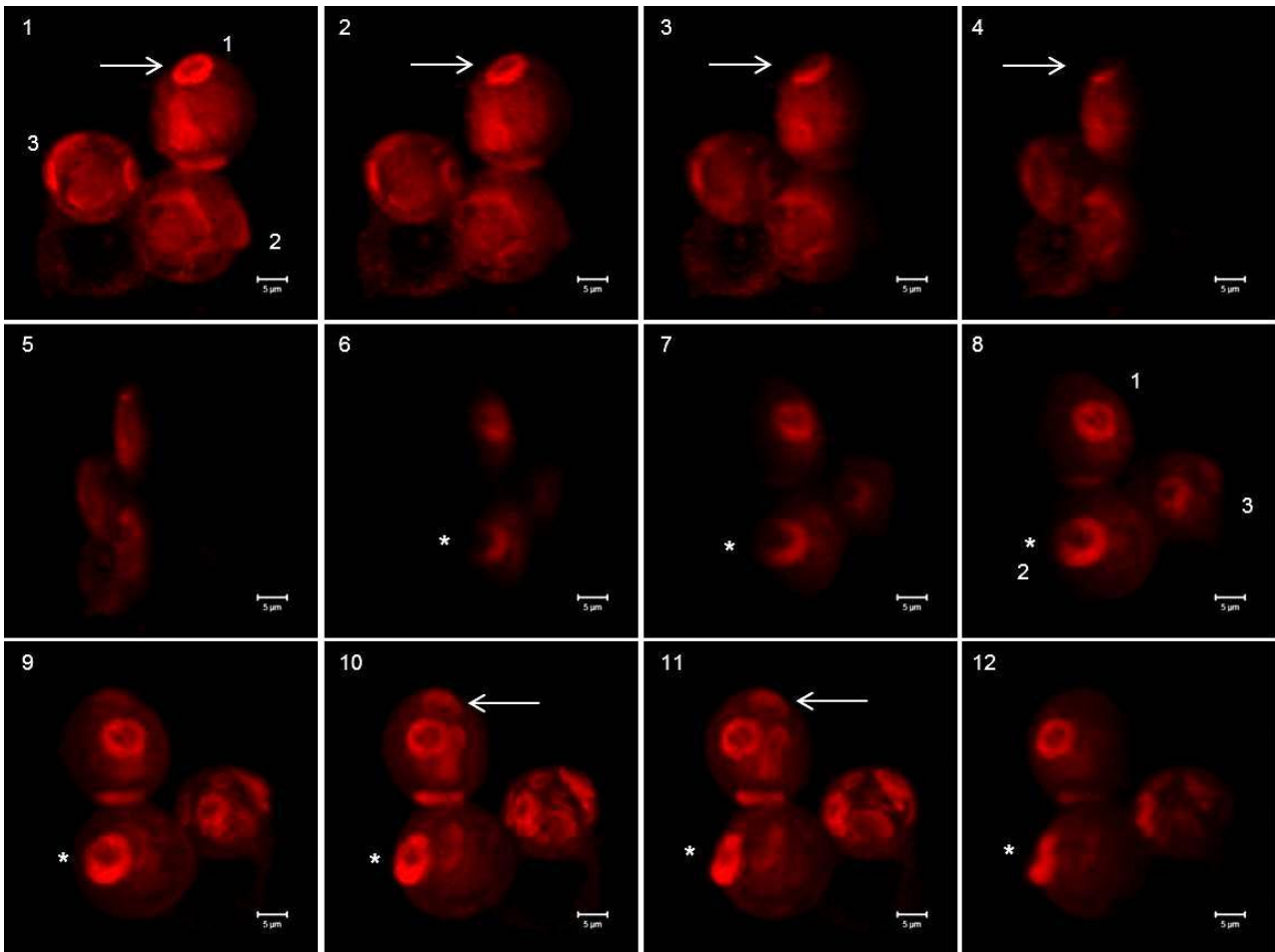
Fig. 29 Snapshots of a three-dimensional reconstruction of the Bac-VP7-200 infected Sf9 cells (48 hpi) in Figure 19. The reconstruction was rotated around the Y-axis in a clockwise manner, with 90˚ rotation between Panels 5 and 6, and 180˚ rotation shown in Panel 12. The VP7-200 particle (see arrow) in Cell 1 appeared hexagonal in nature at 0˚ (Panel 1) and with rotation of the field, also appeared hexagonal from the opposite side (Panel 11). Rotation of the particle in Cell 2 (Asterisk, Panels 6-12) showed that the larger particle appeared rosette-like from a 90˚ angle. Scale bars represent 5 µm.
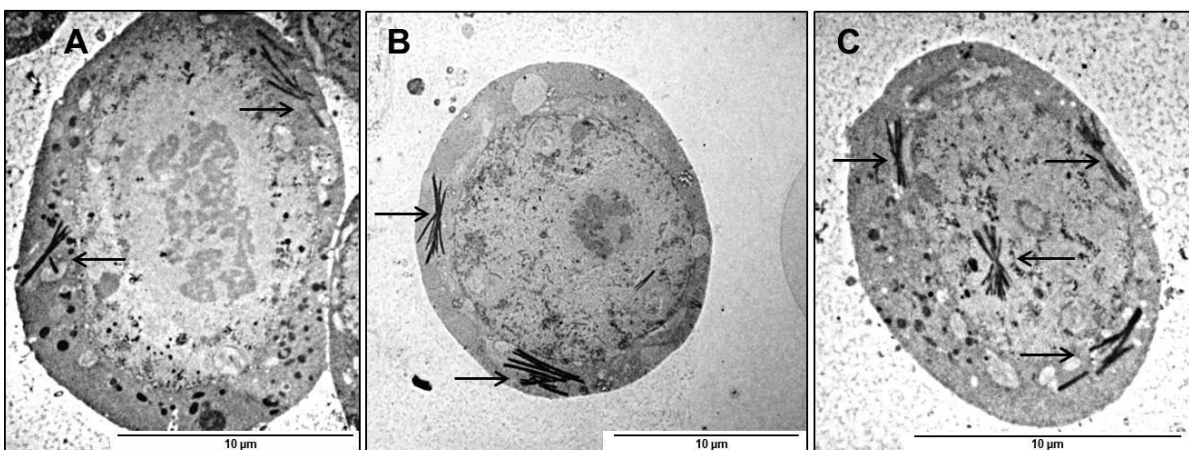
Fig. 30 TEM micrographs of Sf9 cells infected with Bac-VP7-200 (48 hpi). This protein forms rosette-like structures at multiple sites in the cell as indicated by the arrows in A to C. Scale bars represent 10 µm.

56
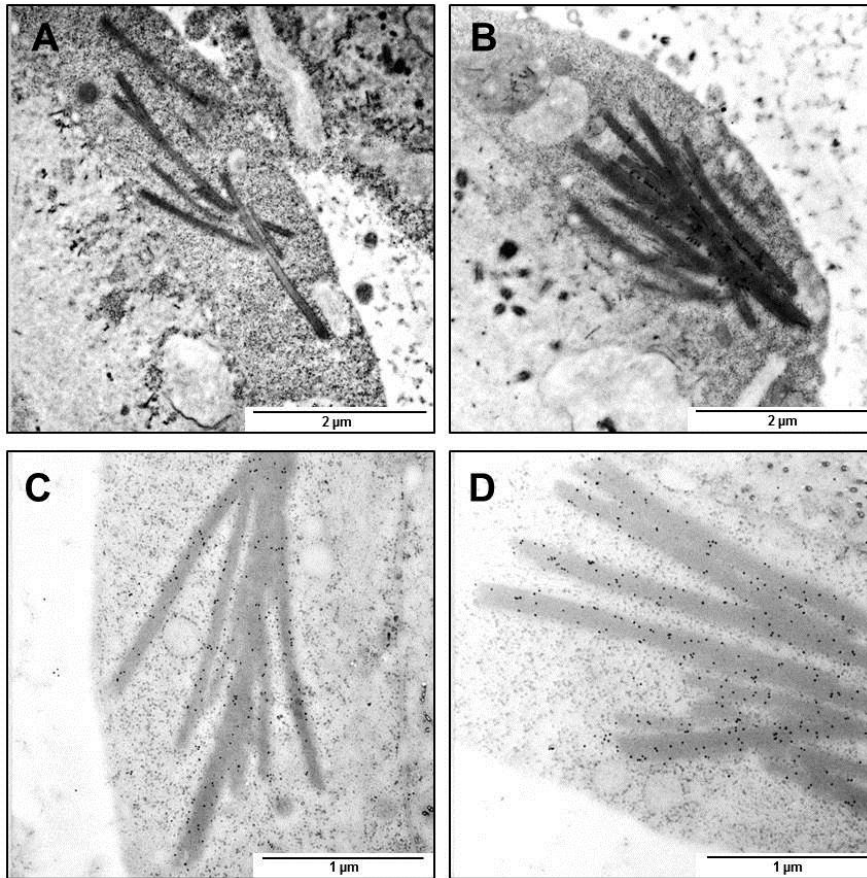
Fig. 31 TEM micrographs of Sf9 cells infected with Bac-VP7-200 (48 hpi). A and B show the rosette-like structures into which VP7-200 assembles. Immunogold labelling with anti-VP7 primary and gold-conjugated secondary antibodies (C and D) confirmed that these structure are indeed VP7-200. Scale bars represent 2 µm (A, B) and 1 µm (C, D).

The above results showed that all three vector proteins self-assembled to single/multiple sites in the cell but particle formation was affected to some extent. VP7-177 and VP7-200 formed particles most similar to those of WT VP7 thereby prompting further investigations thereof.

Effect of top domain modifications on the dimensions of AHSV VP7 particles

Once it had been observed that particles were still being formed by VP7-177 and VP7-200, and that VP7-177 particles appeared to show a closer resemblance to those of WT VP7, it was decided to compare the particles to those of the WT to determine what effect each modification had on the size of the particles themselves. In order to do this TEM micrographs were used and the length and thickness of several particles of each construct measured using iTEM software. The average length and thickness of each particle were then calculated and the results summarised in Table 4.

57

Table 4 A comparison of the length and width of VP7-177 and VP7-200 to WT VP7

Construct (Number of particles measured)	Length (nm)		Average length (nm)	Thickness (nm)		Average thickness (nm)
	From	**To**		**From**	**To**	
WT VP7 (23)	1 281	7 954	3 296	142	483	266
VP7-177 (56)	526	5 926	2 000	60	672	219
VP7-200 (75)	448	4 653	1 953	32	215	101

Due to sectioning through a cell, the readings representing the length of the particles are not as reliable as those representing the thickness thereof. This is so as sections through a flat WT VP7 hexagonal particle result in differences in length depending on where through the particle the section was made. The chances are slim that a section will be made exactly on the edge of the particle rather it is more likely that it will be made internally. Similar is true for VP7-177 and VP7-200 particles. Thus using WT VP7 as an example the lengths 1 280 nm and 7 954 nm may not represent the same particle. The former may represent a section though the widest point of a smaller particle or it may represent an internal section through a larger particle.

The length of VP7-177 ranged from 526 nm to 5926 nm, whilst that of VP7-200 ranged from 448 nm to 4 653 nm. These values are both lower than the WT and indicated that the particles were somewhat smaller on average than the WT. The average length of VP7-177 was calculated as 1 979 nm and that of VP7-200 calculated as 1953 nm. Thus, the sizes of the two mutant vector proteins were similar to one another but differed from the WT (3 275 nm), indicating that, on average, the vector particles were smaller than WT.

The readings pertaining to the thickness of the particles showed that on average, VP7-177 particles were closer in thickness to the WT than VP7-200 particles, thereby confirming what was suggested by TEM. VP7-200 particles (101 nm) were less than half the thickness of the WT (244 nm).

Summary

Table 5 summarises the differences between WT AHSV VP7 and the vector proteins containing minor modifications to the VP7 top domain. Previous findings are included here to aid in the comparison of WT VP7 and the three vector proteins. When analysing the vector proteins, Rutkowska *et al.* (2011) found that less than 10% of WT VP7 localises in the soluble fraction of a sucrose gradient. This changes, however, when modifying the top domain of the protein at sites 144 and 177. These modifications led to an increase of the overall solubility of the protein with VP7-144 being about 60% soluble and VP7-177 being about 30% soluble. No significant change

58

was observed for the solubility of VP7-200. Thus, VP7-200 is most similar to WT VP7 in this regard. Furthermore, all proteins were able to form trimers (Rutkowska *et al.* 2011).
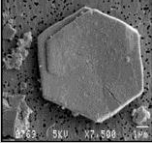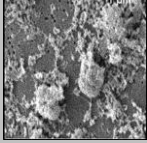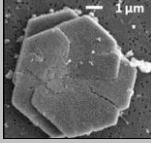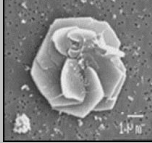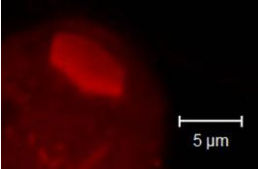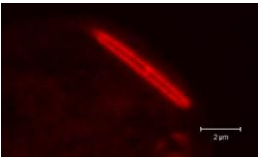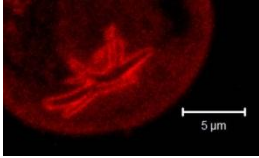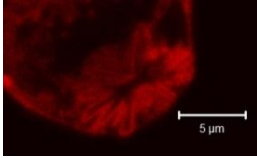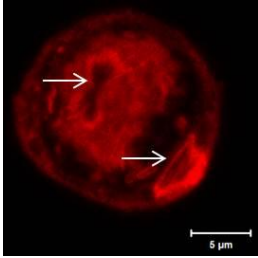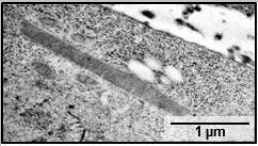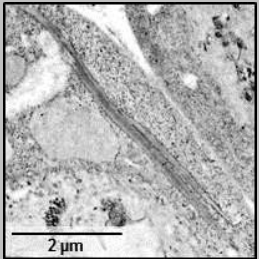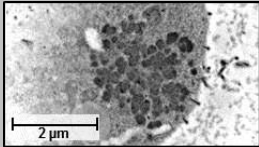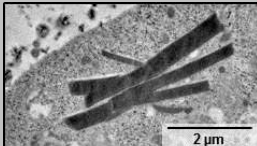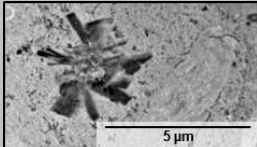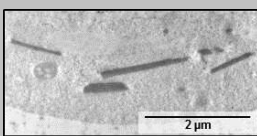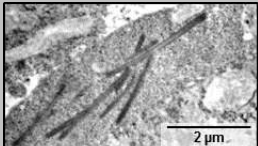
As shown in Table 5, previous work involving scanning electron microscopy (SEM) of purified particles showed the flat, hexagonal particles normally associated with the WT. However, in the case of VP7-177 and VP7-200, the particles were no longer seen to have the rigid shape of the WT. The particles appeared rosette-like, with VP7 sheets layering on top of one another. The overall shape of the particles was however still somewhat hexagonal when viewed from above.

The CSLM and TEM results generated here for WT VP7 were consistent with SEM results (Table 5). WT VP7 appeared flat and hexagonal under the confocal and rod-like particles were also observed when the hexagonal particles were viewed from a 90˚ angle. CSLM also indicated that there are usually multiple assembly sites in a single cell.

TEM showed that VP7-144 forms spindle-like structures in infected cells. These structures taper in at both ends and lack the rigidity of WT VP7. Multiple spindle-like structures were observed to associate with one another to form larger spindle aggregates, which appeared as small, loosely associated protein structures via cross sectioning (Table 5).

Confirming what has been observed under the SEM, VP7-177 was observed as rosette-like structures under the TEM (Table 5). Single rod-like particles were also observed occasionally. Furthermore, TEM showed that on an ultrastructural level VP7-177 particles seemed quite similar to WT VP7 particles. VP7-200 also formed rosette-like structures but the nature of each particle was different to those of WT VP7 and VP7-177, with each VP7-200 particle being thinner than WT VP7 and VP7-177. Z-stack analysis confirmed that the rosette-like VP7-200 structures appeared hexagonal in nature when viewed from above.

Table 5 Summary of the differences between WT VP7 and the minor top domain VP7 mutants

	WT VP7	VP7-144	VP7-177	VP7-200
Solubility (%) (Rutkowska *et al.* 2011)	<10	~60	~30	<10
Able to form trimers? (Rutkowska *et al.* 2011)	Yes	Yes	Yes	Yes
SEM (Kretzmann 2006; Rutkowska *et al.* 2011; Rutkowska 2012)	Hexagonal		Rosette-like	Rosette-like
Confocal	Hexagonal Rod-like	Spindle-like	Rosette-like	Rosette-like
TEM	Rod-like	Spindle-like Foci-like (cross section)	Rosette-like Rod-like	Rosette-like
Terminology	Flat hexagonal or rod-like crystalline-like particles.	Spindle-like structures associating to form spindle aggregates. Cross sectioning shows small, loosely associated aggregates.	Rosette-like structures composed of rigid VP7-177 sheets.	Rosette-like structures composed of thin VP7-200 sheets.

Taken together the results of this section indicate that the self-assembly and localisation of AHSV VP7 are not affected by minor modifications to the top domain. The particle forming ability and nature of the protein is, however, somewhat affected by these modifications.

2.3.3 Effect of eGFP insertion on AHSV VP7 self-assembly and particle formation

This section deals with the insertion of a bulky protein, namely the marker protein eGFP, into the 144, 177 and 200 sites of the AHSV VP7 top domain, and the effect thereof on VP7 self-assembly and particle formation. Split into three parts, this section deals with an investigation into the kinetics of VP7-144-eGFP and VP7-200-eGFP assembly (2.3.3.1), followed by an investigation into the localisation and ultrastructure of the VP7-eGFP fusions (2.3.3.2). Lastly, Part 2.3.3.3 deals with the fate of misfolded VP7-eGFP fusions in the cell.

2.3.3.1 Monitoring fluorescing and total relative VP7-eGFP protein following sucrose gradient fractionation at different times post infection

To investigate whether or not the aggregation of VP7-eGFP protein is dependent on time or the over-expression of the protein, VP7-144-eGFP and VP7-200-eGFP were expressed in Sf9 cells by means of recombinant baculoviruses and harvested at 24, 30, 38 or 48 hpi. The cells were lysed (2.2.5), and either treated with L-arginine or left untreated. Both lysates were centrifuged through 30-80% sucrose gradients, the fractions collected and pellets resuspended in 1 x PBS. Under these sucrose density sedimentation conditions, soluble protein was expected to settle in the upper part of the gradient (fractions 7-10) whereas the particulate protein was expected to migrate toward the bottom of the gradient (fractions 1-5). The protein content of each fraction and the pellet was analysed via Western blot analysis (anti-GFP primary antibody, Table 2, Section 2.2) and the relative amounts of protein on each blot quantified using EZQuant software (EZQuant, 2.2.8). Following this, the relative fluorescence units of the same samples were measured using the Fluoroskan Ascent FL Fluorometer (Thermo Labsytems, 2.2.9). Multiple repeats of the experiment were performed, and a representative example shown here.

Figure 32 shows the Western blots obtained for VP7-144-eGFP and VP7-200-eGFP, both before (Figs. 32A and 32C) and after (Figs. 32B and 32D) treatment with L-arginine. In each case, the pellet was loaded first, followed by the gradient fractions from bottom (1), to top (10 or 11). Although not shown in Figure 32D, some degradation of VP7-200-eGFP was observed at 48 hpi after L-arginine treatment. Thus this time point was discarded from further analyses. Such degradation was also observed by Rutkowska (2012), and may occur due to the activation of cellular proteases by L-arginine.
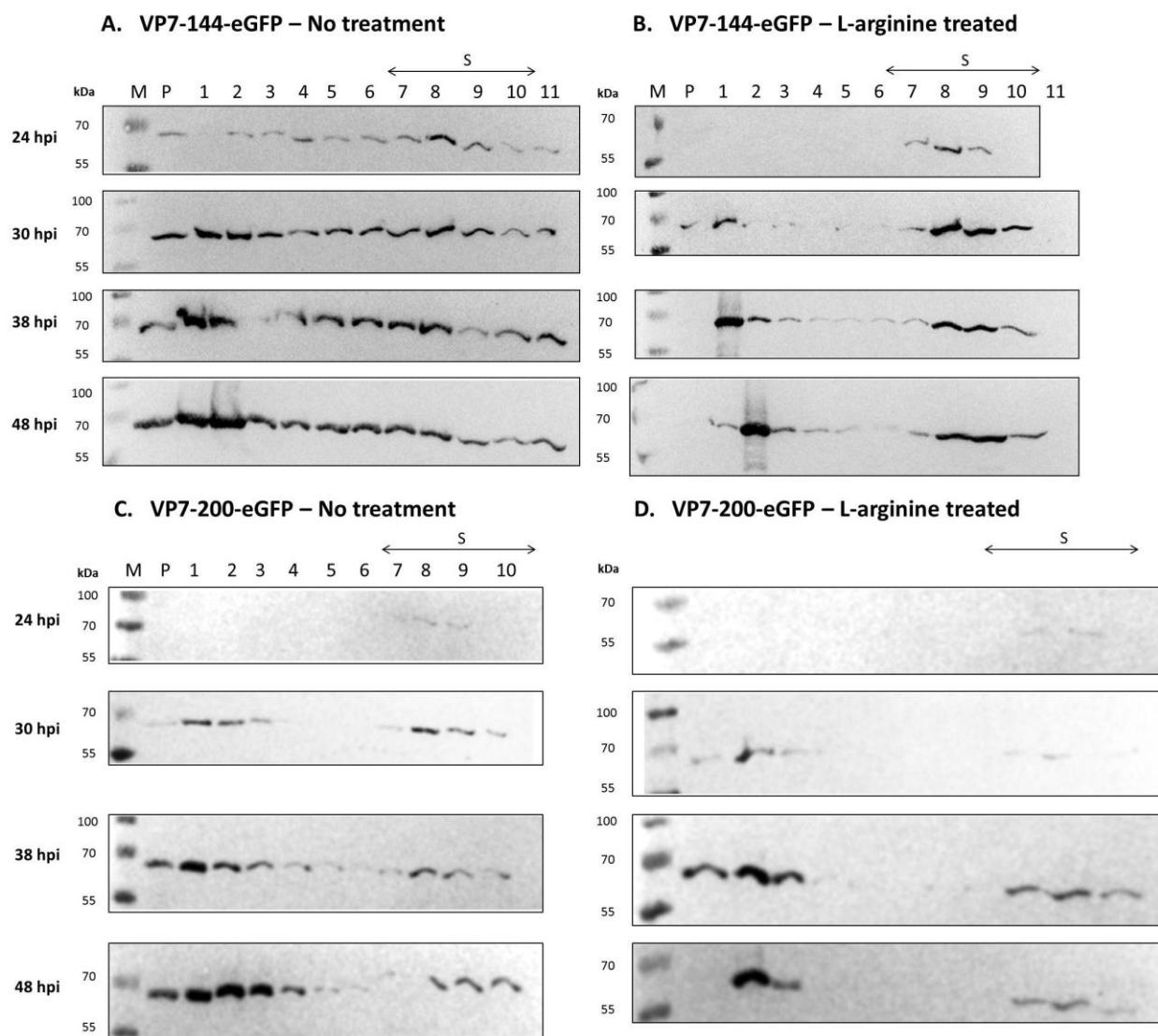
61

Fig. 32 Western blot analysis of untreated (A, C) and L-arginine treated (B, D) VP7-144-eGFP or VP7-200-eGFP protein in the pellet and fractions of 30-80% sucrose gradients from bottom (lane 1) to top (lane 10 or 11) at 24, 30, 38 and 48 hpi. S = Soluble region, M = marker (PageRuler, Fermentas) and P = Pellet.

The relative amount of VP7-eGFP protein was then quantified from the Western blots in Figure 32 using EZQuant software (EZQuant Ltd., 2.2.6) and compared to the relative fluorescence emitted by each corresponding sample. The results are shown in Figures 33 and 34.

Early in the infection cycle, the majority of the fluorescing VP7-144-eGFP was located in the soluble fractions (Fig. 33A, fractions 7-10). With time, there was a subsequent increase in the amount of soluble fluorescing proteins (Figs. 33B-D) but the largest increase appeared to be in the amount of VP7-144-eGFP associated with the particulate fractions at 48 hpi (fractions 1 to 5) suggesting some form of aggregation (Fig. 33D). The results indicate that with time after infection, and with the increase in the amount of protein expressed, an increasing amount of the presumably correctly folded fluorescing VP7-144-eGFP fusion protein becomes aggregated into larger structures. At 48 hpi the majority (66%) of fluorescence emitted from the protein was located in the

62

particulate fractions, with some also located in the intermediate region. From Figures 33A-D it was apparent that the aggregation of VP7-144-eGFP may start as early as 30 hpi. Following L-arginine treatment however, the majority of fluorescing VP7-144-eGFP was located in the soluble fractions (Figs. 33E-H), with a corresponding decrease observed in the particulate fractions. Thus, the aggregation of VP7-144-eGFP is reversible.

Although VP7-144-eGFP was correctly folded, soluble and fluorescing at 24 hpi (Fig. 33A), it was, however, apparent that over time there was an increase in the amount of particulate protein. Over time there was also an increase in the amount of fluorescence associated with these fractions (Fig. 33B-D). The fluorescence that remained associated with the particulate fractions after L-arginine treatment (Fig. 32F-H) may have represented some correctly folded VP7-144-eGFP trapped in particulate protein. Alternatively, fluorescing VP7-144-eGFP protein may aggregate into a particulate version that cannot be re-solubilised by treatment with L-arginine. From 30 hpi, the amount of total relative protein in the particulate fractions exceeded the amount of fluorescing protein, thus from Figures 33F-H it was also apparent that there was a large amount of non-fluorescing protein associated with the particulate fractions. The lack of fluorescence of this protein suggested that it may have been misfolded. Alternatively, not all of the protein associated with the particulate fractions may have fluoresced to the same extent.

The nature of VP7-200-eGFP was markedly different to that of VP7-144-eGFP (Fig. 34). At 24 hpi, all of the expressed VP7-200-eGFP was correctly folded and fluorescing (Fig. 34A) but this changed from 30 hpi onwards. A soluble, fluorescing fraction was observed at each time point but the synthesis of particulate protein increased dramatically from 30 to 48 hpi (Figs. 34B-D). In contrast to VP7-144-eGFP, the fluorescing VP7-200-eGFP component remained mainly associated with the soluble fractions, and there was little to no indication of a large degree of reversible fluorescing VP7-200-eGFP aggregation (Figs. 34B-D). The lack of fluorescence associated with the vast amount of particulate VP7-200-eGFP indicated that in contrast to VP7-144-eGFP, this protein was largely misfolded and non-fluorescing.

In contrast to VP7-144-eGFP, treatment with L-arginine had little effect on VP7-200-eGFP, thereby confirming that this protein is a largely misfolded and non-fluorescing protein, the synthesis of which increases over time (Figs. 34E-G). As was the case with VP7-144-eGFP, some fluorescence was still associated with the particulate fractions following treatment, thereby indicating that some correctly folded protein was trapped within the ever-increasing amount of misfolded VP7-200-eGFP. As suggested in the case of VP7-144-eGFP it was also possible that some fluorescing VP7-200-eGFP protein aggregates into a particulate form that is unable to be L-arginine solubilised.

63

VP7-144-eGFP No treatment
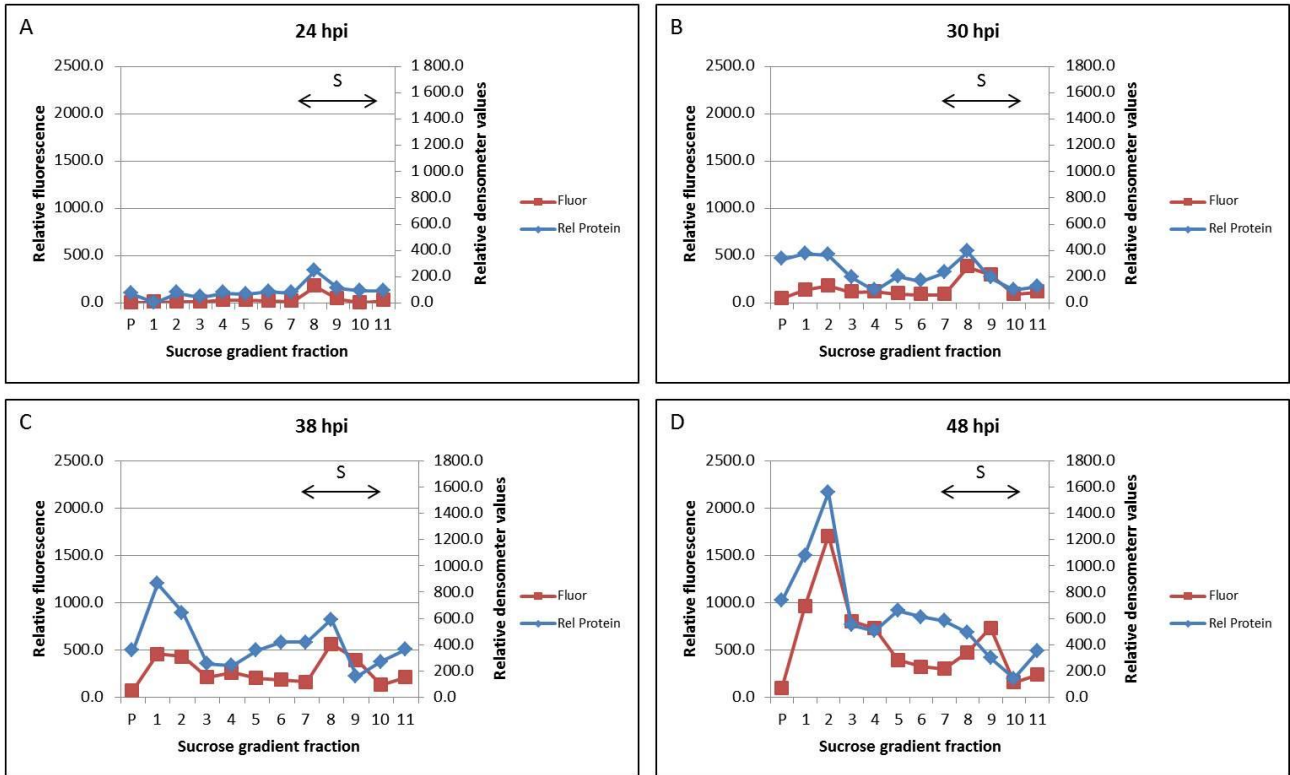
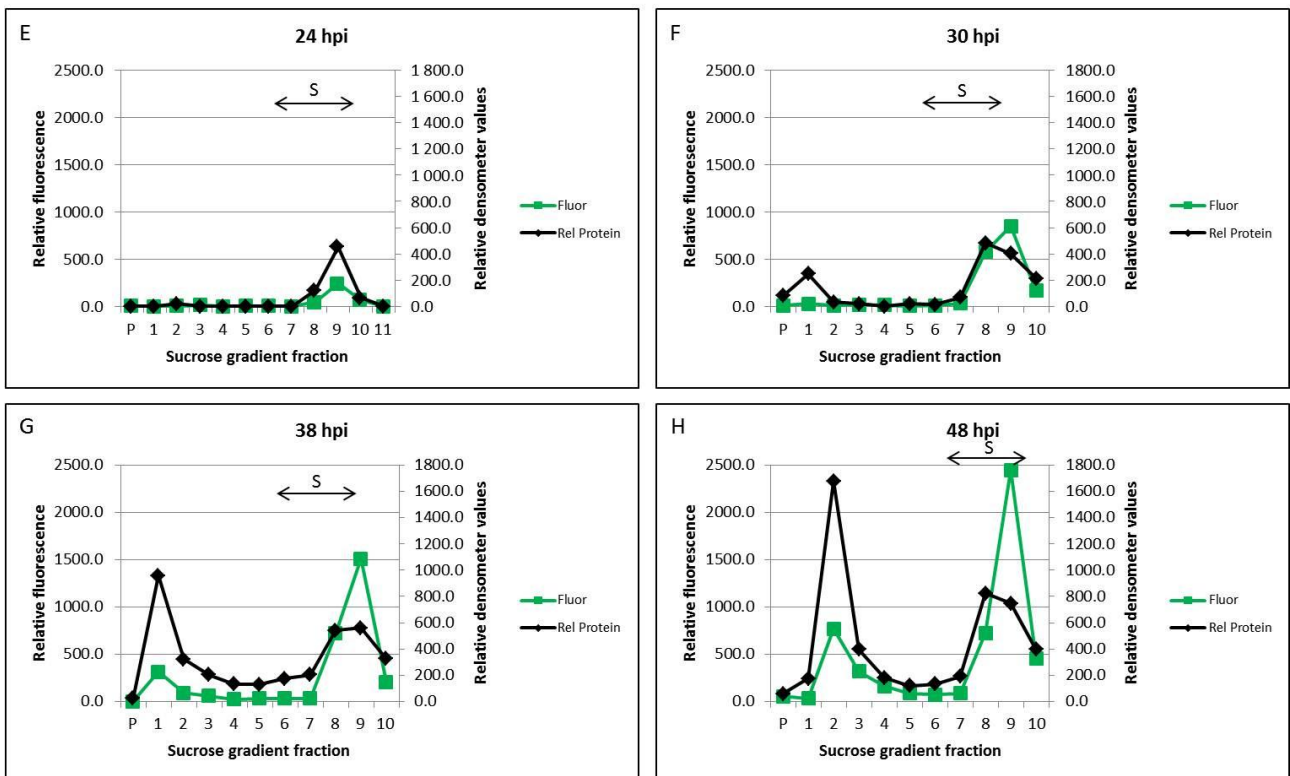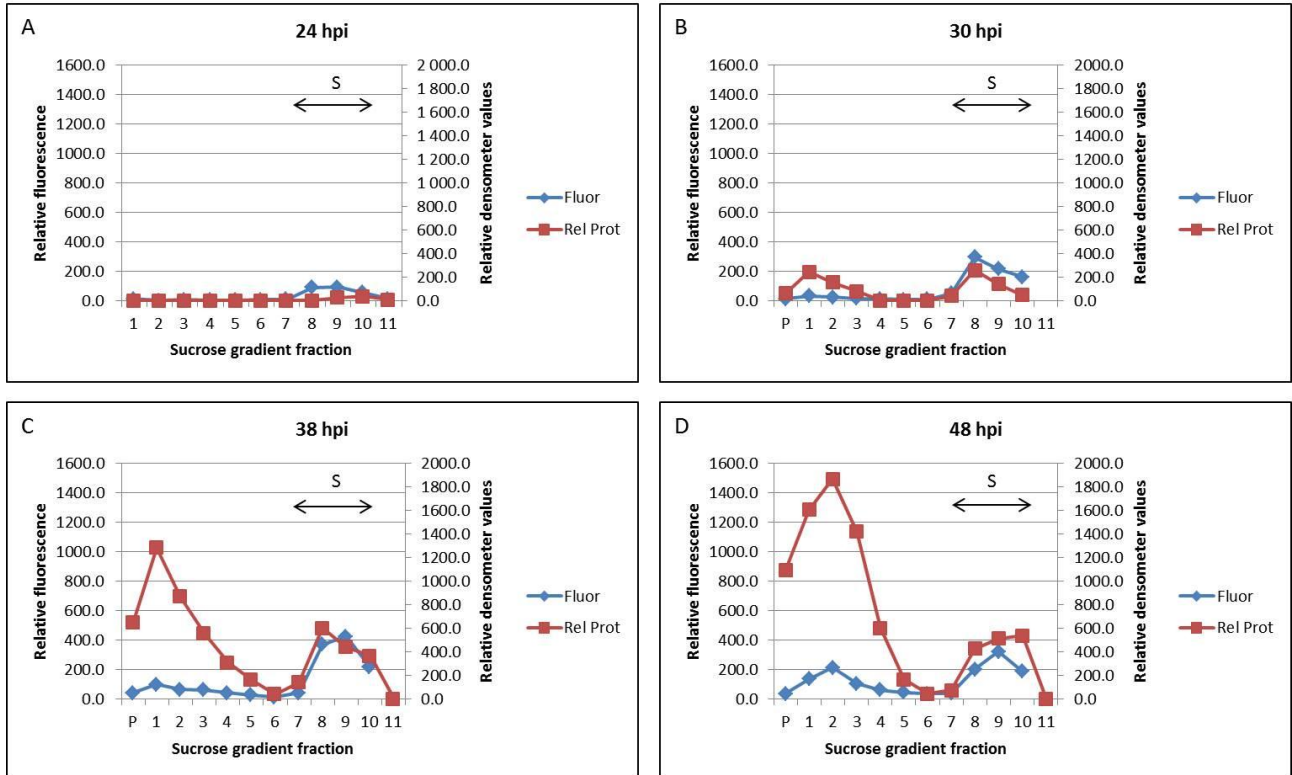## VP7-144-eGFP L-arginine treated

Fig. 33 Comparison between fluorescing and total relative protein of VP7-144-eGFP in the fractions of 30-80% sucrose gradients from bottom (lane 1) to top (lane 10 or 11), both before (A-D) and after (E-H) treatment with L-arginine and at different times post infection. S = soluble region and P = pellet.

64

VP7-200-eGFP No treatment

A — 24 hpi

B — 30 hpi

C — 38 hpi

D — 48 hpi

VP7-200-eGFP L-arginine treated
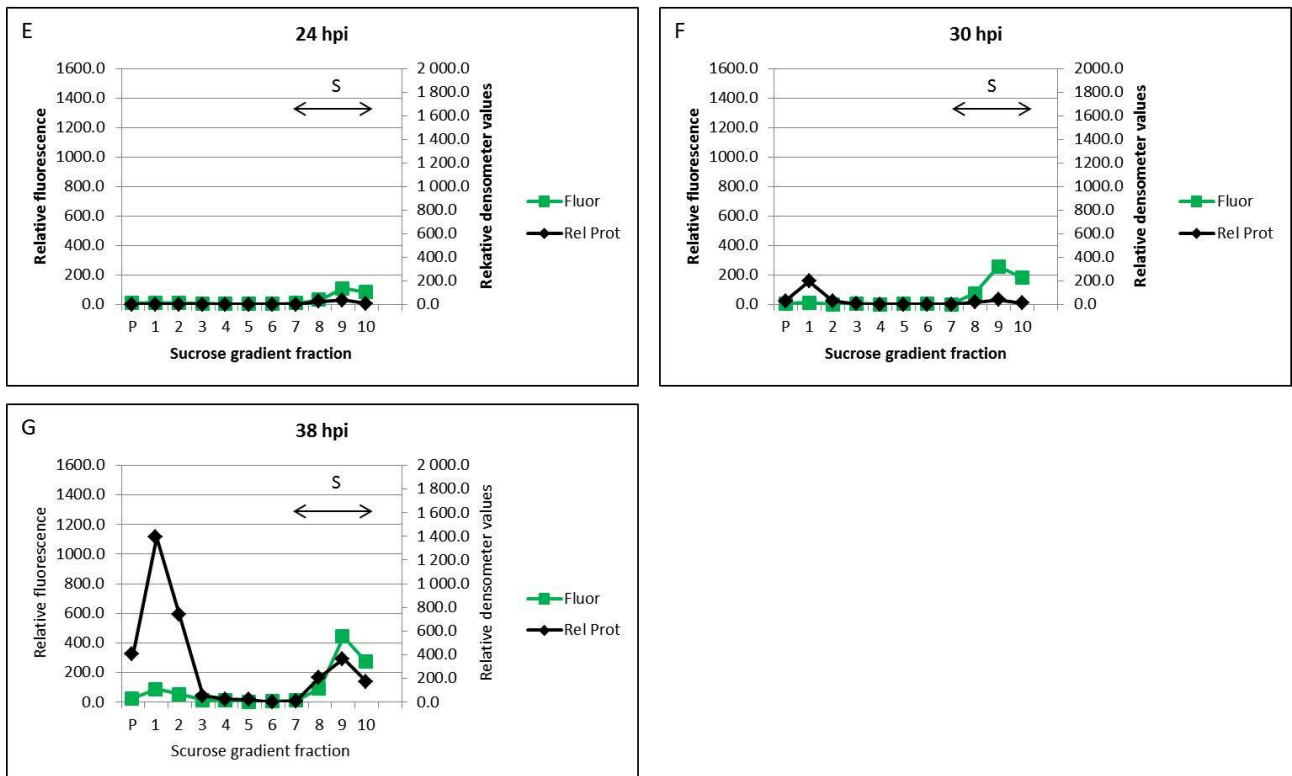
E — 24 hpi

F — 30 hpi

G — 38 hpi

Fig. 34 Comparison between fluorescing and total relative protein of VP7-200-eGFP in the fractions of 30-80% sucrose gradients from bottom (lane 1) to top (lane 10 or 11), both before (A-D) and after (E-G) treatment with L-arginine and at different times post infection. S = soluble region and P = pellet.

65

The results of this section show the tendency of VP7-144-eGFP to reversibly aggregate, a process that may occur as early as 30 hpi. This suggests that the aggregation of the VP7-eGFP proteins occurs at comparatively low VP7-eGFP protein concentrations and not only as a result of the protein over-expression that inevitably occurs at the later stages of the infection cycle. The site of the insertion may influence the tendency of correctly folded, fluorescing protein to aggregate. This could also be due to the trimeric nature and stability of the protein as VP7-144-eGFP is largely trimeric, whereas VP7-200-eGFP is largely monomeric in nature, and its trimers being less stable than VP7-144-eGFP trimers (Rutkowska 2012). VP7-200-eGFP was shown to be a largely misfolded, non-fluorescing protein. This too does not appear to be dependent on time or the over-expression of protein at the later stages of the infection cycle.

Next, the effect of the eGFP insertion on the self-assembly and particle formation of AHSV VP7 was investigated.

2.3.3.2 Subcellular localisation and ultrastructure of the VP7-eGFP constructs

In order to investigate the effect of the insertion of eGFP into different sites of the top domain of AHSV VP7 a dual microscopy approach similar to that employed in Section 2.3.2 was used here. Sf9 cells were infected with recombinant baculoviruses expressing VP7-144-eGFP, VP7-177-eGFP or VP7-200-eGFP and at 48 hpi were prepared for direct immunofluorescence or preserved by HPF-FS for TEM. Anti-VP7 or anti-GFP primary and gold-conjugated secondary antibodies were used for immunogold labelling and TEM. Uninfected (mock infected) and WT-Bac infected cells were used as controls in each experiment. We began this part of the study with VP7-144-eGFP, the most soluble of the VP7-eGFP fusions.

VP7-144-eGFP

Confocal microscopy showed that VP7-144-eGFP formed large foci of strong fluorescence (Fig. 35). Located mainly in the cytoplasm, these structures were irregular in shape (Figs. 35D, E, F) and appeared to be composed of smaller aggregates that increased in size, and decreased in number with the progression of the infection cycle (Fig. 35G). These smaller aggregates were observed in the cytoplasm, mostly at earlier stages of the infection cycle, but were almost completely absent in cells with large foci (Fig. 35H).

Z-stack analyses, as well as the resulting 3D reconstructions were used to further investigate the nature of the foci formed by VP7-144-eGFP. A Z-stack analysis was done at 1 µm intervals through the cell in Figure 36A and indicated that the focus of fluorescence in that particular cell was large, spanning almost the entire cell. The subsequent 3D reconstruction illustrated that the focus was indeed large and located in its entirety in the cytoplasm (Fig, 37). Furthermore, this

66

reconstruction showed that the foci formed by VP7-144-eGFP are not flat in nature but rather are elongated spherical structures (Panels 13-14, Fig. 37).

The large structures visualised under the confocal were visualised as large, irregularly shaped electron-dense protein aggregates under the TEM (Fig. 38). Smaller aggregates resembling those visualised under the confocal microscope were also observed in the cytoplasm (Fig. 38C, D) and appeared to migrate though the cytoplasm toward a larger, more rigid structure (Fig. 38E-H). Positive immunogold labelling with anti-VP7 and anti-GFP confirmed that both the larger and smaller aggregates were in fact VP7-eGFP related proteins (Fig. 39).
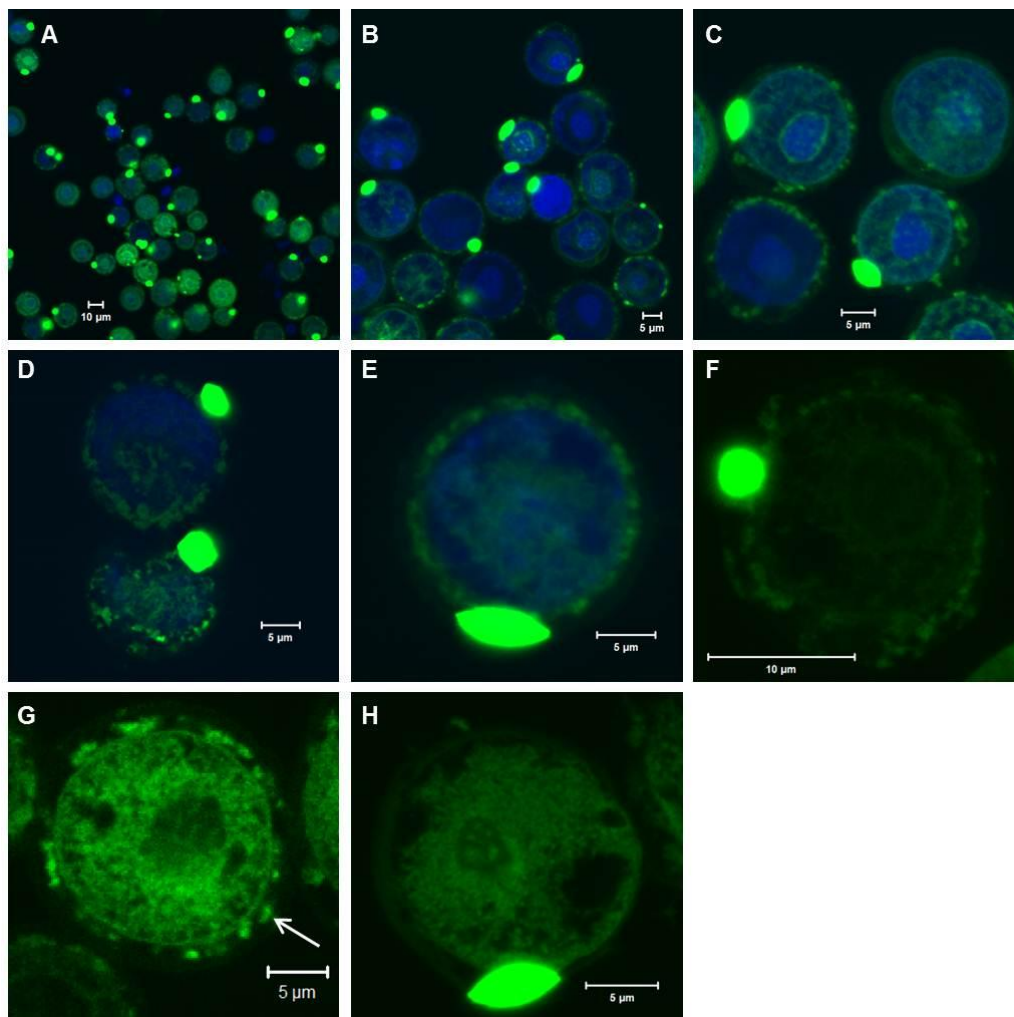

Fig. 35 Direct immunofluorescence images of Bac-VP7-144-eGFP infected Sf9 cells (48 hpi). The larger fields in A-C show that VP7-144-eGFP assembles to foci of fluorescence that are located mainly in the cytoplasm. These foci are irregular in shape (D-F) and appear to be composed of smaller protein aggregates (G) that increase in size and decrease in number (H) during the progression of the infection cycle. Nuclear staining was done with DAPI (blue). Scale bars represent 10 µm (A, F) and 5 µm (B-E, G, H).
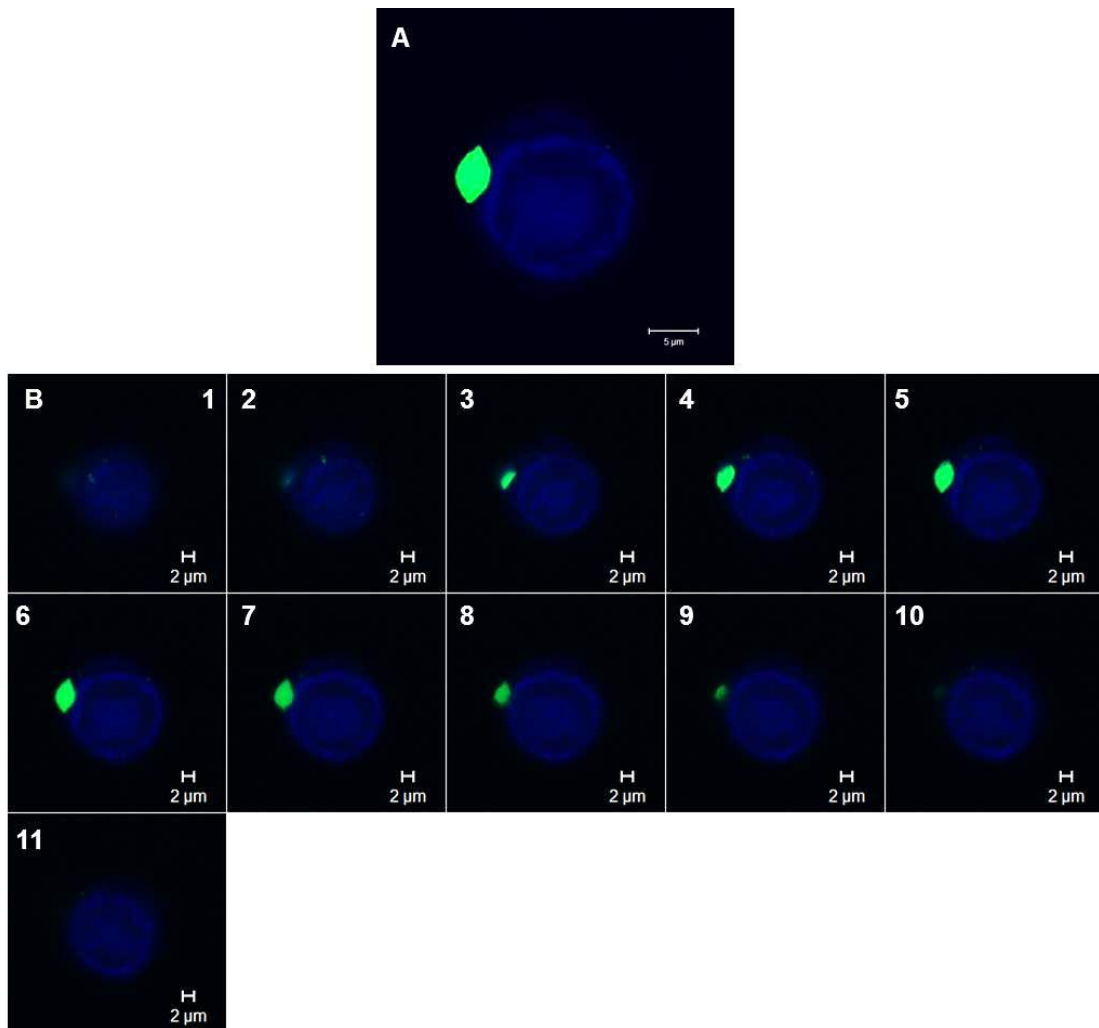
Fig. 36 Z-stack analysis of a Bac-VP7-144-eGFP infected Sf9 cell (48 hpi). The Z-stack gallery of images taken at 1 μm intervals through the cell is shown in B. VP7-144-eGFP formed a large focus of fluorescence located in the cytoplasm. Nuclear staining was done with DAPI (blue). Scale bars represent 5 μm (A) and 2 μm (B).
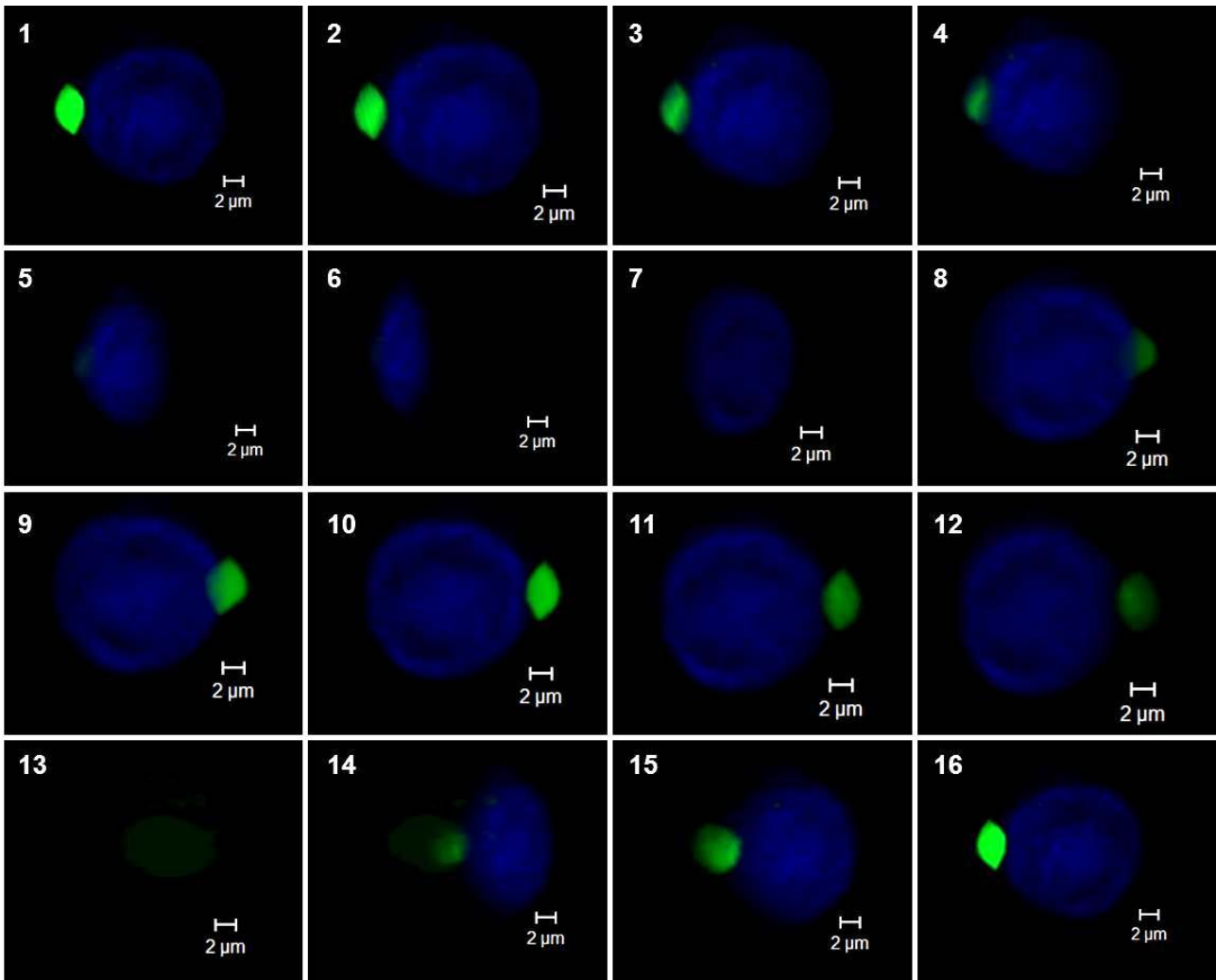
Fig. 37 Snapshots of a three-dimensional reconstruction of the Bac-VP7-144-eGFP infected Sf9 cell shown in Figure 4A. The reconstruction was rotated around the Y-axis in a clockwise manner, with 90˚ rotation between Panels 6 and 7, 180˚ rotation in Panel 10, 270˚ rotation in Panel 13 and 360˚ shown in Panel 16. This rotation around the Y-axis shows that the VP7-144-eGFP focus was not flat but rather, large and somewhat oval in shape. Scale bars represent 2 µm.
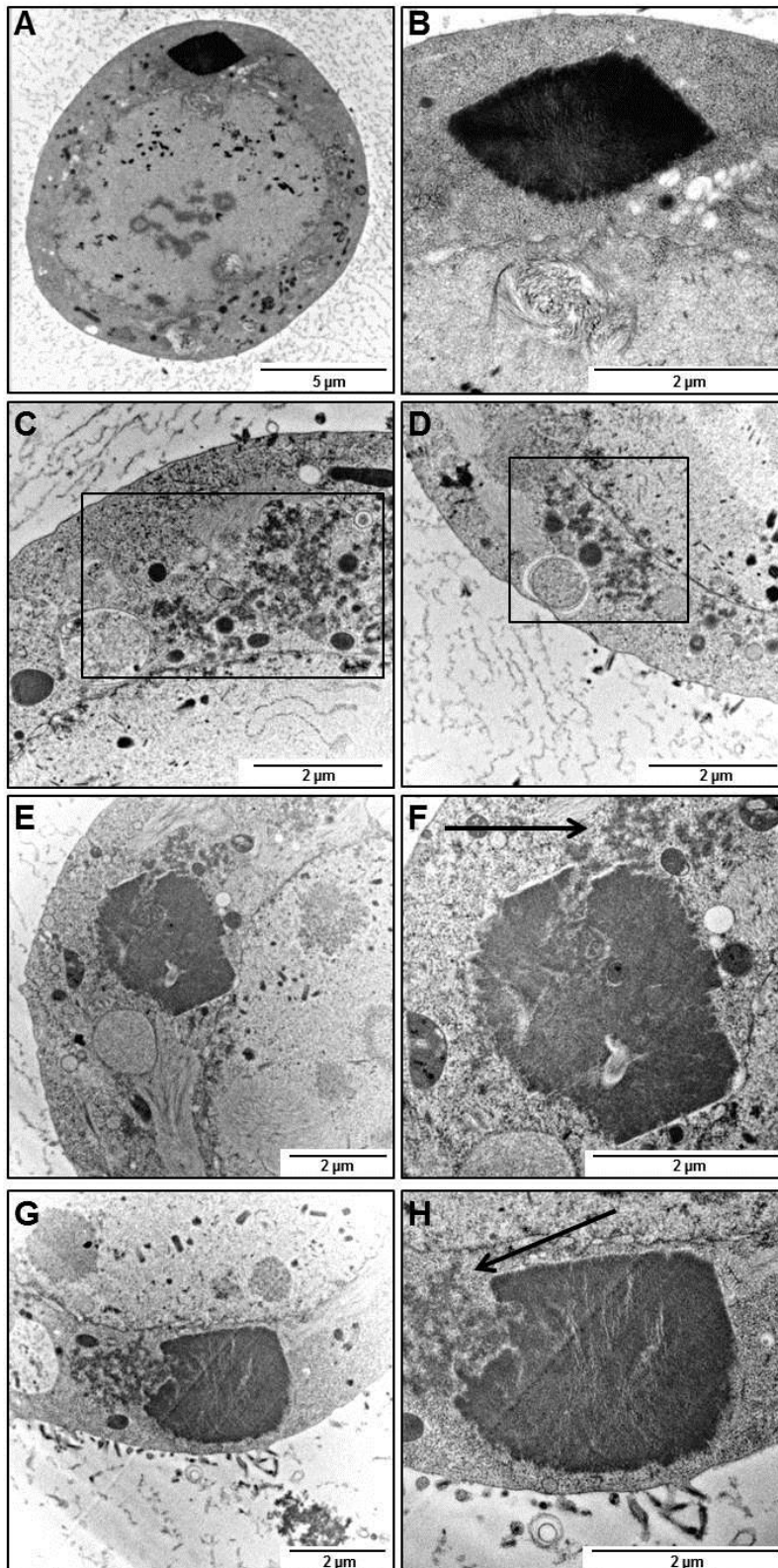
Fig. 38 TEM micrographs of Bac-VP7-144-eGFP infected Sf9 cells (48 hpi). Large, irregular protein aggregates were observed mainly in the cytoplasm (A), with an enlargement of such a structure seen in B. These large structures appeared to be composed of smaller protein aggregates (C, D) that increase in size and decrease in number with the progression of the infection cycle. The migration of the smaller aggregates results in structures such as those observed in E-H. Arrows indicate the smaller aggregates accumulating to the larger structures. Scale bars represent 5 μm (A) and 2 μm (B-H).
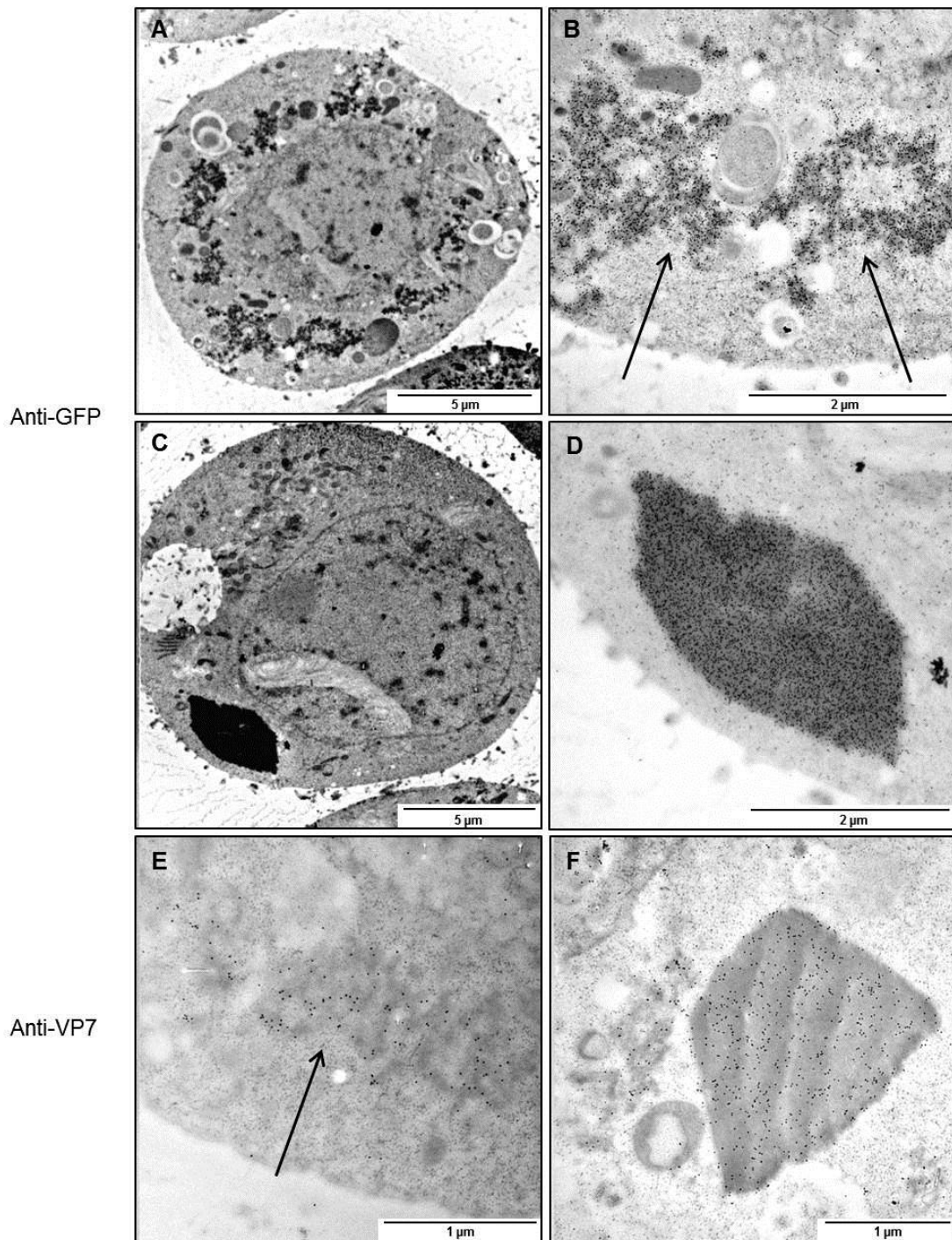
70

Fig. 39 TEM micrographs of VP7-144-eGFP immunogold labelled with either anti-GFP (A-D) or anti-VP7 (E, F) primary and gold-conjugated secondary antibodies. B and D are enlargements of the fields in A and C respectively. VP7-144-eGFP is visualised as large irregular structures (A-D, F), or smaller aggregates (arrows in B, E). Scale bars represent 5 µm (A, C), 2 µm (B, D) and 1 µm (E, F).

VP7-177-eGFP

The next VP7-eGFP fusion was VP7-177-eGFP, the fusion protein with intermediate solubility. In order to view these structures on a cellular level, direct immunofluorescence was performed on Sf9 cells expressing VP7-177-eGFP. As shown in Figure 40, multiple small foci of strong fluorescence were observed in Bac-VP7-177-eGFP infected cells, as opposed to the large, single focus of

71

fluorescence observed in Bac-VP7-144-eGFP infected Sf9 cells. Higher magnifications suggested that these foci were spherical in nature, and that they were formed by the smaller aggregates shown in Figure 40E.

In order to confirm whether or not the foci formed by VP7-177-eGFP were flat or spherical in nature, Z stack analyses were performed. The Z-stack shown in Figure 41 showed multiple foci of strong fluorescence and the subsequent 3D reconstruction (Fig. 42) showed that these foci were spherical in nature and caused distortion of the plasma membrane, causing the cytoplasm to bulge out slightly.

Small protein aggregates, similar to those observed for VP7-144-eGFP at the earlier stages of the infection cycle, were observed for VP7-177-eGFP under the TEM (Fig. 43B, D). These structures lacked the rigidity of the larger structures formed by VP7-144-eGFP (Figs. 38 and 39).

In order to determine whether or not these structures were VP7-eGFP specific, immunogold labelling using both anti-VP7 and anti-GFP was performed. Labelling with both anti-GFP and anti-VP7 primary antibodies confirmed that that the smaller, loosely associated particles were indeed VP7-eGFP related proteins (Fig. 44A-F).

In addition to positive labelling of the smaller protein aggregates, positive labelling was also observed for structures such as those seen in Figures 44G and H. These structures were irregular in shape but were not as large or electron dense as the large structures formed by VP7-144-eGFP (Figs. 38 and 39).
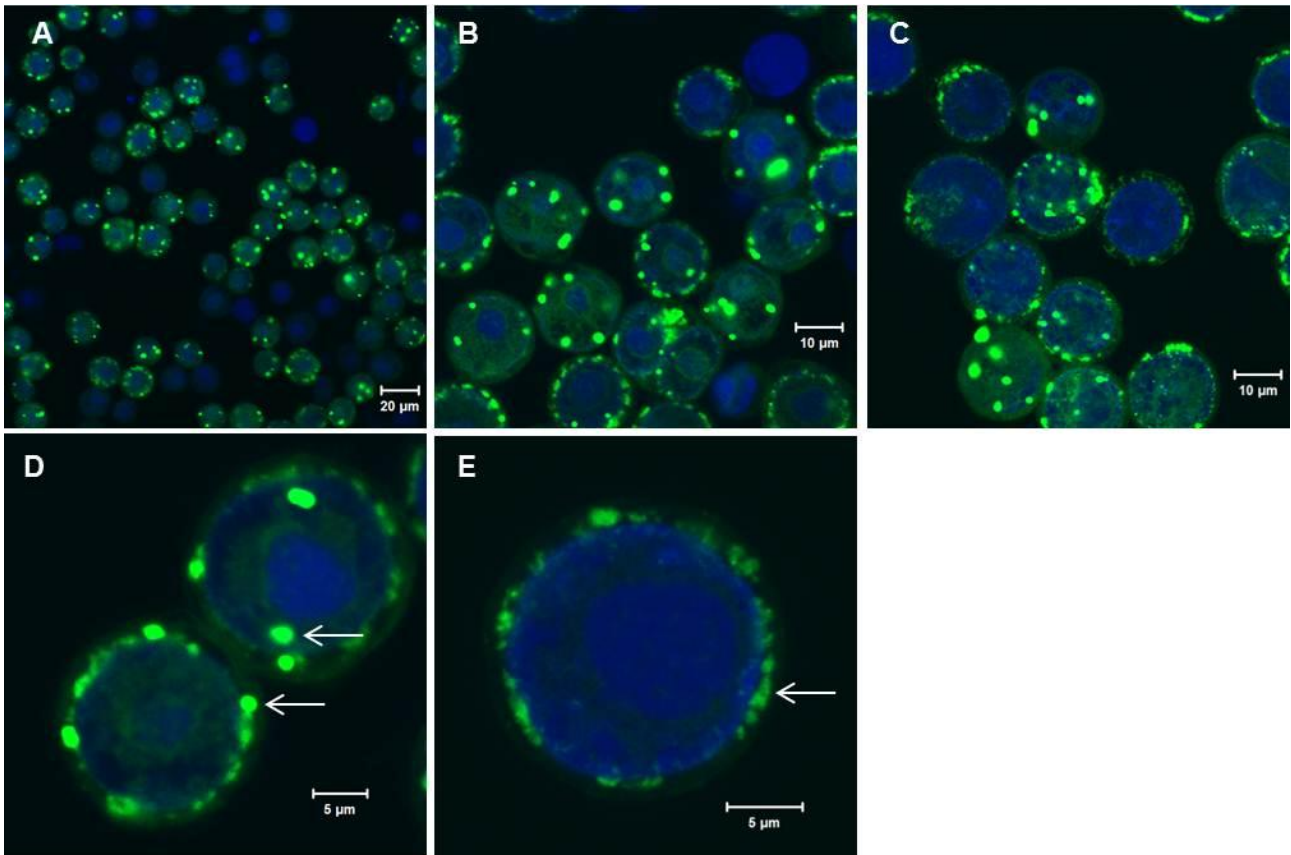
.

Fig. 40 Direct immunofluorescence images of Bac-VP7-177-eGFP infected Sf9 cells (48 hpi). A larger field of cells is seen in A, with cells viewed at a higher magnification seen in B and C. VP7-177-eGFP forms small foci of fluorescence in the cell (as indicated by the arrows in D) that appear to be composed of the smaller aggregates seen in E (as indicated by the arrow). Nuclear staining was done with DAPI (blue). Scale bars represent 20 µm (A), 10 µm (B, C) and 5 µm (D, E).
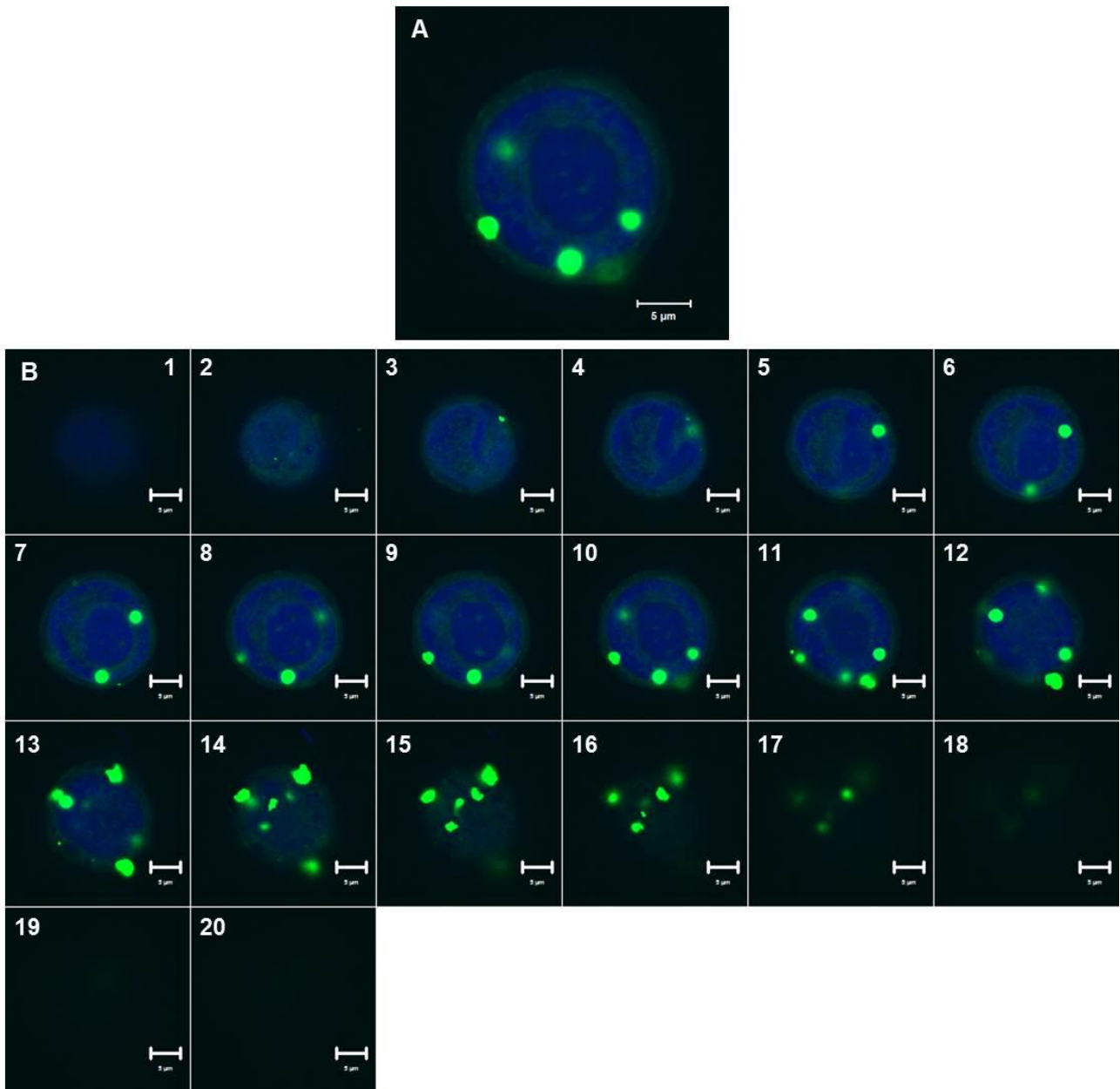
73

Fig. 41 Z-stack analysis of a Bac-VP7-177-eGFP infected Sf9 cell (48 hpi). The Z-stack gallery of images taken at 1 µm intervals through the cell is shown in B, and illustrates that multiple foci were present throughout this cell. Nuclear staining was done with DAPI (blue). Scale bars represent 5 µm.
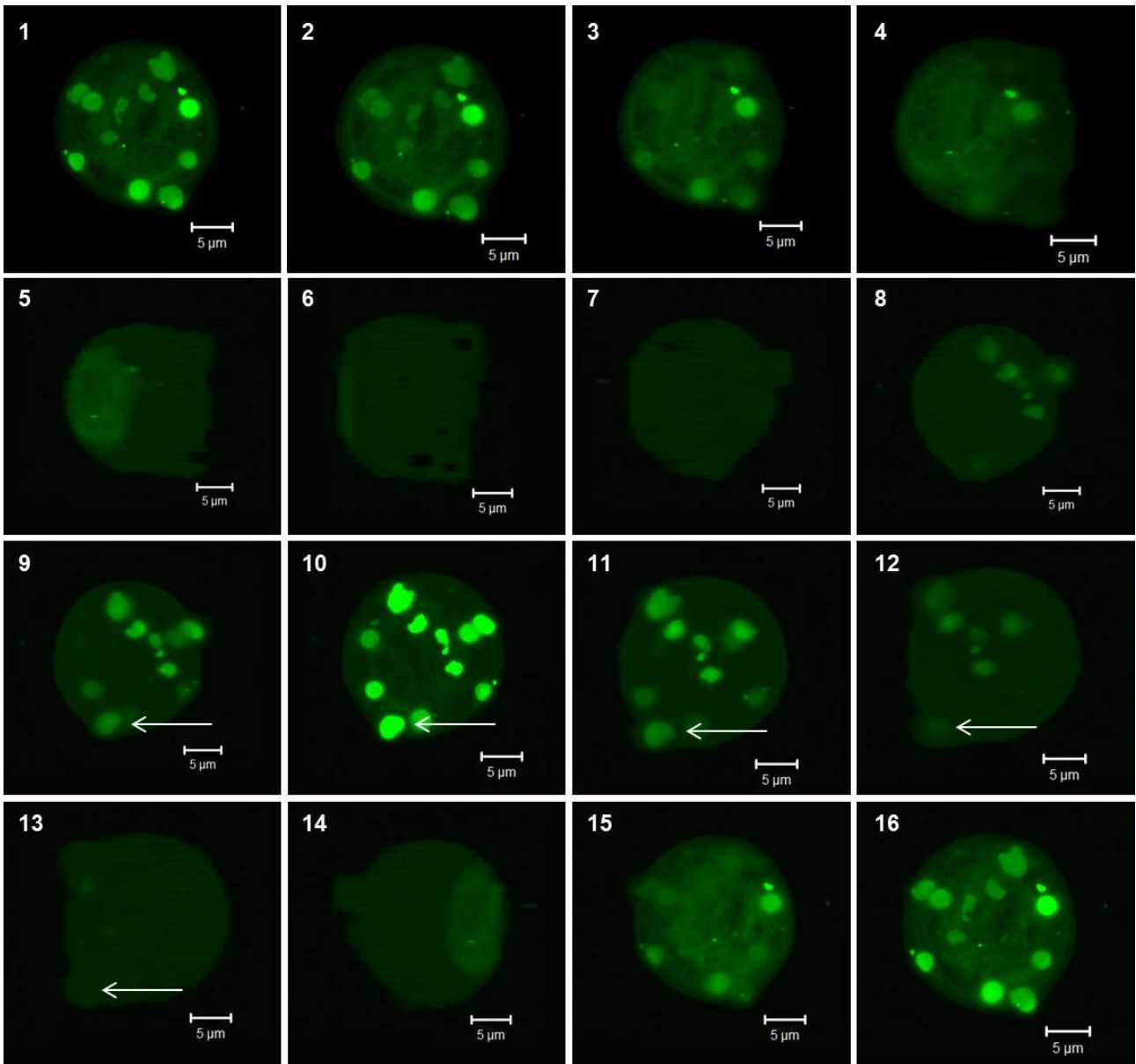
Fig. 42 Snapshots of a three-dimensional reconstruction of the Bac-VP7-177-eGFP infected Sf9 cell in Figure 9. The reconstruction was rotated around the Y-axis in a clockwise manner, with 90˚ rotation observed in Panel 7, 180˚ rotation observed in Panel 10, 270˚ rotation in Panel 13 and 360˚ rotation observed in Panel 16. As the cell rotates around the Y-axis one is able to see that the foci appear spherical in nature and cause the plasma membrane to distort slightly at the location thereof (as indicated by the arrows in Panels 9-13). Scale bars represent 5 µm.
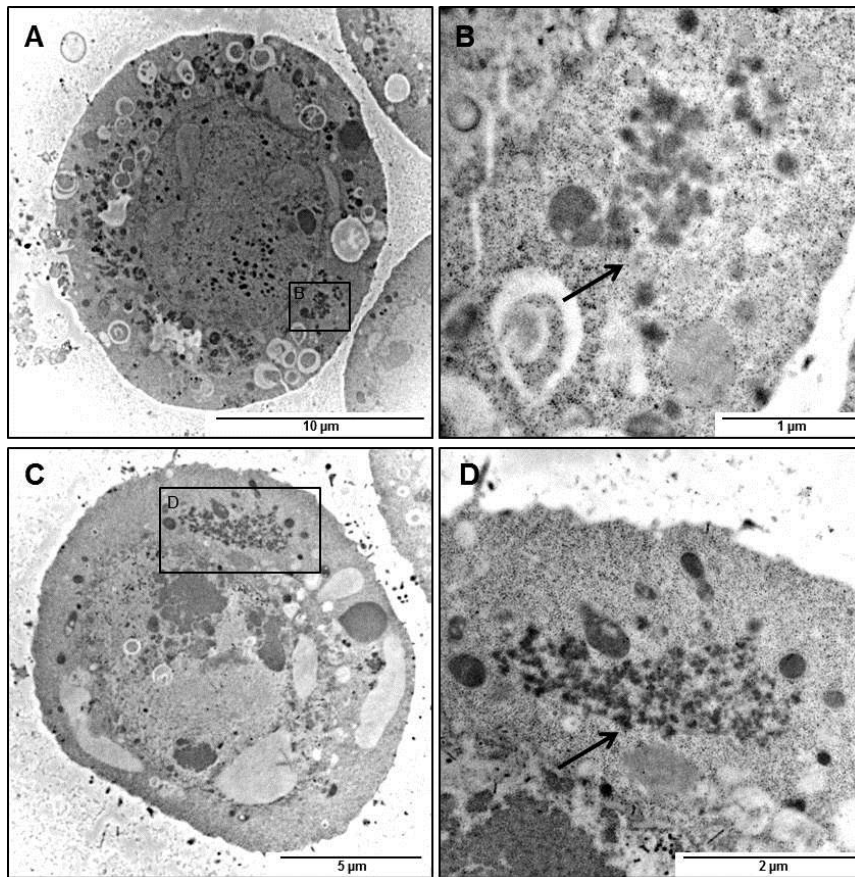
Fig. 43 TEM micrographs of Bac-VP7-177-eGFP infected Sf9 cells (48 hpi). Small protein aggregates were observed in the cytoplasm of the cell (A, B) and were shown to resemble those of VP7-144-eGFP at a higher magnification (B, D). Scale bars represent 10 µm (A), 1 µm (B), 5 µm (C) and 2 µm (D).

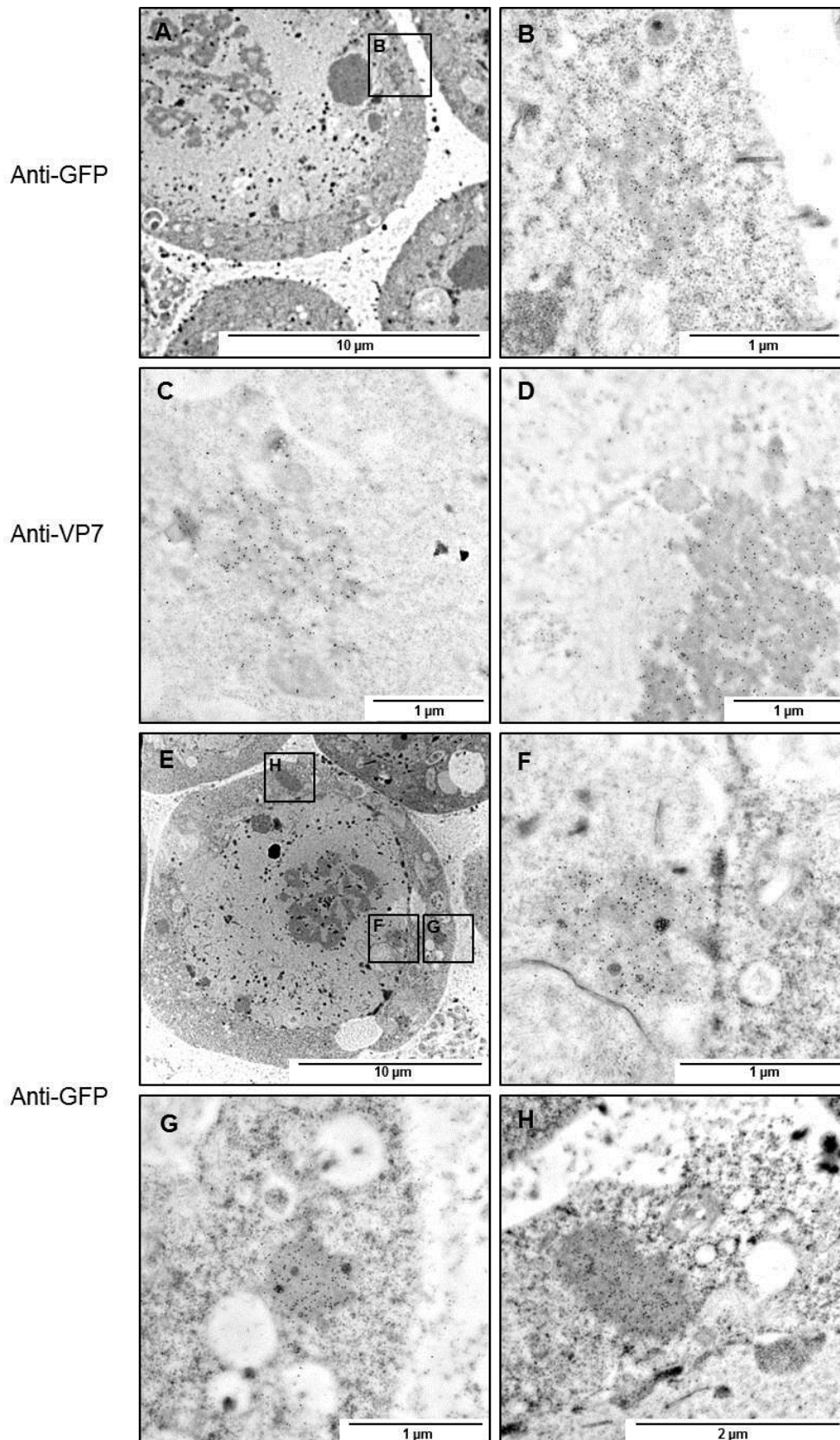Fig. 44 TEM micrographs VP7-177-eGFP immunogold labelled with anti-GFP or anti-VP7 primary and gold-conjugated secondary antibodies. The smaller protein aggregates resembling those observed in Bac-VP7-144-eGFP infected cells showed positive labelling (A, C, D, F). In addition to these aggregates, structures such as those seen in G and H also showed positive labelling. Scale bars represent 10 µm (A, E), 1 µm (B-G) and 2 µm (H).

77

VP7-200-eGFP

The last of the VP7-eGFP fusions was VP7-200-eGFP, the least soluble of the three. In order to view these structures on a cellular level, direct immunofluorescence was performed on Bac-VP7-200-eGFP infected Sf9 cells. Multiple small foci of fluorescence were observed in the cell (Fig. 45) and appeared to be composed of smaller loosely associated particles resembling those of VP7-144-eGFP and VP7-177-eGFP (Figs. 35 and 40).

In order to determine whether or not the foci were flat or spherical in nature Z-stack analyses were done on Bac-VP7-200-eGFP infected Sf9 cells. The Z-stack analysis and 3D reconstruction shown in Figures 46 and 47 confirmed that the foci formed by VP7-200-eGFP were flat in nature. These foci were flat disc-shaped particles that appeared rod-like from a 90° angle.

TEM showed that this protein accumulated to small aggregates similar to those observed in cells expressing VP7-144-eGFP (Fig. 48A-D). In addition to these aggregates, rod-shaped structures were also observed in the cell (Fig. 48E, F). This was the only VP7-eGFP construct that formed these rod-like structures. No rigid rod-like particles resembling those seen in Bac-VP7 infected cells were observed in Bac-VP7-200-eGFP infected cells. In addition to this, no rigid foci resembling those of VP7-144-eGFP were observed.

In order to determine whether or not these structures were in fact VP7-200-eGFP, immunogold labelling with anti-VP7 and anti-GFP was performed. Very specific positive labelling with both antibodies confirmed that both the smaller aggregates and the rod-like particles were indeed VP7-eGFP specific (Fig. 48B-F).
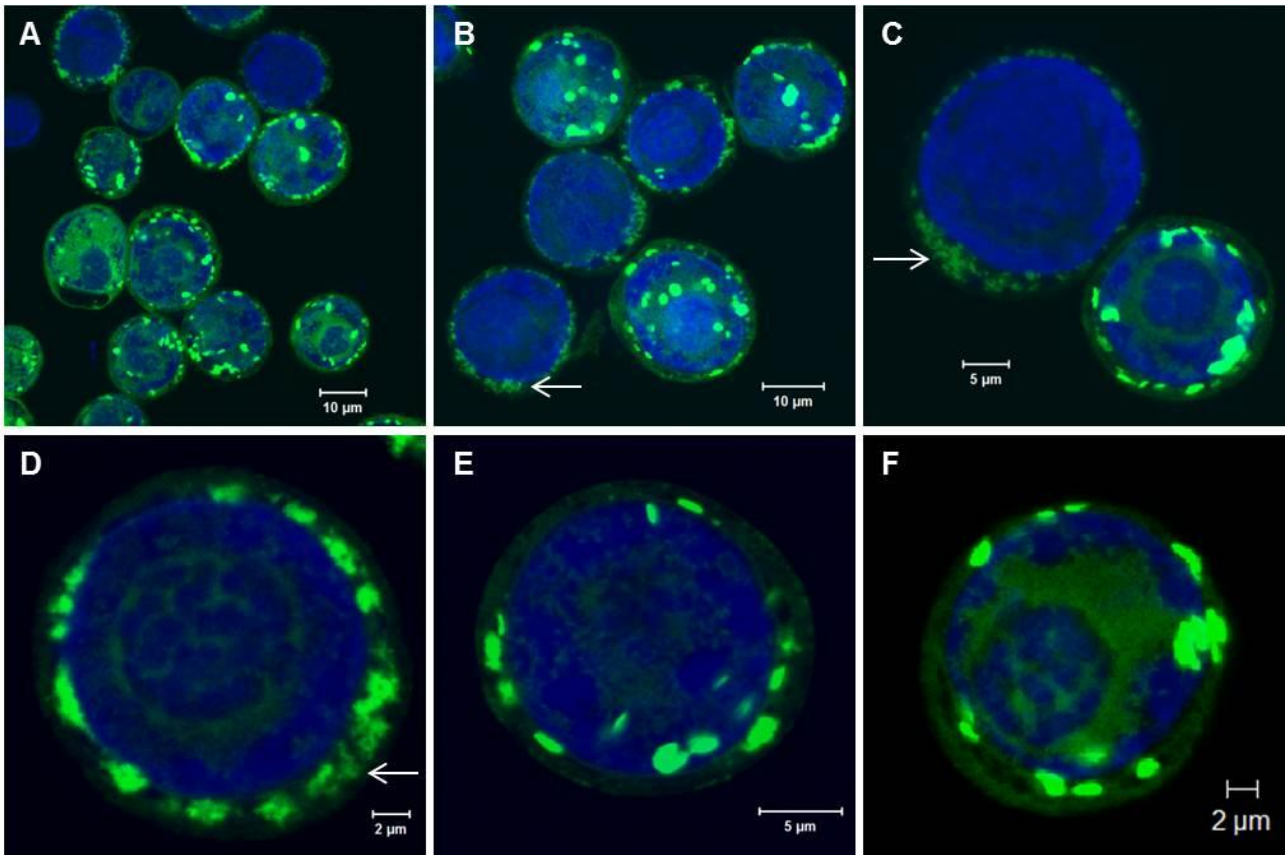
Fig. 45 Immunofluorescence images of Sf9 cells infected with Bac-VP7-200-eGFP (48 hpi). Larger fields of cells are seen in A and B. VP7-200-eGFP is visualised as small protein aggregates (arrows in B-D) that accumulate to multiple, scattered foci of fluorescence (E, F). Nuclear staining was done with DAPI (blue). Scale bars represent 10 μm (A, B), 5 μm (C, E) and 2 μm (D, F).

79

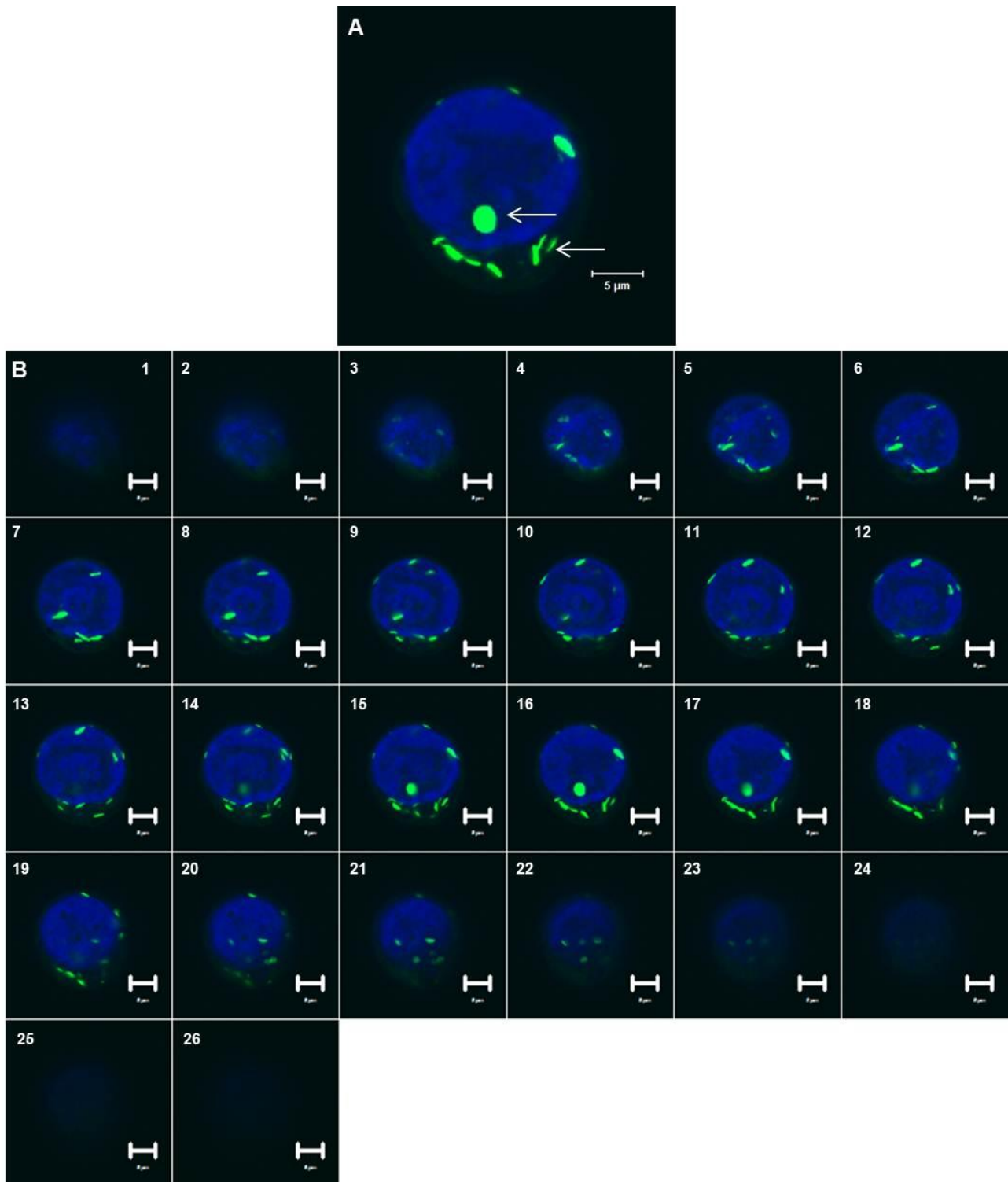Fig. 46 Z-stack analysis of a Bac-VP7-200-eGFP infected Sf9 cell (48 hpi, A). The Z-stack gallery of images taken at 0.5 µm intervals through the cell shown in B. Nuclear staining was done with DAPI. Arrows indicate that VP7-200-eGFP accumulates to form flat disc-shaped foci of fluorescence that may appear rod-like when visualised at a 90˚ angle. Nuclear staining was done with DAPI (blue). Scale bars represent 5 µm.

80
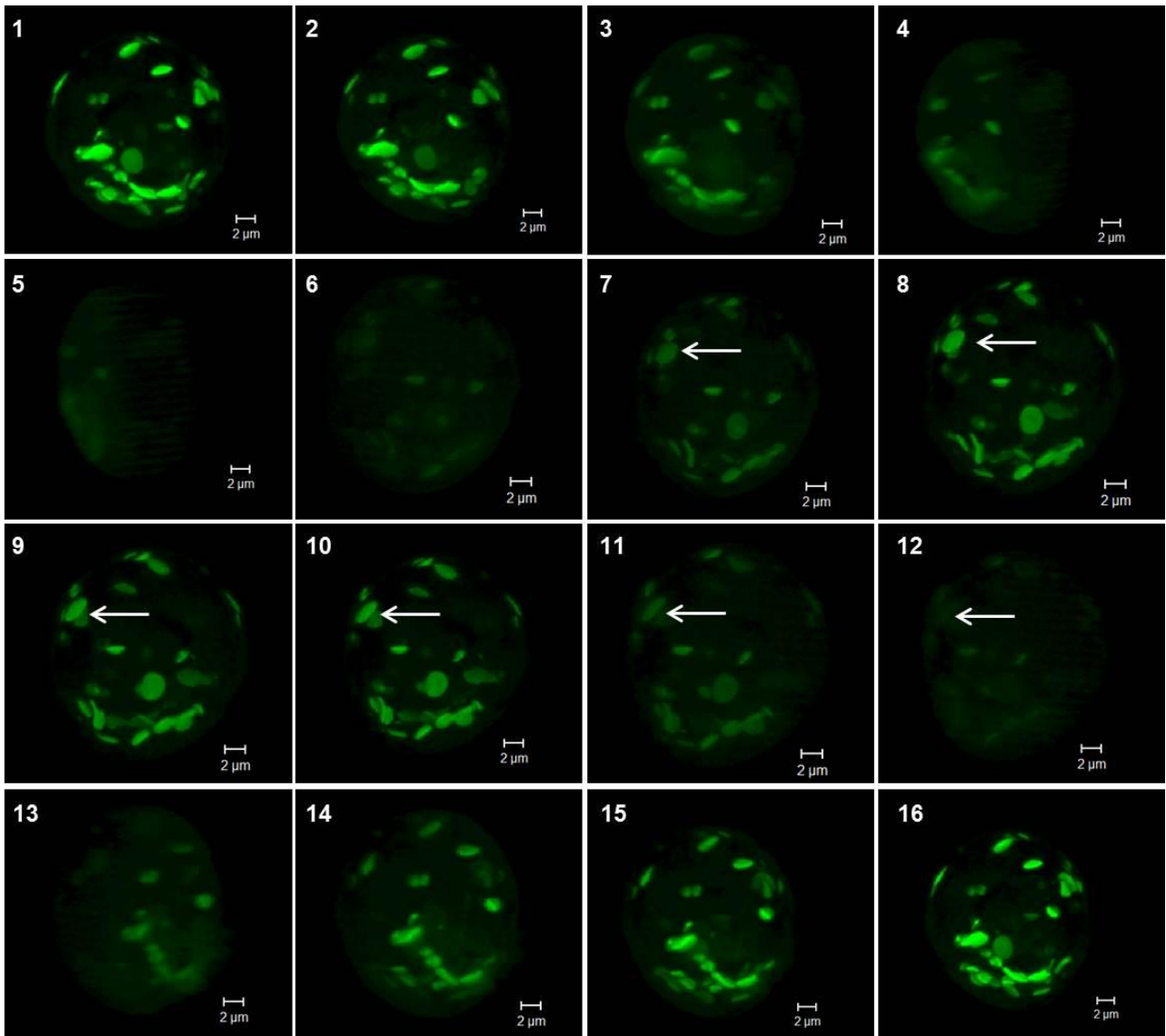
Fig. 47 Snapshots of a three-dimensional reconstruction of the Bac-VP7-200-eGFP infected Sf9 cell (48 hpi) in Figure 12. The reconstruction was rotated around the Y-axis in a clockwise manner, with 90˚ rotation having occurred between Panels 5 and 6, 180˚ rotation between Panels 9 and 10, 270˚ between Panels 12 and 13 and 360˚ rotation was observed in Panel 16. VP7-200-eGFP foci are flat, disc-shaped structures that appear somewhat rod-like from a 90˚ angle (see, for example, the focus indicated by the arrow). Scale bars represent 5 μm.
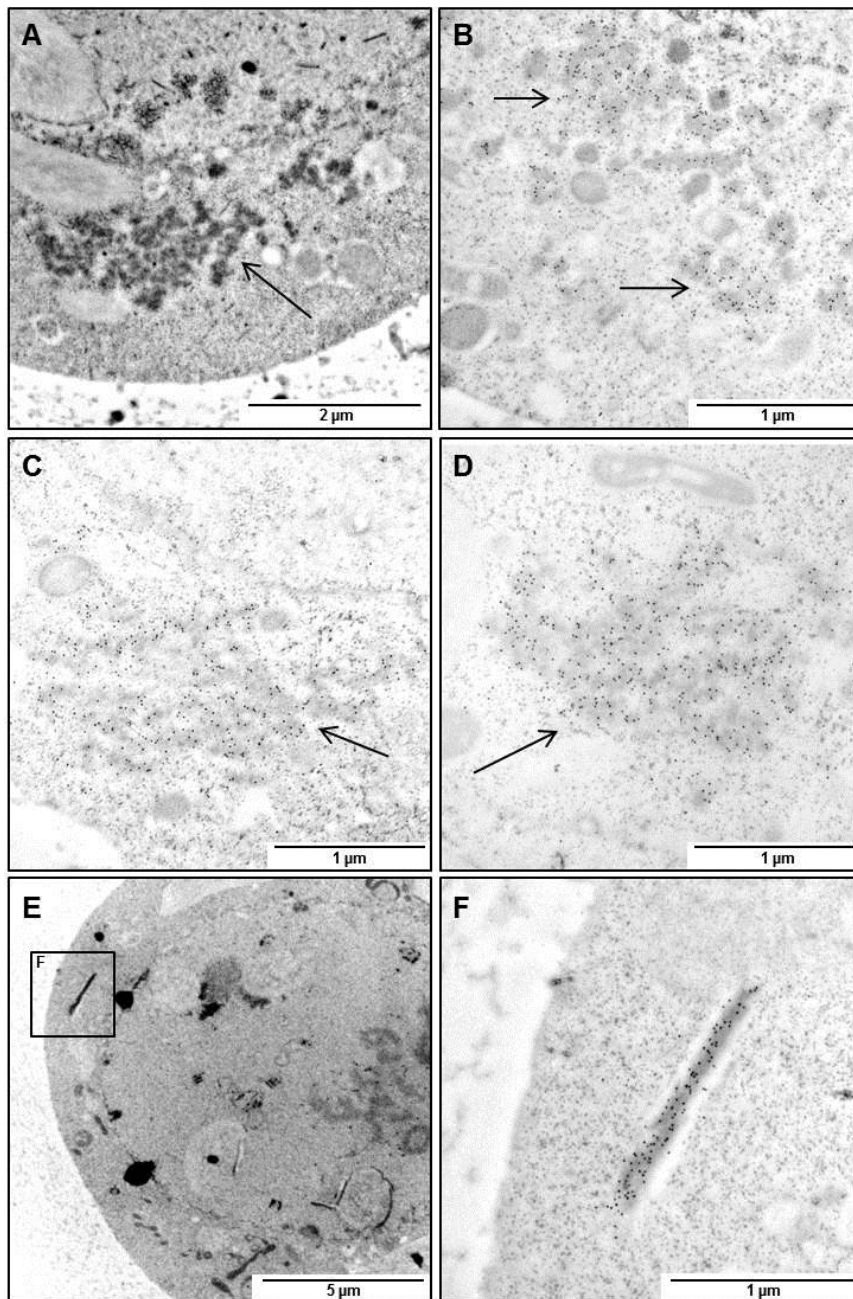
Fig. 48 TEM micrographs of Bac-VP7-200-eGFP infected Sf9 cells (48 hpi). VP7-200-eGFP forms small protein aggregates in the cell (A-D). In addition to these structures, VP7-200-eGFP also forms rod-like particles (E, F). VP7-200-eGFP was immunogold labelled with anti-VP7 (B) or anti-GFP (C-F) primary and gold-conjugated secondary antibodies. Scale bars represent 2 µm (A), 1 µm (B, C, D, F) and 5 µm (E).

Summary
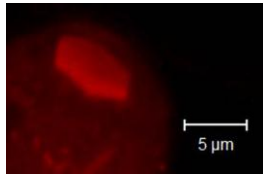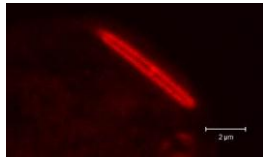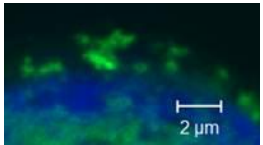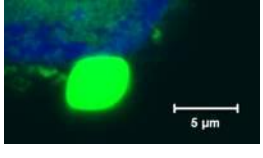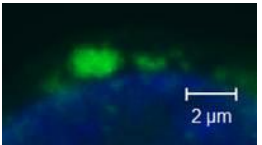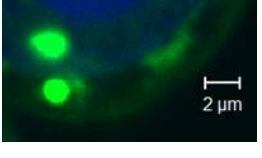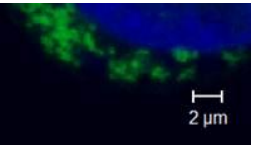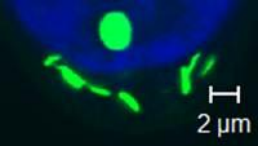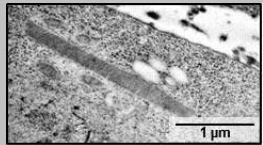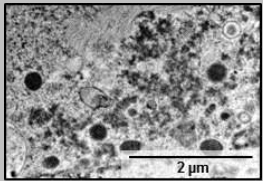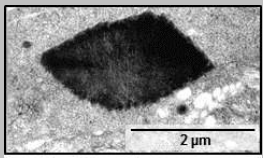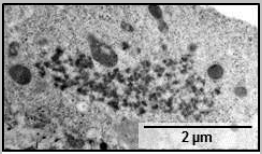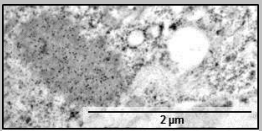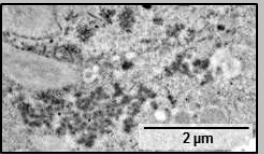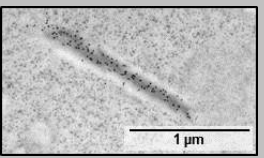
Table 6 summarises the differences between WT AHSV VP7 and the VP7-eGFP mutants. The findings pertaining to WT AHSV VP7 were also stated in Table 5 of Section 2.3.2 and previous findings by Rutkowska *et al.* (2011) and Rutkowska (2012) were included to aid in the comparison of WT VP7 and the VP7-eGFP fusion proteins. VP7-144-eGFP formed large, irregularly shaped structures that appeared to be composed of smaller protein aggregates accumulating over the course of the infection cycle. The large, electron dense structures formed by VP7-144-eGFP were

82

visualised as large foci of fluorescence under the confocal microscope and smaller aggregates were also observed in infected cells.

Smaller aggregates resembling those of VP7-144-eGFP were also observed for both VP7-177-eGFP and VP7-200-eGFP. TEM showed that in addition to the smaller aggregates, VP7-177-eGFP also formed multiple small, irregular foci in the cell. Confocal microscopy showed that these foci were spherical in nature.

VP7-200-eGFP formed multiple flat, disc-shaped foci in infected cells. In contrast to VP7-144-eGFP and VP7-177-eGFP, VP7-200-eGFP also gave rise to rod-like particles in infected cells. These rod-like particles were determined to be the disc-shaped foci visualised at a 90˚ angle.

83

Table 6 Summary of the differences between WT VP7 and the VP7-eGFP fusions

	WT VP7	VP7-144-eGFP	VP7-177-eGFP	VP7-200-eGFP
Solubility (%)	<10 (Rutkowska *et al.* 2011)	~35 (Rutkowska 2012)	~19.5 (Rutkowska 2012)	~22 (Rutkowska 2012)
Able to form trimers?	Yes (Rutkowska *et al.* 2011)	Yes (Rutkowska 2012)	Yes (Rutkowska 2012)	Yes some, but largely monomeric (Rutkowska 2012)
SEM	Hexagonal	?	?	?
Confocal	Hexagonal Rod-like	Small aggregates Large focus	Small aggregates Multiple small round foci	Small aggregates Multiple small disc-/rod-shaped foci
TEM	Rod-like	Small aggregates Large focus	Small aggregates Small focus	Small aggregates Rod-like (occasionally)
Terminology	Flat hexagonal or rod-like crystalline-like particles.	Small aggregates associate to form large foci of strong fluorescence.	Small aggregates associate to form small, round foci of fluorescence.	Small aggregates associate to form small, disc-shaped foci of fluorescence that appear rod-like when visualised at a 90˚ angle.

Taken together the results of this section indicate that the VP7-eGFP proteins all still localised to one or multiple distinct positions in the cell. They differed however with respect the nature of the protein aggregates or particles formed by the proteins at the points of self-assembly.

2.3.3.3 Fate of misfolded VP7-eGFP proteins

As shown in Section 2.3.3.1, a significant portion of expressed VP7-eGFP protein is correctly folded, fluorescing protein with the remaining portion being composed of non-fluorescing, misfolded protein. Little is known about the fate of this misfolded protein and prompted an investigation into the fate thereof using an immunofluorescence and confocal microscopy approach. Sf9 cells were infected with recombinant baculoviruses expressing VP7-144-eGFP, VP7-177-eGFP or VP7-200-eGFP and at 48 hpi were prepared for immunofluorescence and confocal microscopy using the available primary antibodies (anti-VP7 and anti-VP7-eGFP) in conjunction with a TRITC-conjugated secondary antibody. These primary antibodies were polyclonal thereby prompting a comparison between the above-mentioned antibodies with a commercially available antibody that was GFP specific (in conjunction with an AlexaFluor secondary antibody). It was postulated that correctly folded fusions would be detected by both green auto-fluorescence and a red signal from antibody labelling, whereas misfolded proteins would be detected by a red signal in the absence of green auto-fluorescence. WT-Bac infected and uninfected (mock infected) cells were used as controls in all cases and all available antibodies were used for comparative purposes.

Figure 49 shows the results of the immunofluorescence analysis of VP7-144-eGFP with all of the available primary antibodies. In each case the first panel represented green auto-fluorescence, with the localisation pattern and nature of the protein corresponding to what was observed in the previous section (Fig. 35). The second panel (Fig. 49) indicated primary antibody recognition (red). In all cases there appeared to be a red signal at the same locations as that of green auto-fluorescence. This indicated that correctly folded, fluorescing fusions were being detected by the primary antibodies. The signal of the primary antibodies differed in some instances, and at times differed slightly between experiments. Immunofluorescence with the commercial antibody led to higher signals in the cytoplasm of the cell (Fig. 49F). In addition to this, the level of antibody labelling obtained for the foci of fluorescence also differed between antibodies, with the signal in Figure 49C (anti-VP7) being stronger than that observed in Figures 49E (anti-VP7-eGFP) and 49F (anti-GFP). Sometimes a "halo" was observed around large foci (Fig. 49E), as though antibodies could not penetrate the aggregate and only labelled the surface/perimeter. The differences in antibody labelling observed here could reflect the accessibility of the specific epitopes in the aggregate to antibodies in the serum.

The merged images in Figure 49 indicated that in all cases green auto-fluorescence and red antibody recognition colocalised at the same points in the cell. Furthermore, no significant levels of red signal that was consistently present in specific regions was obtained in the absence of green auto-fluorescence, thus no misfolded fusions were differentially detected.

VP7-177-eGFP and VP7-200-eGFP were analysed in a similar manner and showed a similar pattern of primary antibody recognition as that observed for VP7-144-eGFP (Figs. 50 and 51). In the case of both VP7-177-eGFP and VP7-200-eGFP stronger labelling than that observed for VP7-144-eGFP was obtained for the foci of fluorescence. The signal for antibody labelling was stronger still in the case of VP7-200-eGFP foci (Fig. 51). This could be due to the size of the aggregates or the nature of packaging of the various fusion proteins.
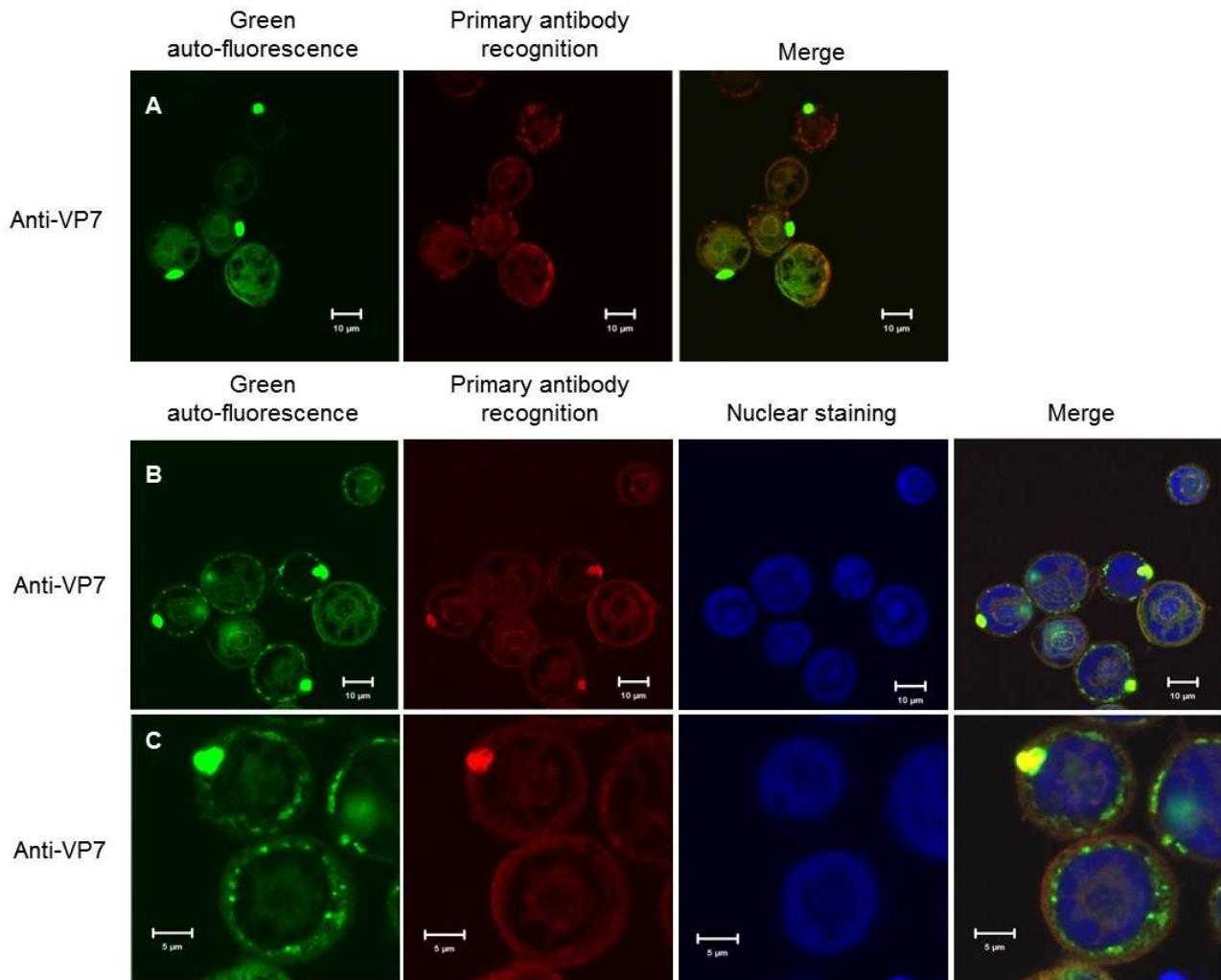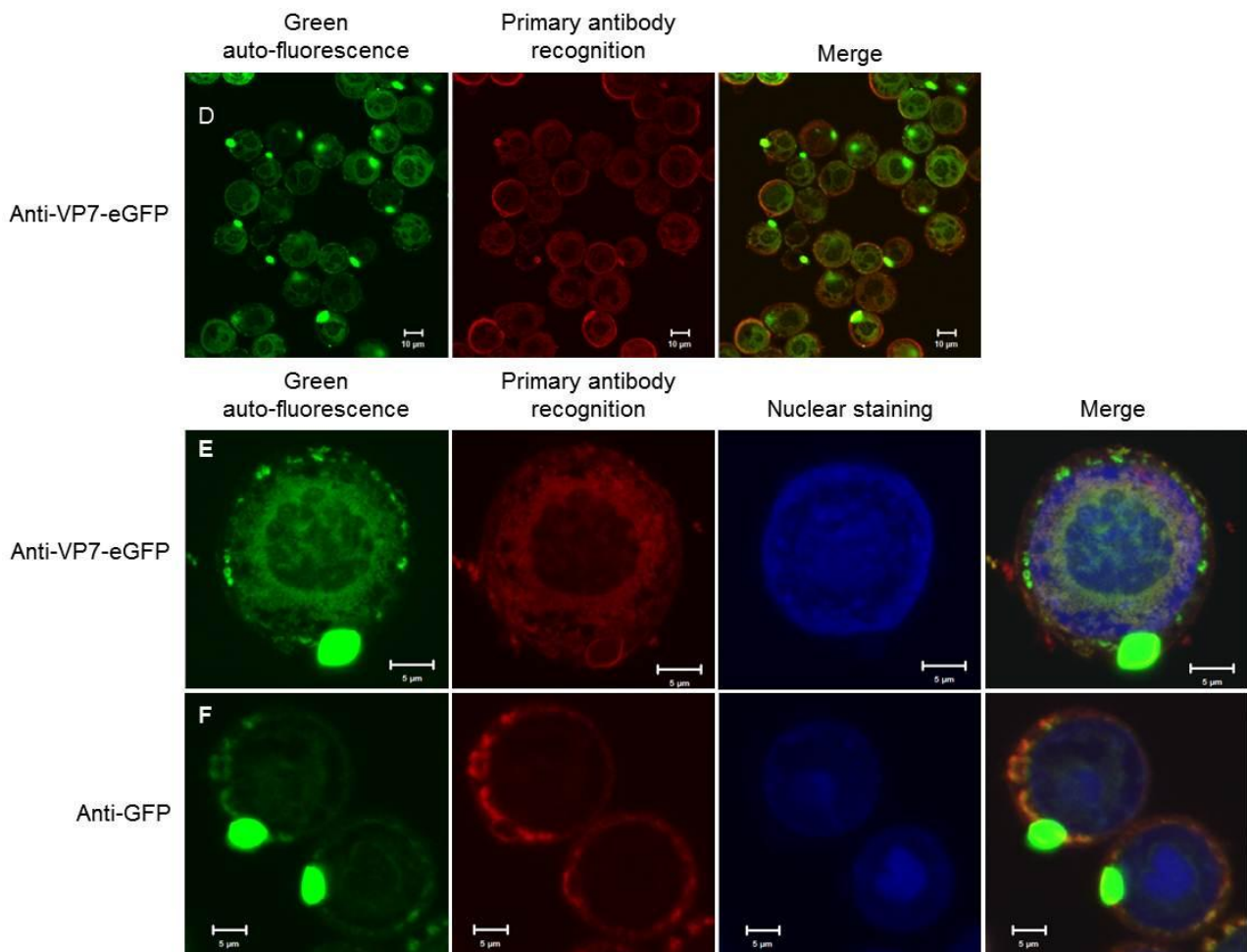
Fig. 49 Immunofluorescence images of Sf9 cells infected with Bac-VP7-144-eGFP (48 hpi). The primary antibodies used were anti-VP7 (A-C) or anti-VP7-eGFP (D, E) in conjunction with a TRITC-conjugated secondary antibody. In the case of F, the commercially available anti-GFP was used in conjunction with an AlexaFluor secondary antibody. In all cases the first panel represents green auto-fluorescence and the second panel represents primary antibody recognition. The last panels represent the merged image, whereas the third panel in B, C, E and F represent nuclear staining with DAPI (blue). Scale bars represent 10 μm (A, B) and 5 μm (C).

In order to substantiate the results obtained via visual estimation of the above immunofluorescence images, colocalisation analysis was done using Image J software (2.2.11). Manders' coefficient was calculated in each case as it is a good indication of the colocalisation in a given field (Bolte and Cordelieres 2006). This value varies from 0 to 1, with the latter representing 100% colocalisation. The image in Figure 49A has a Manders' coefficient of 0.851, and is representative of the colocalisation seen in this study. Thus, although true colocalisation was not observed, a high level of colocalisation was observed in this study, with a Manders' coefficient above 0.9 often observed.

87
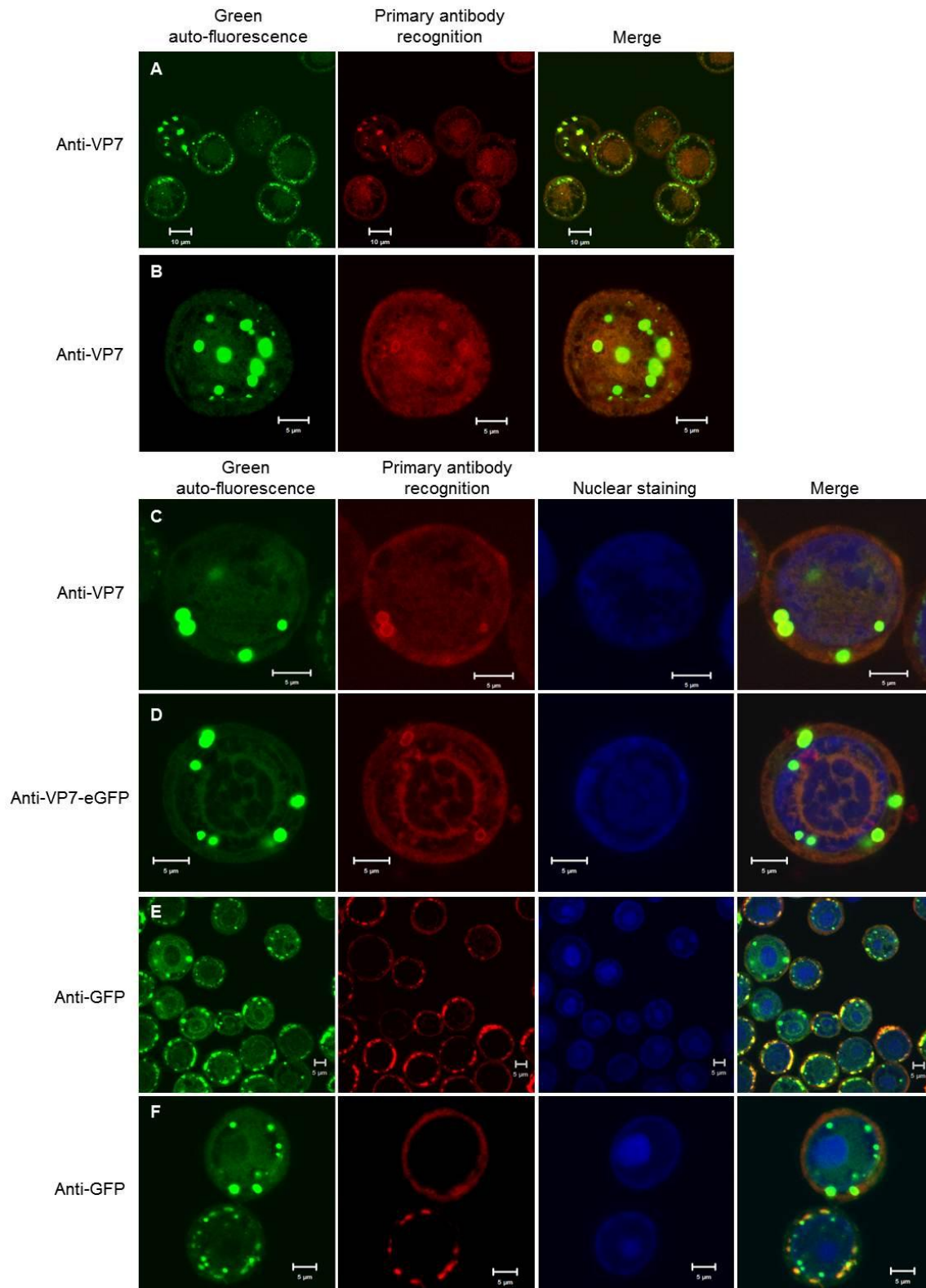
Fig. 50 Immunofluorescence images of Sf9 cells infected with Bac-VP7-177-eGFP (48 hpi). The primary antibodies used were anti-VP7 (A-C) or anti-VP7-eGFP (D) in conjunction with a TRITC-conjugated secondary antibody. In the case of E and F, the commercially available anti-GFP was used in conjunction with an AlexaFluor secondary antibody. In all cases the first panel represents green auto-fluorescence and the second panel represents primary antibody recognition. The last panels represent the merged image, whereas the third panel in C-F represent nuclear staining with DAPI (blue). Scale bars represent 10 µm (A) and 5 µm (B-F).

88
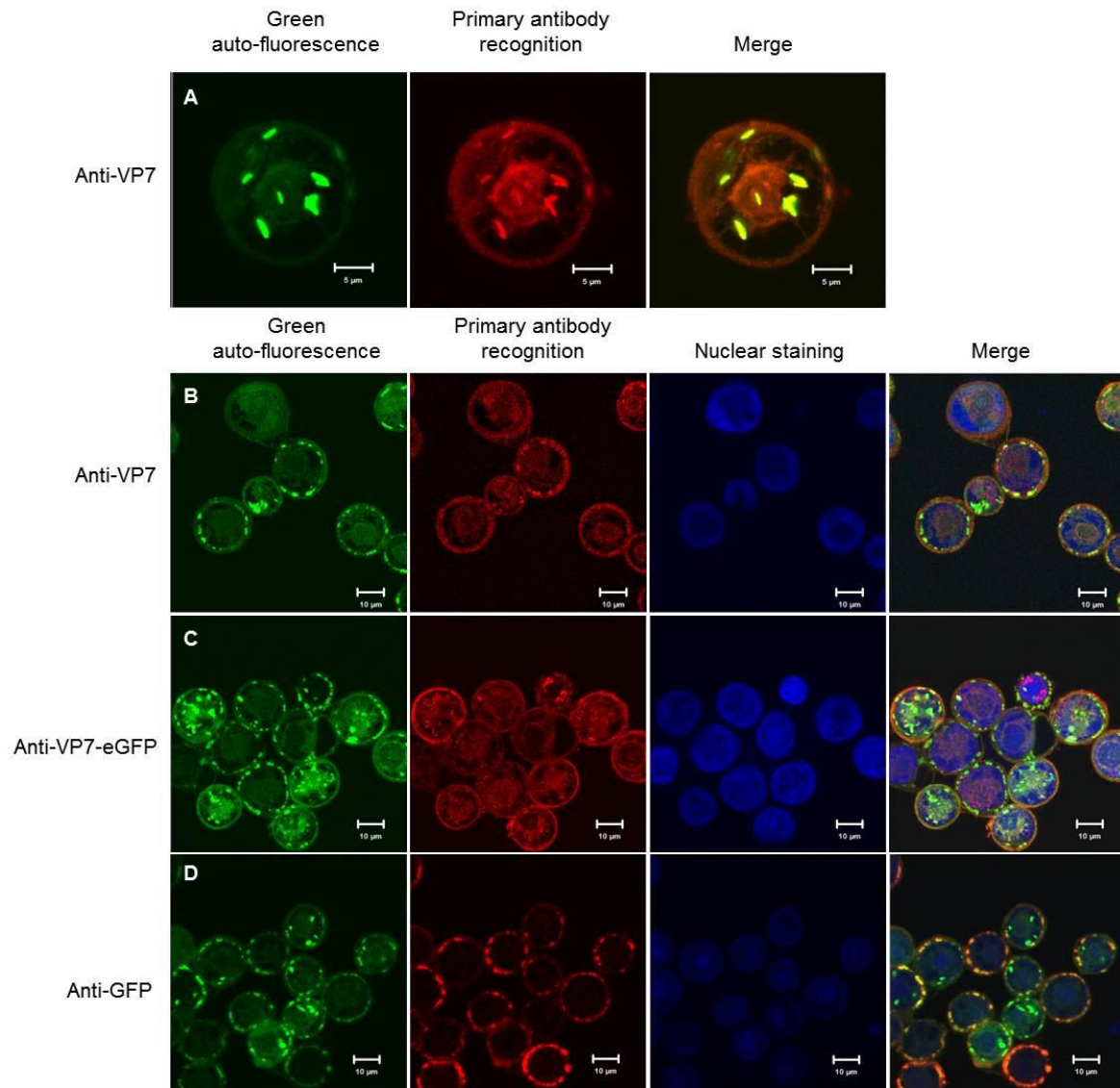
Fig. 51 Immunofluorescence images of Sf9 cells infected with Bac-VP7-200-eGFP (48 hpi). The primary antibodies used were anti-VP7 (A, B) or anti-VP7-eGFP (C) in conjunction with a TRITC-conjugated secondary antibody. In the case of D, the commercially available anti-GFP was used in conjunction with an AlexaFluor secondary antibody. In all cases the first panel represents green auto-fluorescence and the second panel represents primary antibody recognition. The last panels represent the merged image, whereas the third panel in B-D represent nuclear staining with DAPI (blue). Scale bars represent 5 μm (A) and 10 μm (B-D).

The above results indicated that proteins were not differentially detected for any of the VP7-eGFP fusions. This was true for all available antibodies, and may indicate that the misfolded proteins may localise to the same positions as the correctly folded proteins or that the method used here may not be effective in the detection thereof.

2.4 Discussion and Concluding Remarks

Although AHSV VP7 is very similar to its BTV counterpart, there is one main distinguishing factor – BTV VP7 is a largely soluble protein whereas AHSV VP7 is highly hydrophobic and insoluble and self-assembles into flat, hexagonal crystalline particles – the significance of which has yet to be established. Furthermore, little is known about the process underlying the assembly and formation of these AHSV VP7 particles. The main aim of this study was therefore to investigate the formation of these VP7 particles and to assess how the assembly thereof is affected by various modifications to the VP7 top domain. As part of this investigation, previously constructed AHSV VP7 mutants were compared to WT AHSV VP7 using a dual microscopy approach. Factors influencing VP7-eGFP aggregation were also investigated and the fate of misfolded VP7-eGFP fusion proteins was investigated by comparing the localisation of fluorescing and non-fluorescing versions of each protein by means of confocal microscopy.

The hexagonal particles formed by AHSV VP7 are composed of trimer-trimer sheets stacked tightly one on top of the other to form a rigid structure (Burroughs *et al.* 1994; Venter *et al.* 2014). A recent study has shown that initially, AHSV VP7 is distributed homogenously throughout the cytoplasm of both mammalian and insect cells (Bekker *et al.* 2014). Over time, the distribution becomes less homogenous as the protein localises to multiple foci throughout the cytoplasm, decreasing in number and increasing in size, eventually aggregating at one, or more, site(s) forming the characteristic large crystalline-like particle (Bekker *et al.* 2014). The diffuse distribution observed at the initial stages of the infection cycle indicates that VP7 is expressed in a soluble form, after which it coalesces to form an insoluble particle. The intracellular distribution and trafficking of AHSV VP7 to the site(s) of particle formation is not cell-type dependent, nor is it dependent on the presence or absence of other viral proteins (Bekker *et al.* 2014). Furthermore, the authors have shown that AHSV VP7 evades host cell transport mechanisms such as the microtubule network, as well as defence mechanisms such as the ubiquitin-proteasome system or the aggresomal and lysosomal pathways. It was suggested that particle formation is driven by self-assembly of trimer-trimer interactions as described by Limn and Roy (2003), with Bekker *et al.* (2014) suggesting that this could drive the formation of the small foci and their subsequent coalescence into crystalline-like particles.

This study is focussed on the stacking of the VP7 layers to form these particles, and how this stacking is affected by various top domain modifications. A range of AHSV VP7 mutants were available for use. These included the vector proteins VP7-144, VP7-177 and VP7-200, in which small peptides (6 aa) were inserted downstream of sites 144, 177 and 200 of the top domain, as well as VP7 proteins containing major top domain modifications such as the VP7-eGFP fusion proteins VP7-144-eGFP, VP7-177-eGFP, VP7-200-eGFP. In the case of VP7-144 and VP7-177 the peptide insertions at sites 144 and 177 of the top domain caused VP7 to be a more soluble

90

protein, especially so in the case of VP7-144 (Rutkowska *et al.* 2011). However, for VP7-200 the insertion of the small peptide into site 200 did not affect the solubility of the protein, yielding a protein almost as insoluble as WT VP7. Although all three proteins formed trimers, it was shown that the insertion at site 200 affected the trimer stability (Rutkowska *et al.* 2011). The likely reason for this is that in the case of VP7-200 the three 200 insertion sites are all located in close proximity in the trimer top domain. Any insert at this site will therefore have to compete for space, which in turn could result in trimer instability.

For this study the protein expression by the available baculovirus recombinants was confirmed, and the necessary controls for both confocal and transmission electron microscopy developed. This was followed by an investigation into the self-assembly and particle formation of WT AHSV VP7, which then formed the basis for the subsequent comparison with the various VP7 mutants.

When investigating WT AHSV VP7, confocal microscopy showed that VP7 accumulates at multiple sites in the cell, eventually forming rigid structures located mainly in the cytoplasm but also occasionally in the nucleus. These structures were visualised as flat, hexagonal or rod-like particles. Primary antibody recognition of the outer surface epitopes led to the difference in appearance of hexagonal versus rod-like particles, with the latter showing labelling on the outer edge of the rods, depending on where in the particle the slice was made. Z-stack analysis and rotation of the resulting 3D reconstructions however showed that the flat, hexagonal structures appear rod-like when viewed at a 90˚ angle to the original structure, indicating that the observation of one structure as opposed to the other is dependent on the focal plane and orientation of the cell, rather than the two structures representing two independent forms of the protein complex. Similar analyses of single cells under the confocal indicated that even though a single plane through a cell suggests the presence of only one particle in the cell, more particles may be present. At times, as many as three particles were observed.

Ultrastructural analyses of WT AHSV VP7 under the TEM showed the presence of rigid, rod-like particles in the cytoplasm of Sf9 cells that could be positively labelled with anti-VP7 antibodies. No hexagonal particles were viewed under the TEM. This is not surprising, as TEM is performed on ultrathin sections through a cell. Thus it is more likely for a diagonal section through a hexagonal particle to occur, leading to the observation of rod-like particles differing in length depending on where in the particle the section is made.

The WT VP7 particles observed here correspond to the rod-like particles observed under the TEM in AHSV-infected mammalian and insect cells (Breese *et al.* 1969; Venter *et al.* 2012; Venter *et al.* 2014) as well as to those observed when expressed in insect cells by means of a recombinant baculovirus (Chuma *et al.* 1992). Furthermore, these particles correspond to the hexagonal

particles purified from AHSV-infected mammalian cells (Burroughs *et al.* 1994) and those purified from baculovirus infected insect cells and viewed under the SEM (Rutkowska *et al.* 2011). Both the rod-like and the hexagonal particles also resemble those observed more recently under the confocal for both AHSV-infected mammalian cells and Sf9 cells expressing WT VP7 by means of a recombinant baculovirus expression system (Bekker *et al.* 2014).

In addition to forming the basis of comparison with the vector proteins, the analysis of WT AHSV VP7 also showed the value of using a dual microscopic approach to investigate a common aim. Confocal microscopy allowed AHSV VP7 self-assembly and particle formation to be investigated on a cellular level, and was particularly useful in that Z-stack analyses could be used to render 3D reconstructions of a cell/field of cells.   TEM allowed for a more in-depth analysis on an ultrastructural level. The use of both of these microscopic techniques in the same study has been successful in a wide range of other studies (Johnston *et al.* 1998; Garcia-Mata *et al.* 1999; Kar *et al.* 2007) including a recent investigation on the use of *Drosophila melanogaster* as a model organism for BTV replication and tropism (Shaw *et al.* 2012).

The results generated for WT VP7 were then compared to the VP7-144, VP7-177 and VP7-200 vector proteins (containing minor top domain modifications) to determine how these modifications affected the formation of the VP7 particles, in particular - the stacking of VP7 layers to form the rigid particles. This was addressed using the dual microscopy approach described above, with the appropriate anti-VP7 antibodies. Similar to what was observed for WT VP7, all three vector proteins self-assembled to one, or multiple, site(s) in the cell, indicating that the modifications had no effect on the ability of VP7 to self-assemble. However, these modifications did seem to affect the nature of the VP7 particle formed, as the protein structures formed by all three proteins differed from the hexagonal particles characteristic of AHSV VP7.

Confocal microscopy showed that although VP7-144 self-assembled to one, or multiple, site(s) in the cell, it formed structures that were quite unlike the particles formed by WT VP7. Instead, VP7-144 formed long and tapered structures (herein referred to as spindle-like structures) that were shown by Z-stack analysis to layer one on top of the other resulting in the formation of larger, somewhat star-shaped spindle aggregates. Perhaps due to the nature of the structures it was difficult to determine what these structures looked like from a 90˚ angle. TEM circumvented this problem and indicated the presence of both long, fibrous structures as well as smaller, loosely associated foci-like structures within Bac-VP7-144 infected Sf9 cells. Both structures were positively labelled with anti-VP7 and were often present within the same cell, indicating that the smaller foci-like structures represent a cross-sectional view through spindle-aggregates.

In contrast to VP7-144, confocal microscopy showed the presence of rosette-like structures in both Bac-VP7-177 and Bac-VP7-200 infected insect cells, with Z-stack analyses showing that these structures were fragmented in nature. Thus the stable layering of the sheets was affected in both cases, leading to these rosette-like structures in the cell. Furthermore, multiple Z-stack analyses and 3D reconstructions showed that the rosette-like particles appear somewhat hexagonal from above, consistent with previous SEM results (Kretzmann 2006; Rutkowska *et al.* 2011). TEM showed that you do get WT VP7-like particle formation in the case of the VP7-177 and VP7-200 vector proteins. The layers formed by VP7-177 were however, thicker (219 nm) on average than those formed by VP7-200 (101 nm). Instead of being stacked tightly together as in the case of WT VP7, the layers appeared to lift, causing the rosette-like appearance observed here.

The confocal and TEM results described above show that these minor top domain modifications do not affect the process of self-assembly, but they do affect how stably the layers stack one upon the other. Previous studies on rotavirus VP6 have shown that the charge of one residue in the trimer is enough to affect particle formation (Lepault *et al.* 2001). Perhaps this is also true for this study. Thus the nature of the insert, the charge of the insert as well as the site of the insert can all affect the eventual morphology of the VP7 particle. An important consideration here is the position of the three insertion sites within the trimer, and their proximity to one another. Both the three 144 sites and the three 177 sites are located far apart on the outer perimeter of the trimer, whereas the three 200 sites are clustered in close proximity to one another in the top centre of the trimer (Rutkowska *et al.* 2011). Thus, peptides inserted into site 200 are more likely to suffer from space constraints than are those inserted into site 144 or 177. It is possible that introduction of the 6 amino acid peptides may be so significant that VP7 layers are no longer able to stack on top of one another in an effective manner, leading to relatively thin, loosely associated layers and rosette-like structures but no stable particles. Sucrose gradient sedimentation analyses conducted at late stages of the infection cycle previously showed that a portion of the expressed VP7-144 protein in the particulate fractions can be reversed to a soluble form by treatment with L-arginine (Rutkowska *et al.* 2011), an observation not seen for VP7-177 or VP7-200. Thus, due to their loose association, it is possible that the structures formed by VP7-144 may be a visual representation of the reversibly aggregated protein.

The same 6 amino acid (KLRSVD) peptide was inserted into positions 177 and 200, thus the differences in particle formation between these two constructs were probably not insert specific. Also, although the insertions led to differences in solubility, VP7-200 was still almost as insoluble as WT VP7 (Rutkowska *et al.* 2011). Thus rather than solubility, it appears that in the case of VP7-200, the site of the insertion plays the biggest role in particle morphology. The added peptide in the middle of the trimer affects trimer stability, and appears to hamper particle formation by disrupting top-to-bottom layering of VP7-200 trimer sheets. More effective top-to-bottom trimer layering was

93

observed for VP7-177, indicating that this may be due to the location of the insertion sites, which in this case are on the sides of the trimer.

The next section of this study involved the use of VP7-eGFP fusion proteins (i.e. containing major top domain modifications) that were available at the beginning of this study. These proteins had been constructed by inserting eGFP into sites 144, 177 and 200 of the VP7 top domain. Previous sucrose gradient sedimentation analyses had indicated that both VP7-177-eGFP and VP7-144-eGFP sedimented exclusively as trimers, whereas VP7-200-eGFP was largely monomeric but with some trimeric portion (Rutkowska 2012). Sedimentation analyses done at late stages of the baculovirus infection cycle showed that a proportion of all three VP7-eGFP proteins co-sedimented with the particulate or aggregated fractions (Mizrachi 2008; Rutkowska 2012). Preliminary data suggested that this represented correctly folded, fluorescing VP7-eGFP trimers that were either loosely aggregated, or trapped in the excess of misfolded, non-fluorescing VP7-eGFP protein. Treatment of VP7-144-eGFP with L-arginine resulted in an increase in the amount of soluble, correctly folded and fluorescing trimers (Rutkowska 2012). However no such loosely reversible aggregated components were observed in the case of VP7-177-eGFP and VP7-200-eGFP (Rutkowska 2012). Thus, the insertion of eGFP into sites 144, 177 and 200 of the available VP7 vectors led to fusion proteins that could (at late stages) either be present in the cell as correctly folded, fluorescing protein or as so-called "cold", non-fluorescing versions that very may well be misfolded.

It was unknown whether the tendency of correctly folded, fluorescing VP7-144-eGFP trimers to aggregate is due to the site of the insertion and its effect on the protein structure, or whether it could be due to over-expression of the protein later in the infection cycle. To investigate, a comparison was made of the synthesis and aggregation of VP7-144-eGFP and VP7-200-eGFP from the early stages of the infection cycle to the later stages of the cycle when the proteins are over-expressed. These two constructs were selected for this study because VP7-144-eGFP is largely soluble and correctly folded, whereas only a small fraction of the total VP7-200-eGFP protein expressed is soluble (Rutkowska 2012). Thus, fluorescence in the case of VP7-144-eGFP may provide an indication of what happens to particle formation, whereas in the case of VP7-200-eGFP fluorescence data will indicate what happens to the small fraction of correctly folded protein and not the bulk of the protein. In contrast, immunoblots would detect the total relative protein in each fraction of a sucrose gradient, thereby indicating whether or not the protein is correctly folded or misfolded.

Sucrose gradient sedimentation analyses were performed on cells harvested at different time points throughout the course of an infection cycle (at 24, 30, 38 and 48 hpi) and the distribution of fluorescing VP7-eGFP fusions assessed both before and after treatment with L-arginine. Various

94

chemicals such as the anionic detergent Na⁺*N*-Lauroylsarcosine (Sarkosyl) and the amino acid L-arginine (Ishibashi *et al.* 2005) are able to increase protein solubility by reversing or preventing protein aggregation. L-arginine was used here as it does not act as a protein denaturant (Ishibashi *et al.* 2005; Tsumoto *et al.* 2005), even though it may cause the activation of cellular proteases. The total relative protein within each fraction was also calculated from immunoblots, and compared to the fluorescence readings. What is particularly noticeable from these results is that VP7-144-eGFP forms aggregates in the cell, the formation of which starts early in the infection cycle and not only as a result of the over-expression that inevitably occurs at the later stages of the infection cycle. These aggregates could be solubilised with L-arginine, suggesting that they were composed of loosely formed layers of VP7-144-eGFP trimers that spontaneously aggregated via trimer-trimer interactions mimicking those involved in the self-assembly of WT VP7. Some of the fluorescing VP7-144-eGFP protein that was present in the particulate fractions was irreversibly aggregated and is thought to represent soluble, fluorescing protein that was trapped within misfolded protein. Although over time there was an increase in the synthesis of misfolded protein, VP7-144-eGFP appears to be an inherently soluble and fluorescing protein.

In the case of VP7-200-eGFP the protein component that fluoresced was largely present in the soluble fraction, with little to no evidence of reversible protein aggregation. Of interest here was that VP7-200-eGFP was shown to have a significant non-fluorescing, presumably misfolded, component that increased with the progression of the infection cycle. This may be inherent to this particular construct. It is possible that the large eGFP inserts in the top domain 200 sites present a much larger folding challenge than in the less congested 144 site. When the protein is overexpressed very little of the expressed protein is correctly folded and it forms insoluble, nonfluorescing aggregates. The much reduced trimer stability of VP7-200-eGFP may also affect the trimer-trimer aggregation observed in the case of VP7-144-eGFP.

Some degradation was observed at the later time points, where most of the misfolded protein was observed. Furthermore, this problem was more apparent in the case of VP7-200-eGFP, the more misfolded of the two, and was similar to that described by Rutkowska (2012), and may thus be present as a result of site-specific nicks introduced by cellular proteases in the presence of L-arginine. Proteases are part of the ubiquitin-proteasome pathway and target misfolded proteins (Dobson 2003; Tyedmers *et al.* 2010). Rutkowska (2012) showed that nicked trimers retain their integrity during centrifugation but that denaturing conditions such as heating to 95˚C and exposure to SDS causes the cleaving of specific peptides.

Next, confocal and TEM were used to investigate the effect of the eGFP insertion on the self-assembly and particle formation of VP7. The results generated here show that the trimeric VP7-144-eGFP self-assembles in a manner similar to that of WT VP7, in that small protein aggregates

95

migrate through the cell and interact to form a large electron dense structure located mainly in the cytoplasm of Sf9 cells, confirming what was seen by Bekker *et al.* (2014). However, both the number and overall shape of these structures differ from that of WT VP7. In contrast to the multiple, flat hexagonal structures formed by WT VP7, VP7-144-eGFP formed a single large, irregular structure in the cell. These so-called foci of fluorescence fluoresced strongly under the confocal microscope, and were visualised as electron dense structures under the TEM. Z-stack analysis showed that the foci are large, elongated and somewhat spherical in nature. These structures also differed from the spindle-like particles formed by VP7-144, which loosely aggregated into multiple star-shaped spindle aggregates within the cell, as well as the rosette-like structures formed by VP7-177 and VP7-200. This is therefore strong evidence of the VP7-144-eGFP aggregation seen in the results obtained by sucrose gradient sedimentation analyses.

In contrast to VP7-144-eGFP, both VP7-177-eGFP and VP7-200-eGFP accumulated to multiple sites in the cell. No rosette-like structures were observed, nor were the hexagonal particles typical of WT VP7. Instead, small protein aggregates similar to those observed in the case of VP7-144-eGFP were observed in these Sf9 cells and appeared to migrate through the cytoplasm and eventually interacted to form multiple foci of strong fluorescence, but they never reached the stage of a single large focus per cell. Confocal microscopy and Z-stack analysis showed that the VP7-177-eGFP foci were spherical and considerably smaller than those formed by VP7-144-eGFP, whereas the largely monomeric VP7-200-eGFP formed small and flat disc-shaped foci that sometimes appeared rod-like at a 90° angle. TEM showed that the structures formed by both VP7-177-eGFP and VP7-200-eGFP were not as large, rigid or as electron dense as the structures formed by VP7-144-eGFP. Rod-like structures were occasionally observed in Bac-VP7-200-eGFP infected cells but were not observed in the case of cells infected with Bac-VP7-144-eGFP or Bac-VP7-177-eGFP. Also, in the case of all three VP7-eGFP fusion proteins, no typical stacking of layer-upon-layer of protein was observed.

Confocal microscopy of mammalian cells infected with BTV, as well as those transfected with a plasmid expressing BTV VP7, has shown that BTV VP7 is initially distributed homogenously throughout the cytoplasm and gradually forms small foci with the progression of the infection cycle (Kar *et al.* 2007; Drew *et al.* 2010a; Drew *et al.* 2010b). To an extent it appears that the foci formed by VP7-177-eGFP and VP7-200-eGFP resemble those formed by BTV VP7.

The non-fluorescing misfolded VP7-eGFP observed by means of sucrose sedimentation analysis, especially so in the case of VP7-200-eGFP, raised questions as to the localisation of such proteins in the cell and prompted an immunofluorescence-based investigation. Sf9 cells were infected with recombinant baculoviruses expressing VP7-144-eGFP, VP7-177-eGFP and VP7-200-eGFP. At 48 hpi, the cells were fixed and labelled with anti-VP7 or anti-GFP primary antibodies, in conjunction

96

with the appropriate red secondary antibodies. As green auto-fluorescence is indicative of correct protein folding (Waldo *et al.* 1999) it was postulated that correctly folded proteins would be detected by green auto-fluorescence, whereas a red signal from the immunolabelling would represent all versions of the proteins. Thus, we would be able to differentially detect misfolded proteins by a red signal in the absence of green auto-fluorescence. It is important to note that such a result would indicate the distribution patterns of the different forms of the protein but would not allow for a quantitative result as labelling may not occur in a manner directly proportional to the amount of protein present.

In all cases and for all proteins, the correctly folded fluorescing proteins were co-detected by the antibody labelling, the only differences being the intensity of the signal. The commercial antibody directed against GFP showed more specific labelling than the anti-VP7 antibodies used in this study. At times, "halos" similar to those seen in the labelling of the structures formed by the VP7 vector proteins were observed here, indicating that the antibodies only labelled the surface of each focus of fluorescence. The foci of fluorescence formed by VP7-177-eGFP and VP7-200-eGFP were labelled more readily than those formed by VP7-144-eGFP and may be due to epitope availability that is dependent on the size and shape of the aggregates, or on the nature of the packaging of the fusion proteins. Indeed it was shown by the dual microscopy analyses that the foci formed by VP7-177-eGFP are smaller than that of VP7-144-eGFP and those formed by VP7-200-eGFP are flat in nature. Thus, this may explain why the level of antibody labelling appeared strongest for VP7-200-eGFP.

High levels of co-localisation of red and green signals were observed throughout and no significant level of red signal in the absence of green auto-fluorescence was observed, indicating that no misfolded proteins were differentially detected. It has previously been suggested that misfolded proteins become compartmentalised into aggresomes or that they may be targeted for degradation by the cell's degradative pathways (Dobson 2003; Stefani 2004). A recent study has shown that AHSV VP7 trafficking is independent of other AHSV proteins as well as host transport and trafficking machinery (Bekker *et al.* 2014). Thus it is likely that the misfolded proteins detected via sucrose gradient sedimentation analysis may not be targeted to aggresomes or to the host cell's degradative machinery. Either the misfolded proteins localise to the same position in the cell as their correctly folded counterparts, or the method used here was unsuccessful at detecting such proteins.

The tendency of a protein to misfold and subsequently aggregate may be representative of intermolecular interactions taking preference over intramolecular interactions thereby leading to an alternative pathway to that of normal protein folding (Stefani 2004). It is possible that the insertion

97

of eGFP into site 200 affects normal VP7 trimer-trimer interactions thereby leading to increased protein misfolding.

Thus, it appears that VP7-144-eGFP behaves like VP7-144 in that it seems to form layers of trimer-trimer aggregates. The layering of these sheets is however, loosely structured and reversible by treatment with L-arginine and the normal VP7 particles are never formed. The bulk of the soluble versions of this protein are most likely found within the layers. Particle formation is observed in the case of VP7-177 and VP7-200, with the layering thereof hindered leading to the formation of rosette-like structures. The absence of a single large, or a number of large, structures in the cases of VP7-177-eGFP and VP7-200-eGFP may, in part, be due to a mass effect as less soluble fluorescing protein than VP7-144-eGFP is expressed in a cell thereby leading to fewer trimers being able to migrate to a single location in the cell. It is also possible that correctly folded protein gets trapped in the excess of misfolded protein, rendering it unable to move to one or a few sites in the cell. Also, the dense packing of VP7 as observed with the WT seems to be impossible, perhaps due to the proximity of the insertion sites and the size of eGFP.

This study suggests that AHSV VP7 self-assembly and particle formation are separate events and that the stable layering of VP7 into the characteristic flat hexagonal particles is strongly influenced by the top domain. In addition to this it appears that the overall morphology of these particles is dependent on a group of associated factors such as solubility, trimerisation and the site of the insertion and not solely on one inherent property of the protein.

This study, in combination with previous work on the AHSV VP7 mutant proteins used here, indicate that all of the mutant proteins differ with regard to solubility, trimerisation and the eventual morphology of the protein structures they form. It is unknown however, whether or not these top domain modifications affect the incorporation of VP7 into CLPs. By co-expressing each mutant with VP3 it would be possible to investigate the effect of these modifications on CLP formation and the overall ratio of CLPs to protein aggregates/structures. Along a similar line, expressing each mutant with the full complement of viral proteins one would be able to ascertain whether or not these modifications alter the ratio of VP7 trimers incorporated into virions versus those that associate to form particles. Another avenue of interest, and one that is currently being explored, is the role of trimer-trimer interactions on particle formation. By identifying putative residues that may be responsible for trimer-trimer interactions and then targeting them for mutation one may be able to assess their role in particle formation. Although this study provides insight into the self-assembly and particle formation of AHSV VP7 the role of these particles in the replication cycle and viral pathogenesis remains to be investigated. Thus, it may be of future interest to make use of a reverse genetics system in the hopes of elucidating the function of these particles.

98

References

Arnoldi, F, M Campagna, C Eichwald, U Desselberger, OR Burrone. 2007. Interaction of rotavirus polymerase VP1 with nonstructural protein NSP5 is stronger than that with NSP2. J Virol 81:2128-2137.

Babst, M. 2005. A protein's final ESCRT. Traffic 6:2-9.

Basak, AK, P Gouet, J Grimes, P Roy, D Stuart. 1996. Crystal structure of the top domain of African horse sickness virus VP7: comparisons with bluetongue virus VP7. J Virol 70:3797-3806.

Basak, AK, DI Stuart, P Roy. 1992. Preliminary crystallographic study of bluetongue virus capsid protein, VP7. J Mol Biol 228:687-689.

Beaton, AR, J Rodriguez, YK Reddy, P Roy. 2002. The membrane trafficking protein calpactin forms a complex with bluetongue virus protein NS3 and mediates virus release. Proc Natl Acad Sci U S A 99:13154-13159.

Beaudoin, S, K Goggin, C Bissonnette, C Grenier, X Roucou. 2008. Aggresomes do not represent a general cellular response to protein misfolding in mammalian cells. BMC Cell Biol 9:59.

Bekker, S, H Huismans, V van Staden. 2014. Factors that affect the intracellular localization and trafficking of African horse sickness virus core protein, VP7. Virology 456–457:279-291.

Belhouchet, M, F Mohd Jaafar, AE Firth, JM Grimes, PP Mertens, H Attoui. 2011. Detection of a fourth orbivirus non-structural protein. PLoS ONE 6:e25697.

Berkova, Z, SE Crawford, SE Blutt, AP Morris, MK Estes. 2007. Expression of rotavirus NSP4 alters the actin network organization through the actin remodeling protein cofilin. J Virol 81:3545-3553.

Berkova, Z, SE Crawford, G Trugnan, T Yoshimori, AP Morris, MK Estes. 2006. Rotavirus NSP4 induces a novel vesicular compartment regulated by calcium and associated with viroplasms. J Virol 80:6061-6071.

Berkova, Z, AP Morris, MK Estes. 2003. Cytoplasmic calcium measurement in rotavirus enterotoxin-enhanced green fluorescent protein (NSP4-EGFP) expressing cells loaded with Fura-2. Cell Calcium 34:55-68.

Bhattacharya, B, P Roy. 2008. Bluetongue virus outer capsid protein VP5 interacts with membrane lipid rafts via a SNARE domain. J Virol 82:10600-10612.

Bolte, S, FP Cordelieres. 2006. A guided tour into subcellular colocalisation analysis in light microscopy. Journal of Microscopy 224:213-232.

Boyce, M, CC Celma, P Roy. 2012. Bluetongue virus non-structural protein 1 is a positive regulator of viral protein synthesis. Virology Journal 9:178.

Boyce, M, J Wehrfritz, R Noad, P Roy. 2004. Purified recombinant bluetongue virus VP1 exhibits RNA replicase activity. J Virol 78:3994-4002.

Breese, SS, Jr., Y Ozawa. 1969. Intracellular inclusions resulting from infection with African horsesickness virus. J Virol 4:109-112.

Breese, SS, Jr., Y Ozawa, AH Dardiri. 1969. Electron microscopic characterization of African horse-sickness virus. J Am Vet Med Assoc 155:391-400.

Bremer, CW. 1976. A gel electrophoretic study of the protein and nucleic acid components of African horsesickness virus. Onderstepoort J Vet Res 43:193-199.

Bremer, CW, H Huismans, AA Van Dijk. 1990. Characterization and cloning of the African horsesickness virus genome. J Gen Virol 71 (Pt 4):793-799.

Brookes, SM, AD Hyatt, BT Eaton. 1993. Characterization of virus inclusion bodies in bluetongue virus-infected cells. J Gen Virol 74 (Pt 3):525-530.

Burroughs, JN, RS O'Hara, CJ Smale, C Hamblin, A Walton, R Armstrong, PP Mertens. 1994. Purification and properties of virus particles, infectious subviral particles, cores and VP7 crystals of African horsesickness virus serotype 9. J Gen Virol 75 (Pt 8):1849-1857.

Celma, CC, P Roy. 2011. Interaction of calpactin light chain (S100A10/p11) and a viral NS protein is essential for intracellular trafficking of nonenveloped bluetongue virus. J Virol 85:4783-4791.

Chuma, T, H Le Blois, JM Sanchez-Vizcaino, M Diaz-Laviada, P Roy. 1992. Expression of the major core antigen VP7 of African horsesickness virus by a recombinant baculovirus and its use as a group-specific diagnostic reagent. J Gen Virol 73 (Pt 4):925-931.

Cinelli, RA, A Ferrari, V Pellegrini, M Tyagi, M Giacca, F Beltram. 2000. The enhanced green fluorescent protein as a tool for the analysis of protein dynamics and localization: local fluorescence study at the single-molecule level. Photochem Photobiol 71:771-776.

Clift, SJ, ML Penrith. 2010. Tissue and cell tropism of African horse sickness virus demonstrated by immunoperoxidase labeling in natural and experimental infection in horses in South Africa. Vet Pathol 47:690-697.

Coetzer, JAW, AJ Guthrie. 2004. African horsesickness. In: Infectious Diseases Of Livestock With Special Reference To Southern Africa. J.A.W. Coetzer, G.R. Thomson, R.C. Tustin (Ed); N.P.J. Kriek (Ass Ed). Oxford University Press, Cape Town, pp 1231-1246.

Cooper, GM, RE Hausman. 2007. The Cell: A Molecular Approach. Washington, D.C.: ASM Press.

Cormack, B. 1998. Green fluorescent protein as a reporter of transcription and protein localization in fungi. Current Opinion in Microbiology 1:406-410.

Cormack, BP, RH Valdivia, S Falkow. 1996. FACS-optimized mutants of the green fluorescent protein (GFP). Gene 173:33-38.

Diaz, Y, ME Chemello, F Pena, et al. 2008. Expression of Nonstructural Rotavirus Protein NSP4 Mimics Ca^{2+} Homeostasis Changes Induced by Rotavirus Infection in Cultured Cells. J. Virol. 82:11331-11343.

Diprose, JM, JM Grimes, GC Sutton, JN Burroughs, A Meyer, S Maan, PP Mertens, DI Stuart. 2002. The core of bluetongue virus binds double-stranded RNA. J Virol 76:9533-9536.

Dobson, CM. 2003. Protein folding and misfolding. Nature 426:884-890.

Drew, CP, IA Gardner, CE Mayo, E Matsuo, P Roy, NJ MacLachlan. 2010a. Bluetongue virus infection alters the impedance of monolayers of bovine endothelial cells as a result of cell death. Veterinary Immunology and Immunopathology 136:108-115.

Drew, CP, MC Heller, C Mayo, JL Watson, NJ Maclachlan. 2010b. Bluetongue virus infection activates bovine monocyte-derived macrophages and pulmonary artery endothelial cells. Vet Immunol Immunopathol 136:292-296.

Eaton, BT, AD Hyatt, SM Brookes. 1990. The replication of bluetongue virus. Curr Top Microbiol Immunol 162:89-118.

Eaton, BT, AD Hyatt, JR White. 1987. Association of bluetongue virus with the cytoskeleton. Virology 157:107-116.

Els, HJ, DW Verwoerd. 1969. Morphology of bluetongue virus. Virology 38:213-219.

Firth, AE. 2008. Bioinformatic analysis suggests that the Orbivirus VP6 cistron encodes an overlapping gene. Virol J 5:48.

Forzan, M, M Marsh, P Roy. 2007. Bluetongue virus entry into cells. J Virol 81:4819-4827.

Forzan, M, C Wirblich, P Roy. 2004. A capsid protein of nonenveloped Bluetongue virus exhibits membrane fusion activity. Proc Natl Acad Sci U S A 101:2100-2105.

Gallagher, KL, PN Benfey. 2005. Not just another hole in the wall: understanding intercellular protein trafficking. Genes Dev 19:189-195.

Garcia-Mata, R, Z Bebok, EJ Sorscher, ES Sztul. 1999. Characterization and dynamics of aggresome formation by a cytosolic GFP-chimera. J Cell Biol 146:1239-1254.

Garcia-Mata, R, YS Gao, E Sztul. 2002. Hassles with taking out the garbage: aggravating aggresomes. Traffic 3:388-396.

Gibbs, EP, WJ Tabachnick, TJ Holt, DE Stallknecht. 2008. U.S. concerns over bluetongue. Science 320:872.

Giepmans, BG. 2008. Bridging fluorescence microscopy and electron microscopy. Histochemistry and Cell Biology 130:211-217.

Giepmans, BNG, SR Adams, MH Ellisman, RY Tsien. 2006. The Fluorescent Toolbox for Assessing Protein Location and Function. Science 312:217-224.

Goff, A, LS Ehrlich, SN Cohen, CA Carter. 2003. Tsg101 control of human immunodeficiency virus type 1 Gag trafficking and release. J Virol 77:9173-9182.

Gold, S, P Monaghan, P Mertens, T Jackson. 2010. A clathrin independent macropinocytosis-like entry mechanism used by bluetongue virus-1 during infection of BHK cells. PLoS ONE 5:e11360.

Golovanov, AP, GM Hautbergue, SA Wilson, LY Lian. 2004. A simple method for improving protein solubility and long-term stability. J Am Chem Soc 126:8933-8939.

Gould, EA, S Higgs. 2009. Impact of climate change and other factors on emerging arbovirus diseases. Trans R Soc Trop Med Hyg 103:109-121.

100

Grimes, J, AK Basak, P Roy, D Stuart. 1995. The crystal structure of bluetongue virus VP7. Nature 373:167-170.

Grimes, JM, JN Burroughs, P Gouet, JM Diprose, R Malby, S Zientara, PP Mertens, DI Stuart. 1998. The atomic structure of the bluetongue virus core. Nature 395:470-478.

Grimes, JM, J Jakana, M Ghosh, AK Basak, P Roy, W Chiu, DI Stuart, BV Prasad. 1997. An atomic model of the outer layer of the bluetongue virus core derived from X-ray crystallography and electron cryomicroscopy. Structure 5:885-893.

Hassan, SH, C Wirblich, M Forzan, P Roy. 2001. Expression and functional characterization of bluetongue virus VP5 protein: role in cellular permeabilization. J Virol 75:8356-8367.

Hassan, SS, P Roy. 1999. Expression and functional characterization of bluetongue virus VP2 protein: role in cell entry. J Virol 73:9832-9842.

Hewat, EA, TF Booth, P Roy. 1992. Structure of bluetongue virus particles by cryoelectron microscopy. J Struct Biol 109:61-69.

Hewat, EA, TF Booth, P Roy. 1994. Structure of correctly self-assembled bluetongue virus-like particles. J Struct Biol 112:183-191.

Howell, PG. 1962. The isolation and identification of further antigenic types of african horsesickness virus. Onderstepoort Journal of Veterinary Research 29:139-149.

Huismans, H, HJ Els. 1979. Characterization of the tubules associated with the replication of three different orbiviruses. Virology 92:397-406.

Huismans, H, BJ Erasmus. 1981. Identification of the serotype-specific and group-specific antigens of bluetongue virus. Onderstepoort J Vet Res 48:51-58.

Huismans, H, AA van Dijk, AR Bauskin. 1987a. In vitro phosphorylation and purification of a nonstructural protein of bluetongue virus with affinity for single-stranded RNA. J Virol 61:3589-3595.

Huismans, H, AA van Dijk, HJ Els. 1987b. Uncoating of parental bluetongue virus to core and subcore particles in infected L cells. Virology 157:180-188.

Huismans, H, NT Vanderwalt, M Cloete, BJ Erasmus. 1987c. Isolation of a Capsid Protein of Bluetongue Virus That Induces a Protective Immune-Response in Sheep. Virology 157:172-179.

Hurley, JH, SD Emr. 2006. The ESCRT complexes: structure and mechanism of a membrane-trafficking network. Annu Rev Biophys Biomol Struct 35:277-298.

Hyatt, AD, BT Eaton, SM Brookes. 1989. The release of bluetongue virus from infected cells and their superinfection by progeny virus. Virology 173:21-34.

Hyatt, AD, AR Gould, B Coupar, BT Eaton. 1991. Localization of the non-structural protein NS3 in bluetongue virus-infected cells. J Gen Virol 72 (Pt 9):2263-2267.

Hyatt, AD, Y Zhao, P Roy. 1993. Release of bluetongue virus-like particles from insect cells is mediated by BTV nonstructural protein NS3/NS3A. Virology 193:592-603.

Ishibashi, M, K Tsumoto, M Tokunaga, D Ejima, Y Kita, T Arakawa. 2005. Is arginine a protein-denaturant? Protein Expr Purif 42:1-6.

Johnston, JA, CL Ward, RR Kopito. 1998. Aggresomes: a cellular response to misfolded proteins. J Cell Biol 143:1883-1898.

Kamper, N, PM Day, T Nowak, HC Selinka, L Florin, J Bolscher, L Hilbig, JT Schiller, M Sapp. 2006. A membrane-destabilizing peptide in capsid protein L2 is required for egress of papillomavirus genomes from endosomes. J Virol 80:759-768.

Kar, AK, B Bhattacharya, P Roy. 2007. Bluetongue virus RNA binding protein NS2 is a modulator of viral replication and assembly. BMC Mol Biol 8:4.

Kretzmann, H. 2006. The characterization of African horsesickness virus VP7 particles with foreign peptides inserted into site 200 of the VP7 protein top domein. Genetics: University of Pretoria. p. 125.

Lee, SY, A Poloumienko, S Belfry, X Qu, W Chen, N MacAfee, B Morin, C Lucarotti, M Krause. 1996. A common pathway for p10 and calyx proteins in progressive stages of polyhedron envelope assembly in AcMNPV-infected Spodoptera frugiperda larvae. Arch Virol 141:1247-1258.

Lepault, J, I Petitpas, I Erk, J Navaza, D Bigot, M Dona, P Vachette, J Cohen, FA Rey. 2001. Structural polymorphism of the major capsid protein of rotavirus. Embo J 20:1498-1507.

Limn, CK, P Roy. 2003. Intermolecular interactions in a two-layered viral capsid that requires a complex symmetry mismatch. J Virol 77:11114-11124.

101

Lodish, HF. 2004. Molecular Cell Biology. New York: W.H. Freeman and Company.

Maclachlan, NJ. 2010. Global implications of the recent emergence of bluetongue virus in europe. Vet Clin North Am Food Anim Pract 26:163-171, table of contents.

Maclachlan, NJ, AJ Guthrie. 2010. Re-emergence of bluetongue, African horse sickness, and other orbivirus diseases. Vet Res 41:35.

Manole, V, P Laurinmaki, W Van Wyngaardt, CA Potgieter, IM Wright, GJ Venter, AA van Dijk, BT Sewell, SJ Butcher. 2012. Structural Insight into African Horsesickness Virus Infection. J. Virol. 86:7858-7866.

Maree, FF. 2000. Multimeric protein structures of African horsesickness virus and their use as antigen delivery systems. Genetics: University of Pretoria.

Maree, S, S Durbach, H Huismans. 1998. Intracellular production of African horsesickness virus core-like particles by expression of the two major core proteins, VP3 and VP7, in insect cells. J Gen Virol 79 (Pt 2):333-337.

Martin, LA, AJ Meyer, RS O'Hara, H Fu, PS Mellor, NJ Knowles, PP Mertens. 1998. Phylogenetic analysis of African horse sickness virus segment 10: sequence variation, virulence characteristics and cell exit. Arch Virol Suppl 14:281-293.

Meiring, TL, H Huismans, V van Staden. 2009. Genome segment reassortment identifies non-structural protein NS3 as a key protein in African horsesickness virus release and alteration of membrane permeability. Arch Virol 154:263-271.

Mellor, PS, C Hamblin. 2004. African horse sickness. Vet Res 35:445-466.

Mertens, PPC, JN Burroughs, A Walton, MP Wellby, H Fu, RS O'Hara, SM Brookes, PS Mellor. 1996. Enhanced Infectivity of Modified Bluetongue Virus Particles for Two Insect Cell Lines and for Two Culicoides Vector Species. Virology 217:582-593.

Mizrachi, E. 2008. The solubility, particle formation and immune display of trimers of major capsid protein 7 of African Horsesickness Virus fused with enhanced green fluorescent protein. Genetics: University of Pretoria.

Monastyrskaya, K, N Staeuber, G Sutton, P Roy. 1997. Effects of domain-switching and site-directed mutagenesis on the properties and functions of the VP7 proteins of two orbiviruses. Virology 237:217-227.

Nason, EL, R Rothagel, SK Mukherjee, AK Kar, M Forzan, BV Prasad, P Roy. 2004. Interactions between the inner and outer capsids of bluetongue virus. J Virol 78:8059-8067.

Nienhaus, GU, J Wiedenmann. 2009. Structure, Dynamics and Optical Properties of Fluorescent Proteins: Perspectives for Marker Development. ChemPhysChem 10:1369-1379.

Oellermann, RA. 1970. Plaque formation by African horsesickness virus and characterization of its RNA. Onderstepoort J Vet Res 37:137-143.

Oellermann, RA, HJ Els, BJ Erasmus. 1970. Characterization of African horsesickness virus. Arch Gesamte Virusforsch 29:163-174.

OIE. 2011. Terrestrial Animal Health Code. Paris, France: OIE.

Owens, RJ, C Limn, P Roy. 2004. Role of an arbovirus nonstructural protein in cellular pathogenesis and virus release. J Virol 78:6649-6656.

Patel, A, P Roy. 2014. The molecular biology of Bluetongue virus replication. Virus Research.

Prasad, BV, S Yamaguchi, P Roy. 1992. Three-dimensional structure of single-shelled bluetongue virus. J Virol 66:2135-2142.

Prasher, DC. 1995. Using GFP to see the light. Trends Genet 11:320-323.

Prasher, DC, VK Eckenrode, WW Ward, FG Prendergast, MJ Cormier. 1992. Primary structure of the Aequorea victoria green-fluorescent protein. Gene 111:229-233.

Ramadevi, N, NJ Burroughs, PP Mertens, IM Jones, P Roy. 1998. Capping and methylation of mRNA by purified recombinant VP4 protein of bluetongue virus. Proc Natl Acad Sci U S A 95:13537-13542.

Rapoport, TA. 2007. Protein translocation across the eukaryotic endoplasmic reticulum and bacterial plasma membranes. Nature 450:663-669.

Ratinier, M, M Caporale, M Golder, et al. 2011. Identification and Characterization of a Novel Non-Structural Protein of Bluetongue Virus. PLoS Pathog 7:e1002477.

Reynolds, ES. 1963. The use of lead citrate at high pH as an electron-opaque stain in electron microscopy. J Cell Biol:208-212.

Riley, JA. 2003. Construction of a new peptide insertion site in the top domain of major core protein VP7 of African horsesickness virus. Genetics: University of Pretoria.

Roy, P. 2001. Orbiviruses. In: DM Knipe, PM Howley, editors. Fields Virology: Lippincott Williams and Wilkins. p. 1835-1865.

Roy, P. 2005. Bluetongue virus proteins and particles and their role in virus entry, assembly, and release. Adv Virus Res 64:69-123.

Roy, P, T Hirasawa, M Fernandez, VM Blinov, JM Sanchez-Vixcain Rodrique. 1991. The complete sequence of the group-specific antigen, VP7, of African horsesickness disease virus serotype 4 reveals a close relationship to bluetongue virus. J Gen Virol 72 (Pt 6):1237-1241.

Royant, A, M Noirclerc-Savoye. 2011. Stabilizing role of glutamic acid 222 in the structure of Enhanced Green Fluorescent Protein. Journal of Structural Biology 174:385-390.

Rutkowska, DA. 2012. Characterization of Major Capsid Protein VP7 of African horsesickness virus as an Antigen Display System. Genetics: University of Pretoria.

Rutkowska, DA, QC Meyer, F Maree, W Vosloo, W Fick, H Huismans. 2011. The use of soluble African horse sickness viral protein 7 as an antigen delivery and presentation system. Virus Res 156:35-48.

Schnell, U, F Dijk, KA Sjollema, BNG Giepmans. 2012. Immunolabeling artifacts and the need for live-cell imaging. Nature Methods 9:152-158.

Shaw, AE, E Veronesi, G Maurin, et al. 2012. Drosophila melanogaster as a Model Organism for Bluetongue Virus Replication and Tropism. J. Virol. 86:9015-9024.

Smith, GA, LW Enquist. 2002. Break ins and break outs: viral interactions with the cytoskeleton of Mammalian cells. Annu Rev Cell Dev Biol 18:135-161.

Stauber, N, J Martinez-Costas, G Sutton, K Monastyrskaya, P Roy. 1997. Bluetongue virus VP6 protein binds ATP and exhibits an RNA-dependent ATPase function and a helicase activity that catalyze the unwinding of double-stranded RNA substrates. J Virol 71:7220-7226.

Stefani, M. 2004. Protein misfolding and aggregation: new examples in medicine and biology of the dark side of the protein world. Biochim Biophys Acta 1739:5-25.

Stoltz, MA, CF van der Merwe, J Coetzee, H Huismans. 1996. Subcellular localization of the nonstructural protein NS3 of African horsesickness virus. Onderstepoort J Vet Res 63:57-61.

Studer, D, W Graber, A Al-Amoudi, P Eggli. 2001. A new approach for cryofixation by high-pressure freezing. J Microsc 203:285-294.

Tan, BH, E Nason, N Staeuber, W Jiang, K Monastryrskaya, P Roy. 2001. RGD tripeptide of bluetongue virus VP7 protein is responsible for core attachment to Culicoides cells. J Virol 75:3937-3947.

Traub, LM, S Kornfeld. 1997. The trans-Golgi network: a late secretory sorting station. Curr Opin Cell Biol 9:527-533.

Tsumoto, K, D Ejima, Y Kita, T Arakawa. 2005. Review: Why is arginine effective in suppressing aggregation? Protein Pept Lett 12:613-619.

Tsumoto, K, M Umetsu, I Kumagai, D Ejima, JS Philo, T Arakawa. 2004. Role of arginine in protein refolding, solubilization, and purification. Biotechnol Prog 20:1301-1308.

Tyedmers, J, A Mogk, B Bukau. 2010. Cellular strategies for controlling protein aggregation. Nat Rev Mol Cell Biol 11:777-788.

Urakawa, T, DG Ritter, P Roy. 1989. Expression of largest RNA segment and synthesis of VP1 protein of bluetongue virus in insect cells by recombinant baculovirus: association of VP1 protein with RNA polymerase activity. Nucleic Acids Res 17:7395-7401.

van Staden, V, J Theron, BJ Greyling, H Huismans, LH Nel. 1991. A comparison of the nucleotide sequences of cognate NS2 genes of three different orbiviruses. Virology 185:500-504.

Venter, E, CF van der Merwe, AV Buys, H Huismans, V van Staden. 2014. Comparative ultrastructural characterisation of African horse sickness virus-infected mammalian and insect cells reveals novel potential virus release mechanism from insect cells. Journal of General Virology 95:642-651.

Venter, E, CF Van Der Merwe, V Van Staden. 2012. Utilization of cellulose microcapillary tubes as a model system for culturing and viral infection of mammalian cells. Microscopy Research and Technique 75:1452-1459.

Venter, GJ, JJ Koekemoer, JT Paweska. 2006. Investigations on outbreaks of African horse sickness in the surveillance zone in South Africa. Rev Sci Tech 25:1097-1109.

Verwoerd, DW. 1969. Purification and characterization of bluetongue virus. Virology 38:203-212.

Verwoerd, DW, HJ Els, EM De Villiers, H Huismans. 1972. Structure of the bluetongue virus capsid. J Virol 10:783-794.

Verwoerd, DW, H Louw, RA Oellermann. 1970. Characterization of bluetongue virus ribonucleic acid. J Virol 5:1-7.

Waldo, GS, BM Standish, J Berendzen, TC Terwilliger. 1999. Rapid protein-folding assay using green fluorescent protein. Nat Biotechnol 17:691-695.

Ward, BM. 2011. The taking of the cytoskeleton one two three: how viruses utilize the cytoskeleton during egress. Virology 411:244-250.

Wetzel, R. 1994. Mutations and off-pathway aggregation of proteins. Trends in Biotechnology 12:193-198.

Wirblich, C, B Bhattacharya, P Roy. 2006. Nonstructural protein 3 of bluetongue virus assists virus release by recruiting ESCRT-I protein Tsg101. J Virol 80:460-473.

Xu, G, W Wilson, J Mecham, K Murphy, EM Zhou, W Tabachnick. 1997. VP7: an attachment protein of bluetongue virus for cellular receptors in Culicoides variipennis. J Gen Virol 78 (Pt 7):1617-1623.

Yu, Y, A Fukusho, DG Ritter, P Roy. 1988. Complete nucleotide sequence of the group-reactive antigen VP7 gene of bluetongue virus. Nucleic Acids Res 16:1620.

Zhang, G, V Gurtu, SR Kain. 1996. An enhanced green fluorescent protein allows sensitive detection of gene transfer in mammalian cells. Biochem Biophys Res Commun 227:707-711.

Zhang, J, RE Campbell, AY Ting, RY Tsien. 2002. Creating new fluorescent probes for cell biology. Nat Rev Mol Cell Biol 3:906-918.

Zhang, X, M Boyce, B Bhattacharya, X Zhang, S Schein, P Roy, ZH Zhou. 2010. Bluetongue virus coat protein VP2 contains sialic acid-binding domains, and VP5 resembles enveloped virus fusion proteins. Proc Natl Acad Sci U S A 107:6292-6297.

Zimmer, M. 2002. Green fluorescent protein (GFP): applications, structure, and related photophysical behavior. Chem Rev 102:759-781.